NUMERICAL AND EXPERIMENTAL MODELLING OF MICROWAVE APPLICATORS

DISSERTATION SUBMITTED TO THE
UNIVERSITY OF CAMBRIDGE FOR THE
DEGREE OF DOCTOR OF PHILOSOPHY

David Christopher Dibben

Darwin College
June 1995

To Michiyo

Declaration

The work presented in this dissertation was carried out in the Department of Engineering, University of Cambridge, during the period October 1991 to June 1995 under the supervision of Dr. A.C. Metaxas.

The author wishes to declare that, except for commonly understood and accepted ideas or where specific reference is made to the work of others, the work in this dissertation is his own and includes nothing which is the outcome of work done in collaboration. It has not been submitted in part, or in whole, to any other university for a degree, diploma or other qualification.

David Dibben
Darwin College
June 1995

Acknowledgements

I would like to express my appreciation to my supervisor, Dr. A.C. Metaxas for his support, encouragement and patience throughout the project. I would also like to thank the technicians in the electrical laboratory for their help, in particular Mr. Bob Gale for his assistance in the assembly of the experimental apparatus and to Dr. Stan Evans for his help designing the waveguide coupler. Thanks are also due to Unilever plc. for the loan of their spectrum analyser and to the EPSRC for providing financial support for this project.

Summary

This thesis presents a time domain finite element method for the solution of microwave heating problems. This is the first time that this particular technique has been applied to microwave heating. It is found that the standard frequency domain finite element method is unsuitable for analysing multimode applicators containing food-like materials due to a severe ill-conditioning of the matrix equations. The field distribution in multimode applicators loaded with low loss materials is found to be very sensitive to small frequency changes. Several solutions at different frequencies are therefore required to characterise the behaviour of the loaded applicator. The time domain finite element method is capable of producing multiple solutions at different frequencies when used with Gaussian pulse excitation; it is therefore ideally suited to the analysis of multimode applicators. A brief survey of the methods available for the solution of the linear equations is provided. The performance of these techniques with both the frequency domain and time domain finite element methods is then studied.

Single mode applicators are also analysed and it is found that the frequency domain method is superior in these cases. Comparisons are given between the calculated results and experimental data for both single mode and multimode systems. The importance of experimental verification being stressed.

The choice of element type is an important consideration for the finite element method. Three basic types of element are considered; nodal, Whitney edge elements and linear edge elements. Comparisons of the errors with these elements show that Whitney elements produce a consistently lower error when post-processing is used to smooth the solution.

The coupled thermal-electromagnetic problem is investigated with many difficulties being identified for the application to multimode cavity problems.

Indexing Terms

Microwave Heating

Multimode Cavities

Finite Element Analysis

Time Domain Analysis

Edge Elements

Contents

Summary i

Indexing Terms iii

List of Principle Symbols xi

1 Introduction 1

1.1 Microwave Energy: Volumetric and Selective Heating 1
1.2 Microwave Applicators 3
1.2.1 Single Mode Resonant Cavities 4
1.2.2 Multimode Cavities 5
1.3 Applicator Design 10
1.4 Computational tools 13
1.4.1 Analytical Methods 16
1.4.2 Numerical Methods 16
1.5 Experimentation and Verification 21
1.6 Computer Implementation 22

2 Finite Element Method: Electromagnetic Field Calculation 23

2.1 Introduction 23

2.1.1 Governing Equations 25
2.1.2 Spurious modes 26
2.2 Finite Element Discretisation 27
2.2.1 Traditional Nodal Elements 27
2.2.2 Edge Elements 29
2.3 Frequency Domain Finite Element Method 33
2.4 Time Domain Finite Element Method 34
2.4.1 Introduction 34
2.4.2 Formulation 35
2.4.3 Stability 38
2.4.4 Lumping 40
2.5 Boundary Conditions 41
2.5.1 Absorbing boundary conditions (ABCs) 42
2.6 Post-Processing of Edge Element Results 45
2.6.1 Error calculation 47
2.6.2 Comparison of Techniques 48
2.7 Comparison of Element Types 49
2.7.1 Comparison of Whitney Elements and Linear Edge Elements . . . 49
2.7.2 Comparison of Whitney Elements and Nodal Elements 52
2.7.3 Comparison of Edge Element Shapes 56
2.8 Conclusions 57

3 Solution of Linear Equations 59
3.1 Introduction 59
3.2 Direct Methods 60
3.3 Iterative Techniques 63
3.3.1 Introduction 63
3.3.2 Complex Systems 65
3.3.3 Preconditioning 66
3.3.4 Terminating Criteria 70
3.4 Ill-Conditioning 71
3.4.1 Estimation of the Condition Number 72

3.5 Application to the Frequency Domain Method 73
  3.5.1 Single Mode and Waveguide Problems 74
  3.5.2 Multimode Cavity Problems 75
3.6 Application to the Time Domain Method 79
  3.6.1 Diagonal Scaling 80
  3.6.2 Direct Methods 81
  3.6.3 SOR Iteration 81
  3.6.4 Preconditioned Conjugate Gradients 82
3.7 Conclusions 83

4 Calculation of the Reflection Coefficient and Absorbed Power 85

4.1 Introduction 85
4.2 Calculation of Reflection Coefficient 85
4.3 Power Calculation 88
  4.3.1 Power Calculation by E-Field Scaling 89
  4.3.2 Power Calculation by Scaling Total Power 90
4.4 Gaussian Pulse Excitation 91
4.5 Signal Processing Techniques 95

5 Results: Single Mode Cavities 97

5.1 Introduction 97
5.2 Rectangular Cavities 98
  5.2.1 Waveguide Loaded Cavity: TEAM Problem 18 98
  5.2.2 Experimental TE_{101} Applicator 104
5.3 Cylindrical TM_{010} Cavity 107
  5.3.1 TM_{010} Cavity: TEAM Problem 19 108
  5.3.2 Experimental TM_{010} Cavity 112
5.4 Conclusions 115

6 Results: Multimode Cavities 117

6.1 Introduction 117
6.2 Mesh Generation 118

6.2.1 Adaptive meshing 120
6.3 Experimental Setup 121
6.3.1 Thermal Imaging Technique 122
6.4 Mashed Potato Loaded Cavity 122
6.5 Pastry Block 129
6.6 Plastic Block 131
6.6.1 Introduction 131
6.6.2 Experimental Results 131
6.6.3 Solution at a Single Frequency 133
6.6.4 Multiple Frequency Solution 136
6.6.5 Effect of Lumping 139
6.6.6 Solution with a Fine Mesh 139
6.6.7 Effect of Variation in Dielectric Properties 141
6.6.8 Discussion of Results 144
6.7 Conclusions 144

7 Solution for Temperature 147
7.1 Introduction 147
7.2 Solution of the Heat Flow Equation 148
7.3 Temperature Distribution in Mashed Potato Load 150
7.4 Coupled Electromagnetic and Thermal Models 152
7.4.1 Introduction 152
7.4.2 Temperature Feedback 153
7.4.3 Ceramic Block Example 155
7.5 Conclusions 157

8 Conclusions and Recommendations for Further Work 159
8.1 Recommendations for Further Work 160

Bibliography 163

Appendices

A Element Types **175**

A.1 Hexahedral Edge Elements 175

A.2 Prismatic Elements 179

B Waveguide Coupler **183**

List of Principle Symbols

a	Width of waveguide or cavity
C_p	Specific heat capacity $W\,\mathrm{kg}^{-1}K^{-1}$
$\mathbf{D}$	Electric flux desnity
$\mathbf{E}$	Electric field strength
$\vec{e}$	Eigenvector of TE_{10} mode
e_i	Circulation of electric field along edge i of the mesh
$\mathbf{e}$	Vector of edge values
$\mathbf{H}$	Magnetic field strength
$\mathcal{H_0}(\mathrm{curl}) =$	$\{\mathbf{u} \in (L^2(\Omega))^3 \mid \nabla \times \mathbf{u} \in (L^2(\Omega))^3\ ,\ \mathbf{n} \times \mathbf{u} = 0\ \mathit{on}\ \Gamma\}.$
h_e	Convective heat transfer coefficient $\mathrm{W\,m^{-2}K^{-1}}$
$\hat{\mathbf{i}}, \hat{\mathbf{j}}, \hat{\mathbf{k}}$	Cartesian unit vectors
$\jmath$	$\sqrt{-1}$
$\mathbf{J}_s$	Source current density
k	Wave number, $\omega\sqrt{\mu_0\epsilon_0}$
$\mathbf{n}$	Normal vector to a surface

p_v	Power density $\mathrm{W\,m^{-3}}$
t	Time
Δt	Time step size
T	Temperature K
$\mathbf{w}_i$	Edge shape function assocuiated with edge i
Z_0	Impedance of free space 376.7 Ω
Z_w	Waveguide impedance

Greek Symbols

β	Phase constant
Γ	Surface
ϵ	Permitivity, $\epsilon_0\epsilon'$
ϵ'	Relative dielectric constant
ϵ''	Relative dipolar loss factor
ϵ^*	Absolute permitivity $\epsilon_0(\epsilon' - \jmath\sigma_e/\omega\epsilon_0)$
ϵ_0	Permittivity of free space, 8.854×10^{-12} F/m
ϵ_r	Relative Permittivity $\epsilon_r = \epsilon' - \jmath\sigma_e/\omega\epsilon_0$
κ	Thermal conductivity $\mathrm{W\,m^{-1}K^{-1}}$
$\kappa(\mathbf{A})$	Condition number of matrix $\mathbf{A}$
κ_2	Condition number of a matrix measured using 2-norms
λ_i	Barycentric coordinate of node i
λ_0	Free space wavelength
λ_g	Waveguide wavelength
μ	Permeability
μ_0	Permeability of free space , $4\pi \times 10^{-7}$ H/m

ρ	Material density $\mathrm{kg\,m^{-3}}$
ρ	Reflection coefficient
ρ_c	Charge density
σ_c	Electrical conductivity
σ_e	Effective conductivity, $\sigma_e = \sigma_c + \epsilon''\epsilon_0\omega$
σ_s	Stefan-Boltzmann constant $\mathrm{W\,m^{-2}K^{-4}}$
τ_c	Number of non-zeros in coefficient matrix
τ_f	Number of non-zeros in factored matrix
ψ	Weighting function
ω	Angular frequency, rad/sec.
Ω	Integration domain
Ω_e	Volume of element

Chapter 1 Introduction

1.1 Microwave Energy: Volumetric and Selective Heating

The last twenty years has seen a consolidation of the use of microwave energy as an effective source for the volumetric and selective heating of dielectric materials. It has found successful application in many areas; industrial, commercial, domestic and medical. The largest area of use is for the processing of food, the tempering of fruit, meat, fish and dairy produce, for the heating and cooking of meals and for sterilisation and pasteurisation. The domestic microwave oven is now a common household appliance throughout the world and many food producers are turning to microwave heating as a means of achieving the high quality products demanded by todays consumers. The sizes of these systems can range from a few hundred watts for a domestic oven to over 250 kilowatts for a recent industrial oven designed for the dry frying of snack foods. As well as food applications microwave heating has also seen use for the processing of textiles and ceramics. It has also been used extensively for the hyperthermia treatment of tumours and for the warming of blood prior to transfusion into humans. It can be seen from the range of applications that microwave heating is a very versatile and powerful method for the heating of dielectric materials.

All of these uses have one thing in common: they all require some form of applicator to transfer the microwave energy from the source into the material being treated.

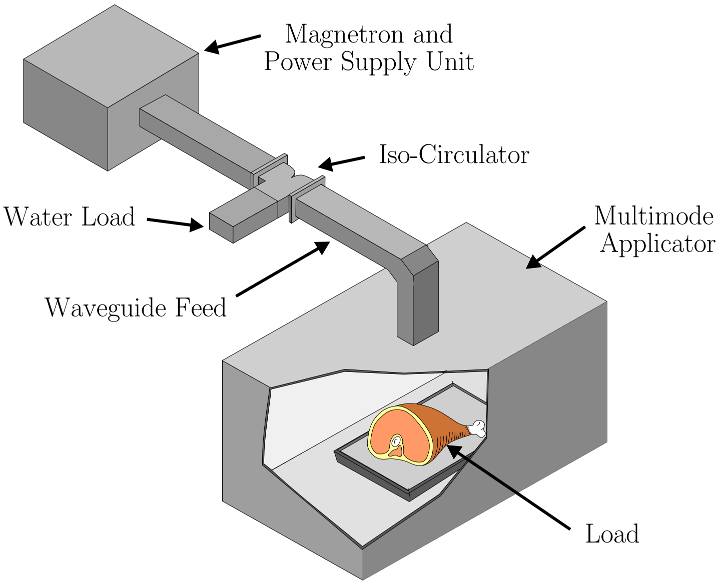

Figure 1.1: A typical microwave system.

Figure 1.1 shows a typical set up for a industrial system, where a magnetron supplies energy to a cavity applicator via a waveguide feed. An iso-circulator [Metaxas & Meredith, 1983] is used in the feed to absorb any reflections from the cavity. This prevents damage to the magnetron from occurring. Domestic ovens follow exactly the same design except that the expensive iso-circulator is not used since only low power levels are present. The feed waveguide is also much shorter in domestic ovens. For large ovens, the cavity may be several meters long with several magnetrons feeding it at different points. Often a conveyor belt is employed to carry the product through the oven. The design of these applicators governs both the efficiency with which the material can be heated and the degree of heating uniformity that is produced. Simulation can aid in the design of these applicators by allowing the heating pattern to be determined in advance. There are several different techniques that may be used to analyse the applicator structures. These are described later in this chapter, however, this thesis will concentrate on the application of the finite element method. The simulation methods described provide an extra weapon in the armoury of designers of microwave systems. As well as allowing designs to be tested without the need for the construction of expensive prototypes they can give further insights into the nature of the heating process.

Two basic types of applicator are considered in this thesis; the single mode resonant cavity and the multimode cavity. The former type is ideal for special purpose applications, such as the heating of textile fibres, liquids [Metaxas, 1974] or webs [Metaxas & Meredith, 1978] where the size and shape of the product allows the use of special applicator designs. The multimode type, by way of contrast lends itself to general purpose applications since it is capable of heating a wide range of loads of differing geometries and material properties in either batch and continuous operation [Metaxas & Meredith, 1983]. The wide application of the multimode cavity has lead to its dominance, with single mode applicators comprising only few percent of the systems in use in industry. The multimode applicator is, however, considerably more complex to model than the single mode type and as a consequence their design has relied almost entirely upon the experience of the designer and on trial and error. These two classes of applicator are described in the next section. Other applicator types do exist, such as the meander applicator, but their usage is extremely limited and is therefore not considered here.

This chapter outlines the basic principles of these applicators and the current methods of design. By considering them from a qualitative standpoint initially an insight into potential problems that may be encountered during a numerical analysis is gained. This influences the choice of method that will be used for the analysis.

1.2 Microwave Applicators

The applicator forms the focus for the modelling effort since its design will ultimately determine both the heating pattern and the efficiency of the system. If heating is concentrated in a small area of the load then considerably more energy will be required to heat the whole product to the desired temperature than if the heating was uniform. Two types of applicator design are considered, the single mode type being described first followed by the multimode applicator.

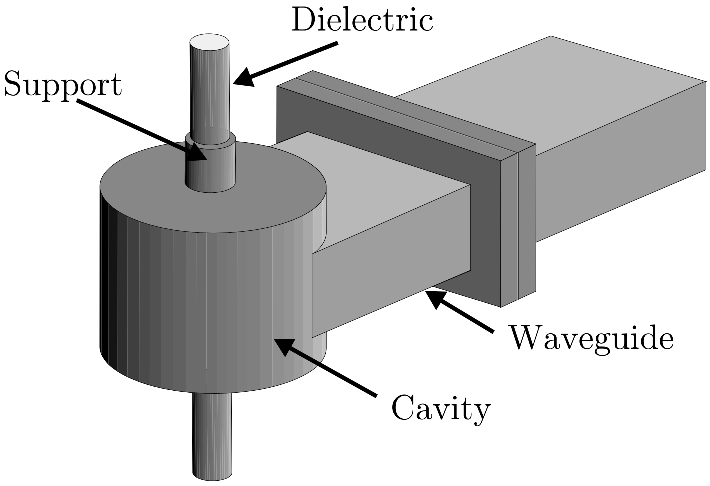

Figure 1.2: TM_{010} single mode resonant cavity

1.2.1 Single Mode Resonant Cavities

The single mode cavity, as its name suggests, is an applicator designed to operate in a single resonant mode. The dimensions of the cavity are chosen such that the resonant frequency of this mode coincides with the frequency of the source when the applicator is loaded. The field distribution within the cavity can often be determined analytically, so the cavity can easily be designed to provide the desired heating characteristics. Two typical cavities are shown in Figures 1.2 and 1.3. These types of cavities are limited to filament type loads, such as textile fibres, cylindrical ceramic samples, or liquids flowing in small bore tubes. For these types of application single mode cavity designs are ideal.

While the field distributions can be calculated analytically, there are still certain parameters that are difficult to determine in this way. It is possible that the loading will cause some higher order modes to be excited in which case the field pattern will deviate from that of the dominant mode. In most cases this will be undesirable and steps can be taken to suppress these extra modes. The cavities are generally connected to the waveguide system via an aperture, as shown in Figure 1.3, the size of which determines the impedance matching between the source and the cavity, and therefore the amount of power that can be transferred. A numerical technique can be used to analyse the effect of different aperture dimensions and so aid the design of the system. Also, in cases of

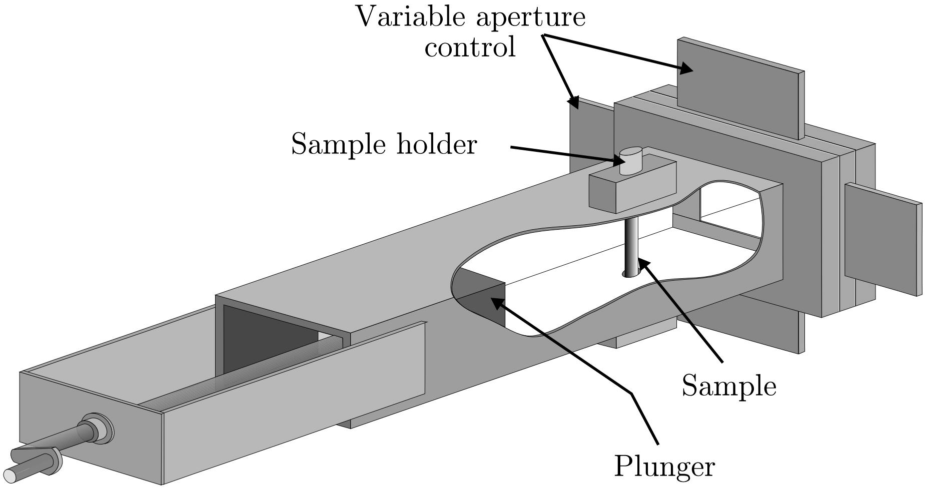

Figure 1.3: TE_{103} single mode resonant cavity

inhomogeneous loading, the field pattern may not be obtainable analytically, in which case a numerical method will provide useful information.

The design of the cavities is such that higher order modes, for example the TM_{020} mode in a cavity designed for TM_{010} operation occur at frequencies considerably greater than that of the operating frequency. This means that the resonant modes are well separated unless the cavity is very heavily loaded. The pattern will not, therefore, vary greatly as the frequency is changed. However, the magnitude of the field inside the cavity is likely to vary significantly with frequency, especially when the Q-factor of the cavity is high. This means that it is necessary to calculate the response of the system at a range of different frequencies. A time domain solution with Gaussian pulse excitation (described in §4.4) allows this to be done using a single calculation whereas solution in the frequency domain will require multiple calculations, one at each frequency of interest. Chapter 5 presents results for single mode cavities and compares the time domain and frequency domain approaches.

1.2.2 Multimode Cavities

A multimode cavity, depicted in Figure 1.4, is simply a metal enclosure, generally rectangular in shape, which is capable of supporting a large number of resonant modes.

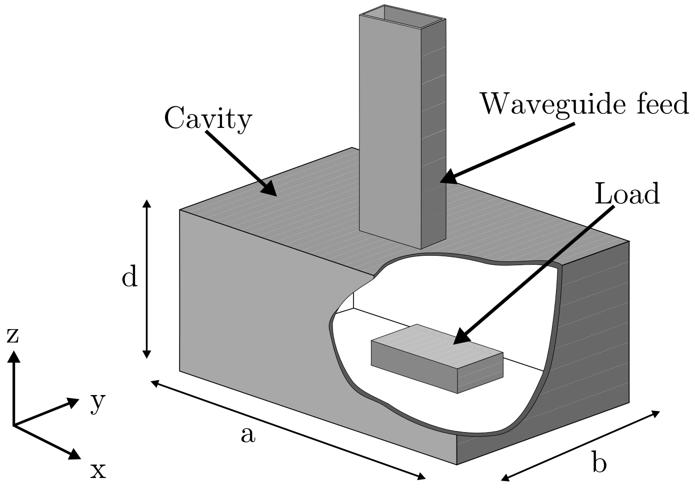

Figure 1.4: Multimode cavity, showing a rectangular load placed inside the cavity.

A feed system is incorporated to couple the cavity to the source of microwave energy. Multimode cavities are capable of accepting a wide range of loads with different geometries and material properties. This flexibility has made them the most widely used type of applicator, with the standard domestic oven being of this type. The applicator derives its name from its ability to support a large number of resonant modes near to the operating frequency, these combine to give some degree of uniformity of heating within the applicator. However, the large number of possible modes makes this type of applicator particularly difficult to analyse. The analysis of the heating of dielectrics inside a multimode system is far from simple, however, many ideas have been put forward to qualitatively account for the behaviour. These generally rely the concept of resonant cavity modes to account for the field distribution inside the cavity, however, many other effects are present which can significantly alter the power distribution that is produced in the load [Risman, 1993; Meredith, 1994].

Resonant Cavity Modes

Attempts are often made to describe the heating effects in terms of various resonant modes. For an empty cavity the modes are clearly defined and if the cavity geometry is rectangular or cylindrical their computation becomes trivial. For an empty rectangular

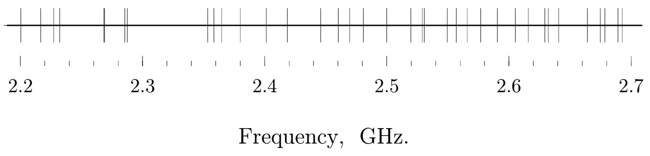

(a) Position of the modes near to 2.45 GHz

Frequency, GHz	l	n	m
2.4012	3	0	3
2.4186	4	1	2
2.4459	2	4	1
2.4602	3	1	3
2.4695	0	3	3
2.4808	0	4	2

(b) Mode indices for 6 modes

Figure 1.5: Position of the resonant modes of a multimode cavity with dimensions 300 x 280 x 240 mm.

cavity the modes obey the relationship [Metaxas & Meredith, 1983],

$$\left(\frac{l\pi}{a}\right)^2 + \left(\frac{m\pi}{b}\right)^2 + \left(\frac{n\pi}{d}\right)^2 = \left(\frac{\omega_{lmn}}{c}\right)^2, \tag{1.1}$$

where l, m and n are integers corresponding to the number of half-wavelengths of quasi-sinusoidal variation of the field along the x, y and z axes respectively, while ω_{lmn} is the resonant frequency of the mode and c is the speed of light.

For example, consider a small cavity typical of many multimode applicators, with dimensions 300 × 280 × 240 mm, which supports several modes near to the operating frequency of 2.45 GHz. These are shown in Figure 1.5. Since most computational methods generally assume that the walls of the cavity are perfect conductors the Q-factor of the modelled cavity will be very high. The only load on the empty cavity being due to the feed system. This means that in order to excite a resonance the source frequency must coincide with the resonant frequency. At source frequency of 2.45 GHz, we would expect the only field in the cavity to be that emanating from the waveguide aperture. As the frequency is increased we would expect a resonance to be observed at 2.4602 GHz and again at 2.4695 GHz. The shapes of three of these modes are given in Figure 1.6. It is worth noting that the percentage change in frequency between the 3,1,3

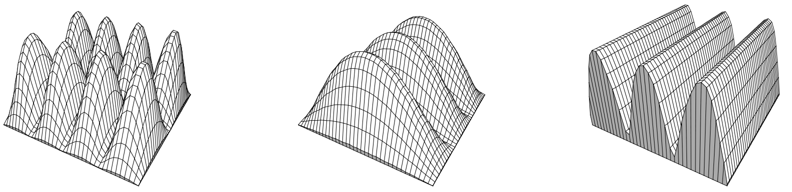

(a) 42x mode (b) 13x mode (c) 30x mode

Figure 1.6: Field patterns of three different resonant modes

mode and the 0,3,3 mode is only 0.37 %, however, the field patterns at these frequencies are very clearly different. This would suggest that the field distribution in an empty or lightly loaded multimode cavity will be extremely sensitive to small changes in frequency. Also, since the resonant frequencies are dependent on the dimensions, a small change in the size of the cavity will shift the position of the modes and consequently lead to a large change in the field pattern. This sensitivity of the system to small perturbations has important implications for the modelling of multimode cavities. Results presented in Chapter 6 show how this sensitivity can manifest itself in real situations during the heating of low loss materials.

Loaded Cavities

The discussion above assumed that the cavity was not loaded in any way, giving rise to very high Q-factors. In practice, since we are investigating microwave heating phenomena, the cavities will be loaded with lossy dielectrics. When ceramics are being heated this loading may be very slight, whereas food-like materials which have a much higher loss factor will produce much lower Q-values. In a loaded cavity many more modes are present and they are no longer sharp resonances but have a broad frequency response, shown qualitatively in Figure 1.7. Furthermore, the modes cannot be easily calculated using an expression such as equation (1.1). If the cavity is loaded with an arbitrarily shaped dielectric then a numerical technique is required to calculate the resonant

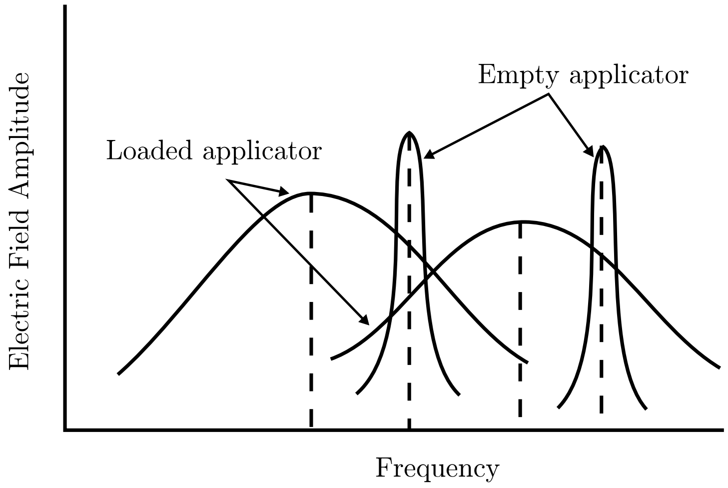

Figure 1.7: Resonant modes in an unloaded and loaded cavity, after Metaxas & Meredith [1983]

frequencies and field patterns of the modes [Collin, 1991].

A common practice for designing multimode applicators is to simply produce a cavity which has the largest number of modes when empty. Since more modes will be present when loaded it is argued that the large number of modes will overlap to produce uniformity. This approach, however, is is far too simplistic. Edge overheating for example is often caused by modes whose electric field is parallel to the edges of the load which gives highly efficient transfer of energy into the load [Risman, 1993]. Consequently one or two modes can dominate the transfer of energy into the load. Also, the above argument does not take into account the method of excitation. While the cavity may be capable of supporting a large number of modes it is by no means certain that they will all be excited. Here the nature of the feed system plays a vital role. This qualitative approach, while allowing a certain insight into the possible causes of problems, such as edge over-heating, cannot fully describe the field distribution in a given applicator unless all the modes are accurately calculated. The use of a numerical technique is therefore required.

The large number of modes present in a loaded multimode applicator allows it to couple power into a very wide range of loads. The loads vary greatly in shape, size and dielectric properties. It is this flexibility which makes multimode applicators so popular. The price for this versatility is, however, a degree of non-uniformity of heating. One way in which this non-uniformity manifests itself is in localised overheating.

The phenomena of localised heating, or hot spots, in multimode applicators is familiar to anyone who has used a domestic microwave oven. In food applications the lack of uniformity of heating can cause burns when food is too hot or allow bacteria to remain if areas have not reached a sufficient temperature to destroy them. In non-food application the results of non-uniform heating can be extremely detrimental. Materials such as ceramics often have a loss factor that increases exponentially with temperature. Uneven heating can, therefore, produce a thermal runaway leading to the destruction of the sample being heated [Metaxas & Meredith, 1983]. Uniform heating is therefore the goal of many applicator designers, whereas in certain situations non-uniform or selective heating is highly desirable, an example being the drying of web-like materials were the energy is targeted in areas of high moisture.

Risman [1993] proposes several different causes for the non-uniformity of heating. These provide an explanation for the effects when they occur but do not provide the applicator designer with firm information as to the possible performance of a particular design. Furthermore, for a load which has a complex geometry or regions with different material properties, they can do no more than provide the most general guide to the effects that may be observed.

1.3 Applicator Design

The careful design of applicators is essential if one is to avoid the type of localised overheating described previously for multimode applicators or to achieve a good impedance match in single mode systems. However, the current design process for many systems is very empirical, often relying entirely on the designers experience, trial and error and the construction of expensive prototypes. The reason for this approach lies in the fact that multimode applicators are notoriously difficult to analyse. Single mode resonant cavity applicators on the other hand, where there is only one dominant field pattern can be described in relatively simple terms by analytical expressions. Even so, when they are coupled to a waveguide feed via an aperture, or are heavily loaded so that higher order modes start to become significant, the use of analytical expressions becomes increasingly difficult. The purpose of this thesis is to present a numerical method for analysing different applicator structures rather than to present novel designs for microwave systems. These techniques will hopefully allow the designers of microwave applicators to remove some of the trial and error in the design process.

The field pattern in a multimode applicator is determined by both the nature of the load and the size of the cavity. It is therefore impossible to predict the exact field pattern for an arbitrary load without carrying out a full solution of Maxwell's equations for the loaded cavity. Since it is often the case that no two loads are identical, especially when dealing with food products, this solution will apply only to the load that has been modelled. The position of the load in the cavity will also effect the field pattern, a change of only a few millimeters being sufficient to alter the distribution. Given these difficulties it is still possible to gain useful insights from simulations of loaded multimode cavities. One can, for example, determine the degree of sensitivity of the system to various parameters, such as the source frequency, feed position, load position or dielectric properties. It is also possible to test different applicator designs against a set of loads, varying the dimensions and observing the effects. The feed system is another area that can be addressed since small changes in the feed can produce large changes in the way the cavity modes are excited. Simulation can then allow the designer to experiment with various changes to a feed design, while keeping all other factors constant. This would be difficult to do in an experimental situation. The behaviour is also dependent on the source of the microwaves. It will be seen from results presented in Chapter 6 that a small change in frequency can lead to large changes in the field distribution inside the applicator, especially when loaded with a low loss dielectric. A further complication arises because the behaviour of the source is generally dependent upon the load to which it is connected. Fortunately, many industrial systems employ an iso-circulator, as shown in Figure 1.1 that isolates the source from the applicator allowing for this effect to be discounted in many applications.

Microwave heating attempts to efficiently couple power from the source of microwaves into the load being heated. It is therefore of obvious interest to determine the amount of power dissipated inside the load. When the system is fed via an iso-circulator the load impedance will determine the fraction of the supplied power, P_0, absorbed by the cavity, P and the amount reflected back into the water load of the iso-circulator, since

$$P = P_0(1 - |\rho|^2), \tag{1.2}$$

where the reflection coefficient, ρ, is a function of the impedance. Determination of the impedance of the loaded applicator as seen from the waveguide feed is an extremely important aspect of the calculation which is often neglected in numerical simulations. If the magnetron is coupled directly to the cavity then this impedance will be seen by the magnetron and will therefore determine its output power and the efficiency with which it will operate. A knowledge of the absolute value of the power absorbed is necessary to correctly determine the temperature rise. The calculation of the impedance and the reflection coefficient are discussed in Chapter 4. Comparisons of the calculated values and experimentally determined ones for single mode cavities are then given in Chapter 5.

Frequency of Operation

The microwave frequencies allocated for industrial use are 896 MHz (915 MHz in the USA) and 2.45 GHz. The sources that produce the microwave energy, invariably a magnetron for heating applications, will not operate exactly at these frequencies. The regulations allow a tolerance of ±10 MHz at 896 MHz and ±50 MHz at 2.45 GHz [Metaxas & Meredith, 1983]. Variations in construction and in the power supply to the magnetron mean that every magnetron will operate at a slightly different frequency. The frequency of operation is also dependent on the impedance of the load to which it is supplying power. This thesis will give results that show how very small changes in frequency (< 0.5 %) can significantly alter the field distributions with some load configurations. This variation in frequency is therefore an important consideration when modelling microwave applicators, a fact which is appreciated by very few workers [Ma *et al.*, 1994]. One of the advantages of the scheme that will be presented in this thesis is its ability to provide information over a range of different frequencies. This immediately provides an indication to the systems sensitivity to frequency and to the nature of the changes that are likely to occur.

1.4 Computational tools

The advent of powerful computational tools has led to the rapid development of numerical techniques for solving complex problems. As the availability of high speed computers has become more widespread so has the range of applications to which these techniques have been applied. Microwave heating systems have only recently started to receive attention in terms of numerical analysis [Lorenson & Gallerneault, 1991]. One of the major causes of this slow start has been that very few assumptions can be made that will reduce the size of the problem to a manageable level. Whereas waveguide problems can be solved in two dimensions and produce useful results, multimode applicators require a full three dimensional vector field solution. Some two dimensional models have been proposed, [Desai *et al.*, 1992; Audhuy-peaudecerf *et al.*, 1993], however, unless some special symmetry can be exploited these cannot yield meaningful results. Consider, for example, the case of a rectangular block heated in a multimode cavity. It is often the case that the power density is concentrated in the corners of the block, a two dimensional model consisting of a vertical slice through the centre of the block would fail to indicate this, demonstrating the necessity of three dimensional models.

Many recent papers that allude to microwave heating in their introduction turn out to be disappointing in their application often referring only to relatively simple waveguide problems and then concluding with a statement along the lines of "this is easily extended to cavity problems and three dimensions". As examples in this thesis will demonstrate the transition from waveguide problems and small cavities with one or two dominant modes to large multimode resonant cavities is far from straight forward. It is not simply a case of discretising the larger problem using more elements and solving as before. Other difficulties have to be overcome and it is these that are addressed here.

Full three dimensional models are extremely expensive computationally, particularly when most applicators are at least two to three free space wavelengths in each dimension. Assuming a working value of, say, 10 grid points per wavelength, this produces $30^3 = 27,000$ grid points and given that there are three components of the field at each grid point we have $81,000$ unknown quantities[1] when using a numerical method based on

---

[1] Boundary conditions will reduce this number slightly.

a regular lattice of points. When a dielectric is placed in the cavity the wavelength inside the dielectric will be considerably shorter requiring a finer discretisation so further increasing the number of unknowns. If a method that requires a uniform lattice is used then the number of variables can very quickly become unmanageable. In the past the number of unknowns exceeded the computational resources of the majority of computers. Now, however, these problems can be solved on workstation sized computers and in the near future on desktop personal computers.

Even with today's computing resources it is still necessary to carefully consider the algorithms used for computing the fields. There are many obstacles to be overcome before a successful solution can be obtained. Work carried out by many workers in the field of computational electromagnetics in the last couple of decades has provided many successful techniques for overcoming these obstacles. The development of edge elements, for example, has allowed analysts to overcome what Bossavit [1990] refers to as the "plague of spurious modes" that prevented the accurate solution of many high frequency electromagnetic problems. The state of the art in computational electromagnetics is advancing rapidly with hundreds of papers being published every year describing new techniques, enhancements to old techniques, new implementations and new applications of existing methods. Described below are some of the methods that are currently employed to solve microwave heating type problems. This thesis will concentrate on the application of the finite element method. Although this is by no means the only choice, the author considers it to be best suited to the particular problem of microwave heating when compared to other available numerical techniques.

Numerical models are an extremely useful tool for the study of heating effects in microwave systems. The ability to analyse the effect of small changes in geometry or dielectric properties gives an idea of the sensitivity of the system to a variety of parameters. While this may mean running repeated solutions to a particular problem it is greatly preferable to repeated experimentation. To effect a significant change in the cavity dimensions, for example, may be the work of an instant for the computational model whereas for the experimentalist it may require the construction of a new cavity which is both expensive financially and time consuming. With this in mind an alternative approach to the numerical solution has been presented by Chaussecourte *et al.*

[1991]; if the modes were known for a given system then it may be possible to quickly optimise certain parameters such as feed position and to identify the sensitivity of the system to changes in frequency. Having determined the eigenvectors of each mode it is necessary to calculate the degree to which they are excited by the source. The calculation of the eigenvalues and eigenvectors of a very large system is a non-trivial problem [Parlett, 1980]. The situation can be alleviated somewhat by calculating only the higher eigenvalues [Lee & Mittra, 1992], however, many will need to be found and stored which this makes this method unattractive.

Another possible way of determining the sensitivity of the system to frequency is to perform the calculation in the time domain. By exciting the system with a Gaussian pulse, a technique long established in FDTD and TLM calculations [Ma *et al.*, 1994], the simultaneous calculation of the field pattern at a number of frequencies can be carried out. The use of finite elements rather than finite differences or TLM allows the full advantages of recent developments in mesh generation [George, 1991] to be taken rather than being restricted to cartesian grids. For multimode cavities this technique is considerably more efficient than performing multiple solutions in the frequency domain. Both the time domain and frequency domain methods are presented here and comparisons of their effectiveness given in Chapters 5 and 6.

It is also worth noting here that we have to consider the accuracy to which the resonant modes are being calculated. This applies to both calculations that find the resonant frequencies of the modes explicitly and to methods that find field distributions which will be a summation of the modes. In three dimensional problems the mesh size will be ultimately limited by computational constraints: the mesh cannot be refined indefinitely. Many workers involved in calculating the eigenvalues directly produce solutions for which two to three percent accuracy is considered to be acceptable. However, if we specify a single operating frequency, say 2.45 GHz, and somehow calculate the field distribution it can be seen that a small error in the resonant frequencies will cause a completely different set of modes to be excited, thus producing a distinctly different answer. When dealing with empty or lightly loaded cavities extreme care needs to be taken if the results are to be at all meaningful.

1.4.1 Analytical Methods

It is sometimes possible to gain some information about a system by using an analytical method, which provides a quick and easy means of evaluation. Applicators with simple geometries, such as single mode resonant cavities, can be studied analytically. However, since the majority of real systems have complex geometries the amount of information that can be obtained is very limited indeed. For example, inhomogeneously loaded multi-mode cavity applicators cannot be analyzed this way. The special case of a slab loaded rectangular cavity has seen attempts at an analytical solution. If the slab extends across the whole cross section of the cavity, so the inhomogeneity is only in one dimension, then analytic expressions for the resonant modes can be found [Paoloni, 1989]. It is then assumed that the source field distribution can be expanded as a Fourier like sum of the modes. However, in his approach no account of the effect of the aperture itself was taken, nor of the evanescent modes present. This configuration, of a slab loaded cavity is unusual in real situations and so the method is of very limited value.

1.4.2 Numerical Methods

There are many numerical methods that can be used to solve Maxwell's equations in three dimensions, each having its own advantages and disadvantages being better suited to particular types of problem [Yamashita, 1990]. This thesis considers the particular case of microwave heating where lossy dielectrics of arbitrary shape and often with high permittivities will be placed inside a metal enclosure. The surrounding cavity may have a regular shape or it may be irregular. The method must therefore be capable of dealing with complex geometries and wide variations in material properties. Each of the methods considered below has different strengths and limitations, some may be numerically efficient but lack versatility. The important requirements are high speed, low cost and good accuracy. If the method is to be used as an efficient design tool then accurate solutions must be obtained within a reasonable time, without requiring the use of a super-computer.

The differences between the methods are not as clear cut as might at first appear. It is often the situation that a particular method can be seen as a special case of another. For example, it is possible to represent the TLM node as a finite difference expression

[Chen *et al.*, 1991]. The boundary between the finite difference method and the finite element method is similarly blurred [Monk, 1993]. Yee's finite difference time domain scheme, described below, can be derived by considering the problem either as a finite difference one or as a finite volume one. The importance here is to note that it is the underlying assumptions, common to all the numerical methods that are the crucial factor. The finite element method was chosen, although it is more complex to implement than many other methods, because of the greater flexibility that it allows.

Finite difference

The finite difference time domain (FDTD) method [Yee, 1966] has proved to be extremely popular for the solution of Maxwell's equations. This stems from the ease with which it can be programmed, since it uses a regular grid and does not require storage for large matrices. The FDTD method divides the region into two meshes of small cuboids offset from each other, one is used to model the electric field the other the magnetic field. The differential equations are then approximated by replacing the differential operators with difference expressions. The electric and magnetic fields are then solved for alternately in time: the electric field at a time t is used to find the magnetic field at time $t + \Delta t/2$ which in turn is used to find the electric field at $t + \Delta t$ and so on. The solution can then proceed from some initial condition to a steady state solution. The "leap-frogging" scheme is an explicit one and no matrix inversion is required, however, the time step, Δt, needs to be very short in order to ensure stability, which is governed by the Courant condition [Taflove, 1988];

$$\frac{1}{c\Delta t} \geq \sqrt{\frac{1}{(\Delta x)^2} + \frac{1}{(\Delta y)^2} + \frac{1}{(\Delta z)^2}} \tag{1.3}$$

where Δx, Δy and Δz are the spatial divisions in the x, y and z directions respectively and c is the local speed of light. Solution in the time domain requires that the excitation of the system is via a current sheet placed in the waveguide feed, consequentially it is necessary to place an absorbing boundary behind the source plane in order to absorb reflected waves [Iskander *et al.*, 1994]. This is also true for finite element time domain methods and is discussed further in §2.5.

One of the biggest advantages of the FDTD method, namely its simplicity due to the regular nature of the grids, is also its biggest disadvantage. It has been demonstrated that to achieve good accuracy with a non-conforming mesh, that is one that does not follow the boundary of the problem exactly, requires considerably finer meshes than when the mesh conforms to the boundary [Holland, 1993]. Since all objects have to be modelled using rectangular blocks a circular load will have a circumference that is made up of a series of steps. These steps can produce reflections that do not occur in practice. Also, it is difficult to get sufficient spatial accuracy when regular grids are used. If a cell size of, say, 1cm is used (which corresponds to one twelfth of a free space wavelength at 2.45 GHz) then the cavity and load geometry must conform to this grid. However, it is well known that a change in dimension of a few millimeters can significantly change the results in a multimode cavity [Sundberg, 1994]. Thus to ensure good spatial accuracy it may be necessary to use a discretisation that is considerably finer than that required if just a criteria of points per wavelength were considered. This has a further consequence that can be seen from equation (1.3), the finer mesh will require a shorter time step further increasing the computation time. When modelling microwave heating it is desirable to use a fine mesh in the dielectric region where the wavelength may be one tenth of that in the air. Since the dielectric forms only a small fraction of the volume being meshed the use of a fine mesh everywhere adds considerably to the computational cost. While techniques have been developed that allow irregular grids to be used with the FDTD method these increase the complexity of the method enormously [Huang *et al.*, 1994].

The FDTD method has been used by several workers to model microwave heating. Iskander [1993], Huang *et al.* [1994] and Iskander *et al.* [1994] have all used this method extensively for the analysis of the sintering of ceramic materials. More recently Liu *et al.* [1994] and Sundberg [1994] have applied it to the general problem of microwave heating.

Method of lines

The method of lines is a variant of the finite difference method. Maxwell's equations are combined to form the wave equation then the difference operators are applied to the spatial derivatives, leading to a set of time dependent ordinary differential equations.

These are then solved by a numerical procedure, such as explicit fourth order Runge-Kutta. It still suffers from many of the same drawbacks as the standard finite difference techniques that were mentioned above. This method has been used by Fu & Metaxas [1994] for modelling a microwave applicator.

Transmission Line Matrix (TLM) method

In this method the field problem is converted to an equivalent three dimensional network problem. The volume is divided into a lattice where each cell consists of a transmission line connecting the nodes at its corners [Akhtarzad & Johns, 1975; Hoefer, 1985]. The circuit representation seems to be particularly convenient for certain type of numerical simulations. For microwave cavities, however, a very fine lattice is required in order to model the frequency range correctly. This method has very large memory requirements for three dimensional calculations. Some two dimensional analysis of multimode ovens has been carried out with this method [Desai *et al.*, 1992; Flockhart *et al.*, 1994]. This method again suffers from some of the restrictions of the FDTD method; irregular grids cause problems and fine meshes require very small time steps.

Finite Element

The finite element method is one of the most versatile methods available to the numerical analyst. The region being considered is divided up into a number of small elements, each of which has a simple geometry [Silvester & Ferrari, 1990]. The elements are generally tetrahedra or hexahedra for three dimensional problems. Since a regular grid is not required the mesh can conform to the boundaries of the problem. This means that the very fine meshes required with the FDTD and TLM methods are no longer required when modelling complex geometries. Furthermore, the boundaries can be positioned precisely rather than having to be an integer multiple of the spatial step so problems of dimensional accuracy are not encountered. As always there is a price to be paid for this flexibility, in this case the finite element meshes are considerably more complex to construct than the simple ones used for the finite difference technique. Mesh generation is a topic in its own right that has received a great deal of attention [George, 1991], with many commercial mesh generators being available although these are often not ideally suited to microwave heating problems.

For electromagnetic problems the finite element method is normally formulated in the frequency domain, producing a large set of simultaneous equations that require solution. It will be seen that for multimode cavities these equations are often extremely ill-conditioned and so solution is either very time consuming or impossible. This has restricted some workers [Jia & Jolly, 1992] to very coarse meshes that allow a direct solver (see §3) to be used. The coarse meshes, however, produce results that are of very low accuracy. This thesis presents a time domain approach that does not suffer from these problems and is therefore considerably more efficient. The finite element method has also been used [Ayappa *et al.*, 1991] to investigate the temperature dependence of material properties in microwave heated loads. However, only a simple one dimensional approach is taken, where it is assumed that a plane wave is incident on the surface of the material. This situation is unrealistic for practical problems in multimode cavities.

With the finite element method there is a choice of the field variable that is used for the calculation: the electric $\mathbf{E}$, magnetic field $\mathbf{H}$ or the magnetic vector potential $\mathbf{A}$ in conjunction with a scalar electric potential, ψ. Microwave heating requires a knowledge of the power density, which can be determined directly from $\mathbf{E}$. If either $\mathbf{H}$ or $\mathbf{A}$ were used for the calculation then the solution would require differentiation. This is a process that is both prone to error and reduces the rate of convergence on mesh refinement. It is therefore desirable to solve for the electric field directly.

Other problems with the finite element method, such as spurious modes (see §2.1.2) have now been overcome [Bossavit, 1990] making this method extremely attractive for the solution of microwave heating problems. Its ability to use irregular conformal meshes was one of the overriding reasons for the choice of the finite element method in this work. It was seen that if the FDTD or the TLM methods were chosen then a great deal of effort would be required in order to allow them to use irregular grids, whereas the finite element method already allows this in a simple and elegant manner. A further consideration was the ability of the finite element method, when edge elements (see §2.2.2) are used, to model the sharp metal corners that occur around the waveguide aperture. The finite element method is discussed in more detail in Chapter 2.

The finite element method has been used by several authors for modelling multimode cavities. Jia & Jolly [1992] and Jia [1993] use a simple nodal element based approach to analyse multimode applicators, however, they take no account of spurious modes and use very coarse meshes. The results must therefore be treated with caution. Chassecourte *et al.* [1993] used edge elements to model the cavity in the frequency domain, with a Cray computer being used to obtain the results. Other papers comment that their methods can be extended to microwave heating problems without giving any results for multimode cavities.

1.5 Experimentation and Verification

The purpose of the numerical modelling of the applicators is to predict the heating pattern that will be produced in the load. The ultimate validation of the method must therefore lie in comparisons of the predicted distribution with experimental evidence, however, such a comparison presents a number of difficulties. Microwave systems are often very sensitive to small changes in the dimensions, frequency and dielectric properties so it is vital to ensure that the system being modelled accurately corresponds to the experimental system. While the precise measurement of the geometry may be straight forward, irregularities such as seals around openings or internal fixings may be impossible to incorporate into the model so providing a potential source of discrepancy. Dielectric properties pose more of a problem. Two different methods were used for the purpose of this thesis: a cavity perturbation technique [de Jongh, 1989] and a commercial dielectric measurement probe. The former method being suitable for materials with a low value permittivity while the latter was used for high loss food-like materials.

A further difficulty with experimental systems is associated with the ability to accurately measure the quantities of interest. The measurement of the electric field distribution inside the cavity is a notoriously difficult problem, for which many suggestions have been made. Fibre optic probes are available to measure the magnitude of the electric field at a given point, however, a large number of measurements need to be taken in order to obtain the field distribution. The time taken for each measurement may be as long as ten seconds during which time the field distribution may change. Also if the measurement is carried out at high power then after a couple of measurements the load will have heated sufficiently to change its dielectric properties. This makes these probes unsuitable for distribution measurements. Other methods include placing temperature sensitive material such as liquid crystal coated plastic film or thermal paper into the cavity. These are then heated, either directly or indirectly, by the microwave energy and indicate by means of a colour change the presence of strong field concentrations. While providing a better method of obtaining the distribution than a single probe they suffer from the disadvantage of perturbing the field. Whether this perturbation is significant or not depends heavily on the particular details of the method used.

Another approach that is commonly taken and will be used later in this thesis, is to measure the temperature rise in the load that is being heated. This can be done using fibre-optic probes that are microwave transparent while the load is being heated in the applicator or alternatively by using infra-red thermography to measure surface temperatures after the load has been heated. These techniques provide useful information but are limited in scope. The fibre optic probes are limited to measuring the temperatures at only a few points within the material. The thermal camera can only record surface temperatures and taking measurements while the load is being heated is difficult.

1.6 Computer Implementation

The algorithms in this thesis have been implemented as a computer program written in C++. The program is designed to run on a Sun Sparc-10 workstation and is capable of using either the time domain or frequency domain finite element methods that will be described in Chapter 2. C++ was chosen because it allows an object oriented approach to program design. The finite element method is particularly suitable for this approach.

Chapter

2

Finite Element Method: Electromagnetic Field Calculation

2.1 Introduction

The finite element method is a powerful tool for solving partial differential equations over irregularly shaped regions [Silvester & Ferrari, 1990]. The solution domain is divided into a number of sub-domains or elements each having simple geometry. The dependent variable is then represented within that element by a simple function. An equivalent discretized model for each element is constructed and the contributions from all elements to the system are assembled. The overall solution is therefore approximated by a summation of simple functions. The use of elements having a variety of shapes and sizes allows for irregularly shaped boundaries to be modelled accurately. Each element is treated individually so inhomogeneous regions can be handled in a straight forward manner: each element is assigned a material property and the material is assumed to be homogeneous inside the element.

Considerable attention has been paid by workers in the field to the finite element analysis of high frequency electromagnetic systems. The work carried out on closed problems generally falls into three categories:

- Two and three dimensional analysis of waveguides with complex geometries.
- Three dimensional eigen-analysis to predict modes in waveguides and cavities.

- Prediction of power density in lossy dielectrics.

The first two categories constitute the majority of work that has been carried out to date, for a survey see Davis [1993] or Rahman *et al.* [1991]. The work generally deals with waveguide systems containing lossless and irregularly shaped dielectric insertions, one of the primary interests being to determine the propagation constant of the various modes. Calculations in cavities have been carried out, but again this has mainly been to find the resonant modes, eigenvalues, of lossless resonators. Microwave heating requires a knowledge of the total field pattern produced rather than simply the frequencies of the individual modes. However, many of the techniques that have been developed in other areas of computational electromagnetics can be applied directly to microwave heating problems. Webb [1981] outlines the basic method for calculating the magnetic field for a microwave system using elements with node based expansion functions in the presence of lossy dielectrics, however, computational restrictions confine his attention to waveguide problems. The problem of spurious modes is common to many finite element solutions of electromagnetic problems. Section 2.1.2 discusses the origin of these modes and the techniques that can be used to either suppress or to eliminate them.

One of the major difficulties encountered when studying large cavities is the sheer number of unknowns than must be used in order to accurately represent the field, producing a very large system of algebraic equations. In the conventional frequency domain approach their efficient solution is made virtually impossible for some multimode cavity problems because of ill-conditioning. This dissertation presents a time domain finite element method that overcomes this problem of ill-conditioning. To the author's knowledge this is the first time that the time domain finite element method has been applied to microwave heating. For multimode resonant cavities this proves to be considerably more efficient as well as providing other benefits, such as the ability to solve for more than one frequency simultaneously. The two approaches, frequency domain and time domain are outlined in this chapter. Only a brief description of the theory for the frequency domain method is given here as there are numerous detailed descriptions elsewhere, see for example Silvester & Ferrari [1990]. The time domain method is discussed in greater depth since the particular application is new.

2.1.1 GOVERNING EQUATIONS

The time dependent Maxwell's equations that govern the electromagnetic fields in the applicator are,

$$\begin{aligned}\nabla \times \mathbf{H} &= \left(\epsilon\frac{\partial}{\partial t} + \sigma_e\right)\mathbf{E} + \mathbf{J}_s, &(2.1)\\ \nabla \times \mathbf{E} &= -\mu\frac{\partial \mathbf{H}}{\partial t}, &(2.2)\\ \nabla \cdot \mathbf{D} &= \rho_c, &(2.3)\\ \nabla \cdot \mathbf{H} &= 0, &(2.4)\end{aligned}$$

where $\mathbf{J}_s$ is the current density due to sources in the domain, $\mathbf{E}$ and $\mathbf{H}$ are the electric and magnetic field strengths respectively and $\mathbf{D}$ is the electric flux density. These equations are then supplemented by appropriate boundary conditions, the simplest essential boundary condition being,

$$\mathbf{n} \times \mathbf{E} = 0 \qquad \text{on } \Gamma, \tag{2.5}$$

corresponding to a perfect electrical conductor over the surface Γ.

By eliminating $\mathbf{H}$ from equations (2.1) and (2.2) the wave equation is obtained;

$$\nabla \times \frac{1}{\mu}\nabla \times \mathbf{E} + \sigma_e\frac{\partial \mathbf{E}}{\partial t} + \epsilon\frac{\partial^2 \mathbf{E}}{\partial t^2} = -\frac{\partial \mathbf{J}_s}{\partial t}, \tag{2.6}$$

on which the time domain formulation is based.

If the fields are assumed to be time harmonic, such that $\mathbf{E} = \mathbf{E}_0 e^{\jmath\omega t}$, then equations (2.1) and (2.2) become,

$$\begin{aligned}\nabla \times \mathbf{H} &= \jmath\epsilon^*\omega\mathbf{E} + \mathbf{J}_s, &(2.7)\\ \nabla \times \mathbf{E} &= \jmath\mu\omega\mathbf{H}. &(2.8)\end{aligned}$$

where $\epsilon^* = \epsilon_0(\epsilon' - \jmath\sigma_e/\epsilon_0\omega)$. Elimination of $\mathbf{H}$ from (2.7) and (2.8) gives the vector Helmholtz equation;

$$\nabla \times \frac{1}{\mu}\nabla \times \mathbf{E} - \omega^2\epsilon^*\mathbf{E} = -\jmath\omega\mathbf{J}_s. \tag{2.9}$$

which is used for the frequency domain discretisation.

2.1.2 Spurious modes

Spurious modes are non-physical solutions that can occur in numerical calculations and corrupt the true result. Their presence in numerical solutions to electromagnetic problems has been known for some time and has prompted the development of a multitude of different techniques for their elimination or suppression[1]. The reasons for the occurrence of these spurious modes, which are characterized by a non-zero divergence, is now well understood [Wong & Cendes, 1988; Pinchuk *et al.*, 1988; Lynch & Paulsen, 1991; Schroeder & Wolff, 1994]. Their presence stems from the improper approximation of the null-space of the *curl* operator. The double *curl* equation (2.9) has an infinite number of solutions at zero frequency, that is $\nabla \times \mathbf{E} = 0$ which have the form $\mathbf{E} = -\nabla\phi$, where ϕ is a scalar field.

When traditional elements with node based expansion functions are used to model the field, many of the $-\nabla\phi$ modes are very poorly approximated, consequently they no longer have zero frequency and become mixed with the true modes. They are then indistinguishable from the physical modes in eigenvalue computations and corrupt the solution in driven problems. For elements with node based expansion functions the most popular method of eliminating these modes is to add a penalty term $p\nabla(\nabla \cdot \mathbf{E})$ to the weak form (2.16), where p is a parameter to be chosen [Hara *et al.*, 1983]. This enforces the divergence condition in a least squares way, thereby reducing the number of zero frequency modes. Paulsen & Lynch [1991] analyse this method and conclude that the only correct choice for p is unity, which corresponds to solving the Helmholtz equation

$$\nabla^2\mathbf{E} + \omega^2\mu\epsilon^*\mathbf{E} = 0, \tag{2.10}$$

in homogeneous regions where $\mathbf{J}_s = 0$. Since the divergence condition is then explicitly included the spurious modes are eliminated. A simple example given by Collin [1991] shows that enforcing the divergence removes the spurious modes but the new functional gives a poorer approximation to the physical modes because of the extra constraint imposed. This is further demonstrated by results at the end of this chapter.

An alternative method of eliminating the problem of spurious modes is to model the null space of the *curl* operator more accurately. The $-\nabla\phi$ modes are then approxi-

---

[1] See for example Koshiba *et al.* [1987] and Davis [1993] for a summary of methods.

mated correctly, *i.e.* with zero frequency, and so are not mixed with the physical modes. This can be achieved by the use of a C^1 mesh or C^1 finite elements [Wong & Cendes, 1988]. These two methods are undesirable for general problems since they increase the complexity of the problem considerably. Edge elements, which are described in the next section, have also been shown to provide a good approximation to the null space of the *curl* [Webb, 1993; Zhu *et al.*, 1994]. Spurious modes have not been observed when they are used for the discretisation. However, the many zero frequency modes are present in an eigen analysis but these are easily identified [Zhu *et al.*, 1994]. If these modes are well sorted from the physical modes then they should not occur in driven solutions. The results in this thesis suggest that they do not appear in the solutions of driven problems. Edge elements have been chosen for use in this work partly because of this ability to suppress the spurious modes found when other elements are used.

2.2 Finite Element Discretisation

In order to permit solution of equation (2.16) on a computer it is necessary to approximate the infinite dimensional space by a finite dimensional one. The degree to which the approximation succeeds depends upon how closely the discrete structure mimics the infinite dimensional continuous one [Bossavit, 1988a]. This section discusses some of the choices for the discretisation.

2.2.1 Traditional Nodal Elements

The common approach to the discretisation has been to use standard finite elements with node based expansion functions. These have been found to work well for scalar fields and have consequently been adapted to vector fields by simply replacing the single degree of freedom at each node by three [Silvester & Ferrari, 1990]. These conventional elements, however, suffer from a number of disadvantages:

- Normal continuity is enforced, even when the field should be discontinuous, such as at an interface between two materials with differing material properties.
- The essential boundary condition $\mathbf{n} \times \mathbf{E} = 0$ is difficult to implement when the boundary is not parallel to one of the co-ordinate axis, or at convex corners.

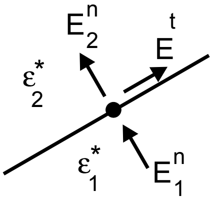

Figure 2.1: Interface condition at the boundary between two dielectrics.

- Special precautions have to be taken to avoid spurious modes, as discussed previously (see §2.1.2).
- Problems are encountered when sharp metal corners are present, such as those that occur around the waveguide feed where it enters the cavity.

The rigorous enforcement of the normal continuity prevents solution in **H** when μ is discontinuous and in **E** when ϵ^* is discontinuous. For most heating applications μ is constant so it would be possible to solve for **H**, which has been done by Jia & Jolly [1992]. It is then necessary to differentiate the solution to obtain **E** since the power density, given by

$$p_v = \frac{1}{2}\sigma_e|\mathbf{E}|^2, \tag{2.11}$$

is ultimately required. The differentiation process, however, may introduce extra errors into the solution and is therefore undesirable [Silvester & Omeragić, 1993]. It is preferable to solve for **E** directly, however, as ϵ^* will almost certainly be discontinuous a special treatment is needed at dielectric interfaces if nodal elements are to be used.

Paulsen *et al.* [1987] suggest that two variables can be used for the normal component of the field at dielectric interfaces. These are related by the continuity relation $\epsilon_1^*\mathbf{E}_1^n = \epsilon_2^*\mathbf{E}_2^n$, where the subscripts 1 and 2 refer to quantities on either side of the boundary, as shown in Figure 2.1. When the normal does not lie along one of the co-ordinate axis it is necessary to rotate the co-ordinate system local to the node. This method has the obvious disadvantage that the normal is multiply defined at corners and that it cannot take account of boundaries between more than two different dielectrics. In two dimensions a method has been proposed for implementing boundary conditions at the interface between several dielectrics, however, it does not appear to be easily extensible into three dimensions [Paulsen *et al.*, 1987]. In materials which have temperature dependent properties and the electromagnetic field is being solved in conjunction with the thermal field, every element may have slightly different material properties. This method is therefore not suitable for the problems considered in this thesis. It has been suggested [Webb *et al.*, 1983] that nodal elements be used without any modification, which effectively smooths the transition between dielectrics. Unfortunately, if this approach were taken then convergence with successive mesh refinement cannot be guaranteed [Bossavit, 1990]. Furthermore, the food-like materials being heated often have very large permittivities which cause large reflections from the surface of the load. If the transition between dielectrics were "blurred" in this way it would reduce these reflections in an artificial way.

An alternative method has been proposed by Mur [1988], who uses linear edge elements along dielectric interfaces to allow the normal component of the field to jump while still using nodal based elements in homogeneous regions. This approach is claimed to provide the flexibility of edge elements coupled with the accuracy and economy of nodal elements. The use of edge elements is discussed in the next section. Both of these approaches require the divergence to be specified in the formulation as a penalty function in order to suppress spurious modes.

A further disadvantage of elements using node based expansion functions is their inability to model sharp metal corners. To overcome this it has been suggested that the polynomial expansion functions are supplemented by singular ones near to a metal corner [Webb, 1988]. These can then accurately model the field distribution, however, the extension to three dimensions appears to be less than straightforward. An alternative proposed by Bardi *et al.* [1994a] is to use edge elements near to sharp metal corners and nodal elements in the body of the domain. This approach is similar to that of Mur's for dealing with dielectric discontinuities.

2.2.2 EDGE ELEMENTS

The unsatisfactory performance of elements using node based expansion functions in many electromagnetic applications has prompted the search for an alternative representation of the field within an element. Such elements exist and are generally termed

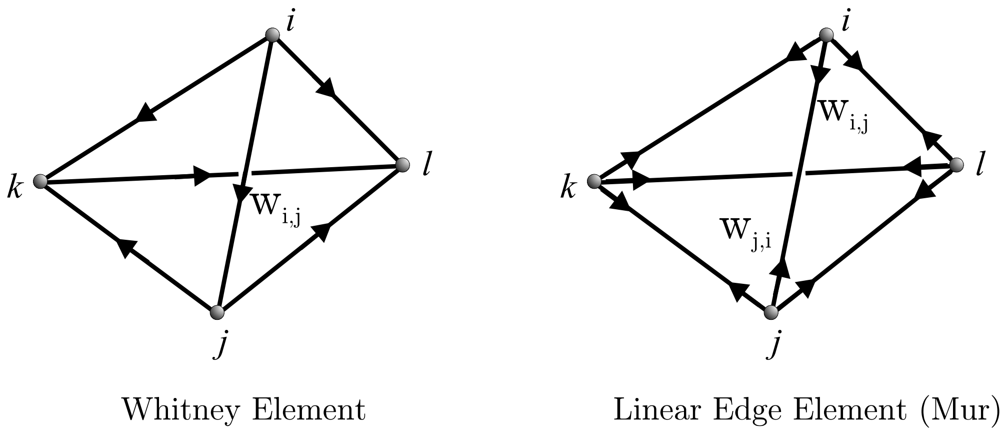

Figure 2.2: Degrees of freedom for Whitney and linear edge elements

vector elements or edge elements because the degrees of freedom are associated with the circulations of the field along the edges of the element rather than with the nodes. Vector finite elements were first proposed by Raviart & Thomas [1977] for the solution of two dimensional fluid flow problems, and were subsequently extend to three dimensional Maxwell's equations by Nédélec [1980]. Bossavit [1988b] related Nédélec's elements to the differential forms proposed by Whitney [1957] which have a structure closely resembling that of Maxwell's equations when the field quantities are expressed as differential forms. It has been argued that differential forms provide a more natural representation of Maxwell's equations than the more common vector field approach [Deschamps, 1981; Baldomir, 1986; Hammond & Baldomir, 1988]. These elements are therefore well suited to the solution of Maxwell's equations.

Edge elements differ from nodal elements in that the degrees of freedom are associated with the edges of the element rather than with the nodes, a consequence of which is that they only impose tangential continuity at the element boundaries leaving the normal component free to jump. This allows edge elements to model either **E** or **H** when both μ and ϵ^* are discontinuous throughout the domain. At sharp corners the normal component of the field is not explicitly prescribed. This extra freedom allows edge elements to correctly model the behaviour surrounding a corner Webb [1993].

For first order tetrahedral elements the basis function associated with an edge having vertices i and j is given by,

$$\mathbf{w}_{i,j} = \lambda_i \nabla \lambda_j - \lambda_j \nabla \lambda_i \tag{2.12}$$

where λ_i is the barycentric function associated with node i [Bossavit, 1988b], as shown in Figure 2.2. The elements proposed by Nédélec have basis functions that vary linearly within the element, however, they are constant along an edge. This lack of first order completeness has caused suspicions about the accuracy of edge elements among some workers [Mur, 1994] and has prompted the design of consistently linear edge elements [Mur & Dehoop, 1985; Nédélec, 1986] which have two degrees of freedom per edge,

$$\mathbf{w}_{i,j} = \lambda_i \nabla \lambda_j \qquad \text{and} \qquad \mathbf{w}_{j,i} = \lambda_j \nabla \lambda_i. \tag{2.13}$$

While the interpolation function is now linear along each edge as well as in the body of the element, it is at the expense of doubling the number of degrees of freedom. Furthermore, linear edge elements approximate the *curl* in an identical way to Whitney elements. This can be seen by rewriting the two basis functions for the edge i, j as,

$$\begin{aligned} \mathbf{w}^a_{i,j} &= \mathbf{w}_{i,j} - \mathbf{w}_{j,i} &&= \lambda_i \nabla \lambda_j - \lambda_j \nabla \lambda_i, \\ \mathbf{w}^b_{i,j} &= \mathbf{w}_{i,j} + \mathbf{w}_{j,i} &&= \lambda_i \nabla \lambda_j + \lambda_j \nabla \lambda_i = \nabla(\lambda_i \lambda_j). \end{aligned} \tag{2.14}$$

$\mathbf{w}^a_{i,j}$ is identical to the Whitney element basis function, while $\mathbf{w}^b_{i,j}$ has a *curl* which is identically zero. Linear edge elements are claimed to be more accurate than the Whitney elements, and to have a local approximation error of $O(\mathrm{h}^2)$ compared to $O(\mathrm{h})$ for Whitney elements [Mur, 1994], a claim which has recently been challenged [Bossavit, 1994]. Monk [1992] shows that Whitney elements do have a linear dependence upon h compared to a quadratic dependence for linear edge elements when measured with the ℓ_2-norm, however, when the discrete maximum norm is used instead both types of elements produce $O(\mathrm{h}^2)$ convergence with Whitney elements being consistently more accurate for a given number of unknowns. Results comparing the accuracy of the two types of elements are given in §2.7, where Monk's observations are confirmed. It has recently been shown [Bossavit, 1994] that while first order completeness gives nice smooth solutions it is not a prerequisite for achieving accurate answers.

The form (2.14) is that given by Webb & Forghani [1993] who proposed a family of hierarchal edge elements. This allows Whitney elements to be used in some regions and higher order edge elements in others where a greater accuracy is required. The family proposed by Webb extends to elements that are complete to degree two. This representation, which for the first order element is the same as (2.14), is therefore more convenient than (2.13) in certain situations. Alternative implementations of edge elements have been proposed [Barton & Cendes, 1987], which use a different representation of the interpolation function, namely

$$\mathbf{w}_{i,j} = \alpha \times \mathbf{r} + \beta, \tag{2.15}$$

where α and β are constant vectors chosen so that the tangential component of $\mathbf{w}_{i,j}$ vanishes on all edges other than i, j while $\mathbf{r}$ is the position vector inside the element. The basis function (2.15) is mathematically equivalent to Whitney elements, however, it is not as convenient to programme.

It is often convenient to use shapes other than tetrahedrons for discretising the problem. This is often due to constraints imposed by the mesh generating software which is often not capable of generating tetrahedral meshes directly. One answer, of course, would be to use software that has this facility but when this is not available other methods must be found. A mesh consisting of hexahedra can be broken up so that each hexahedron is replaced by five tetrahedra [Webb, 1981]. However, this requires that the hexahedral mesh is fairly regular, otherwise conflicts at element faces are encountered where elements on either side do not match. An alternative is to break each hexahedron into twelve tetrahedra by inserting an extra node in the centre of the hexahedron. This has the disadvantage of creating considerably more elements. It can therefore be desirable to use hexahedral edge elements so that the hexahedral mesh can be used unmodified. When the geometry is suitable it is possible to extrude a two dimensional triangular mesh into three dimensions so producing prism elements. This technique is used for the TM_{010} cavity analysed in Chapter 5. The method for creating hexahedral elements was outlined by van Welij [1985], however, this author has not seen a complete listing of the shape functions for hexahedral and prismatic edge elements so these are given in Appendix A.

2.3 Frequency Domain Finite Element Method

Solution of Maxwell's equations in the frequency domain via the finite element method is now a well established technique [Silvester & Ferrari, 1990]. The frequency domain discretisation using edge elements is briefly repeated here for clarity before proceeding to the time domain formulation.

To derive a weak formulation suitable for solution by the finite element method equation (2.9) is multiplied by an arbitrary function $\psi \in \mathcal{H}_\prime(\text{curl})$ and integrated over the volume of the domain Ω. Integration by parts of the curl term then leads to,

$$\int_\Omega \frac{1}{\mu} \nabla \times \mathbf{E} \cdot \nabla \times \psi \, \mathrm{d}\Omega - \omega^2 \int_\Omega \epsilon^* \mathbf{E} \cdot \psi \, \mathrm{d}\Omega = -\int_\Omega \jmath\omega \mathbf{J}_s \cdot \psi \, \mathrm{d}\Omega \qquad \forall \psi \in \mathcal{H}_\prime(\text{curl}). \tag{2.16}$$

It then remains to find $\mathbf{E} \in \mathcal{H}_\prime(\text{curl})$. This weak form (2.16) is identical to the variational functional used by many workers, for example [Silvester & Ferrari, 1990]. This expression has been extensively analysed [Leis, 1977; Bossavit, 1990; Monk, 1992]. To discretise (2.16) using edge elements the continuous field, $\mathbf{E}$ is replaced by

$$\mathbf{E} = \sum_{i=1}^{N} \mathbf{w}_i e_i. \tag{2.17}$$

where e_i corresponds to the circulation of the field along edge i. This leads to the matrix equation,

$$\left([\mathbf{S}] - k^2[\mathbf{T}]\right) \mathbf{e} = 0 \tag{2.18}$$

where $\mathbf{e}$ is the vector of values corresponding to the circulations of the field along each edge and $k^2 = \omega^2 \epsilon_0 \mu_0$. The matrices corresponding to an individual element are;

$$[\mathbf{S}]^e{}_{i,j} = \int_{\Omega_e} \{\nabla \times \mathbf{w}_i \cdot \nabla \times \mathbf{w}_j\} \, \mathrm{d}\Omega_e \tag{2.19}$$

$$[\mathbf{T}]^e_{i,j} = \epsilon_r \int_{\Omega_e} \{\mathbf{w}_i \cdot \mathbf{w}_j\} \, \mathrm{d}\Omega_e. \tag{2.20}$$

These matrices are given explicitly for tetrahedral Whitney elements by Lee & Mittra [1992]. The electric field distribution can then be obtained directly from a solution of (2.18) after the appropriate boundary conditions (see §2.5) have been applied. Methods for solving the set of simultaneous equations are discussed in Chapter 3.

2.4 Time Domain Finite Element Method

2.4.1 INTRODUCTION

The time domain finite element method is generally only used when transient behaviour is being investigated otherwise the fields are assumed to be time harmonic so the frequency domain approach is used. The development of fast iterative solution techniques such as the pre-conditioned conjugate gradient method has made the frequency domain approach even more attractive for many problems [Paulsen *et al.*, 1992]. However, multimode cavities which possess many resonances, often produces a system of very ill-conditioned equations in the frequency domain. It is therefore desirable to switch to the time domain in order to circumvent the problems associated with solving systems of very ill-conditioned equations.

The finite element method is well suited to solutions in the time domain. When applying it to Maxwell's equations there are two approaches that can be taken:

- Solve the wave equation (2.6) in the time domain for a single field variable, in the present case this will be **E**.
- Use a "leap-frogging" scheme which alternately calculates **E** and **H** from equations (2.1) and (2.2). This method is the finite element equivalent of Yee's scheme with finite differences [Madsen & Ziolkowski, 1988; Ambrosiano *et al.*, 1994].

For modelling microwave applicators the power density is required, so a knowledge of the magnetic field is not necessary. The first option of solving the wave equation for **E** was therefore chosen. The use of edge elements allows the electric field to be modelled in the presence of inhomogeneities. At this point it must be noted that there are a few methods in the literature that use a time domain scheme with edge elements, however, none specifically for microwave heating problems. Chan *et al.* [1994] propose a finite difference scheme that uses Whitney element interpolation functions, this method will have greater restrictions on the meshes used than the finite element method that will be presented here. Monk [1993] analyses a time-domain method based on hexahedra which is then related to Yee's finite difference scheme, however, it is a purely theoretical analysis rather than a practical application and dielectrics are not considered. Lee [1994] presents a time domain method for finding the eigenvalues of a cavity resonator using edge elements, however, lossy dielectrics are not considered.

2.4.2 FORMULATION

The formulation used for the calculations in this thesis proceeds by applying Galerkin's procedure to the equation wave equation (2.6): pre-multiplying by a weighting function $\psi \in \mathcal{H},(\text{curl})$ and integrating over the volume Ω, gives

$$\int_\Omega \{\psi \cdot \nabla \times \nabla \times \mathbf{E}\}\, \mathrm{d}\Omega + \mu_0 \int_\Omega \sigma_e\, \psi \cdot \frac{\partial \mathbf{E}}{\partial t}\, \mathrm{d}\Omega + \epsilon_0 \mu_0 \int_\Omega \epsilon' \psi \cdot \frac{\partial^2 \mathbf{E}}{\partial t^2}\, \mathrm{d}\Omega$$

$$= -\int_\Omega \psi \cdot \frac{\partial \mathbf{J}_s}{\partial t}\, \mathrm{d}\Omega. \qquad (2.21)$$

The using Green's vector identity and the divergence theorem yields

$$\begin{aligned}
\int_\Omega (\nabla \times \psi) \cdot (\nabla \times \mathbf{E})\, \mathrm{d}\Omega &+ \mu_0 \int_\Omega \sigma_e \psi \cdot \frac{\partial \mathbf{E}}{\partial t}\, \mathrm{d}\Omega + \epsilon_0 \mu_0 \int_\Omega \epsilon' \psi \cdot \frac{\partial^2 \mathbf{E}}{\partial t^2}\, \mathrm{d}\Omega \\
+ \int_\Omega \psi \cdot \frac{\partial \mathbf{J}_s}{\partial t}\, \mathrm{d}\Omega &= \iint_\Gamma \psi \cdot (\mathbf{n} \times \nabla \times \mathbf{E})\, \mathrm{d}\Gamma \\
&= -\mu_0 \iint_\Gamma \psi \cdot \left(\mathbf{n} \times \frac{\partial \mathbf{H}}{\partial t}\right) \mathrm{d}\Gamma. \qquad (2.22)
\end{aligned}$$

Since both $\mathbf{H}$ and $\partial \mathbf{H}/\partial t$ are continuous, the surface integral on the right of equation (2.22) will cancel at all inter-element boundaries. The system is discretized in the same fashion as before, with the field quantities and weighting function replaced respectively by,

$$\mathbf{E} = \sum_{i=1}^{N} \mathbf{w}_i e_i \qquad \text{and} \qquad \psi = \sum_{i=1}^{N} \mathbf{w}_i. \qquad (2.23)$$

This leads to the matrix equation

$$[\mathbf{S}]\mathbf{e} + [\mathbf{T}_\sigma] \frac{\partial \mathbf{e}}{\partial t} + [\mathbf{T}_\epsilon] \frac{\partial^2 \mathbf{e}}{\partial t^2} = \mathbf{b}, \qquad (2.24)$$

where the element matrices are defined by

$$[\mathbf{S}]^e_{i,j} = \int_{\Omega_e} (\nabla \times \mathbf{w}_i) \cdot (\nabla \times \mathbf{w}_j)\, \mathrm{d}\Omega_e, \qquad (2.25)$$

$$[\mathbf{T}_\sigma]^e_{i,j} = \sigma_e \mu_0 \int_{\Omega_e} (\mathbf{w}_i \cdot \mathbf{w}_j)\, \mathrm{d}\Omega_e, \qquad (2.26)$$

$$[\mathbf{T}_\epsilon]^e_{i,j} \;=\; \epsilon_0\epsilon'\mu_0 \int_{\Omega_e} (\mathbf{w}_i \cdot \mathbf{w}_j)\, \mathrm{d}\Omega_e. \tag{2.27}$$

Matrices (2.25) to (2.27) are similar to the matrices (2.19) and (2.20) obtained for the frequency domain discretisation of the vector Helmholtz equation. The matrix $[\mathbf{S}]$ is identical, whereas $[\mathbf{T}_\epsilon]$ is the real part of (2.20) multiplied by μ_0 and $[\mathbf{T}_\sigma]$ is the imaginary part multiplied by $-\mu_0\epsilon_0\omega$. Finally, the vector $\mathbf{b}$ in equation (2.24) is the forcing vector which represents the surface integral term of equation (2.22) and the source current density terms. In practice the surface integral is only evaluated where an absorbing boundary condition is required (see §2.5.1).

To solve the equations (2.24) it is necessary to discretise the temporal derivatives. Lee [1994] uses the θ–method when using the time domain finite element method to find the resonances of a lossless cavity. This method produces a system which is only conditionally stable, which makes it necessary to choose a very small time step in order to obtain convergence. If an implicit scheme is used for the discretisation a much greater choice over the time step is allowed. The Newmark method, which is commonly used for the solution of the dynamic vibration equation [Wood, 1990], was chosen because the algorithm can be controlled through two parameters, γ and β to give either an implicit or an explicit scheme. With an appropriate choice of these parameters the system is unconditionally stable and has second order accuracy in time. This allows the time step to be chosen in order to give a particular accuracy without being constrained by the stability criteria. It is to be noted that the time domain finite element method requires the solution of a set of simultaneous equations at each time step for both implicit and explicit methods unless lumping (see §2.4.4) is used. The use of an implicit scheme does not significantly increase the computational effort required at each time step over that required for an explicit scheme. This is contrary to the FDTD methods based on Yee's scheme which do not require any matrix inversions when used with an explicit method, consequently an implicit scheme is rarely used with such methods.

The choice of $\gamma = 0.5$ and $\beta = 0.25$ produces a system that is unconditionally stable with an accuracy of $O(\Delta t^2)$ (see §2.4.3). The time step, Δt, can then be chosen to provide the accuracy required. With $\gamma = 0.5$ and $\beta = 0$ the Newmark method is equivalent to using central differences for the temporal derivatives which have second order accuracy but only conditional stability, however, since the method is explicit lumping can be used to diagonalize the matrices $[\mathbf{T}_\sigma]$ and $[\mathbf{T}_\epsilon]$ so reducing the effort required at each time step.

The Newmark method uses the following approximations,

$$\mathbf{e}_{n+1} = \mathbf{e}_n + \Delta t\,\mathbf{f}_n + \frac{\Delta t^2}{2}(1-2\beta)\,\mathbf{g}_n + \Delta t^2\beta\mathbf{g}_{n+1}, \tag{2.28}$$

$$\mathbf{f}_{n+1} = \mathbf{f}_n + \Delta t\,(1-\gamma)\mathbf{g}_n + \Delta t\,\gamma\,\mathbf{g}_{n+1}, \tag{2.29}$$

where $\mathbf{f}_n$ and $\mathbf{g}_n$ are the approximations to the first and second order temporal derivatives of $\mathbf{e}_n$ at time $t = n\Delta t$, and where γ and β are the Newmark parameters. Substituting the derivatives in (2.24) by $\mathbf{f}$ and $\mathbf{g}$ at time $t = (n+1)\Delta t$ produces

$$[\mathbf{S}]\mathbf{e}_{n+1} + [\mathbf{T}_\sigma]\mathbf{f}_{n+1} + [\mathbf{T}_\epsilon]\mathbf{g}_{n+1} = \mathbf{b}_{n+1}. \tag{2.30}$$

Substitution of (2.28) and (2.29) into (2.30) gives

$$\begin{aligned} &\{[\mathbf{T}_\epsilon] + \gamma\Delta t[\mathbf{T}_\sigma] + \beta\Delta t^2[\mathbf{S}]\}\mathbf{g}_{n+1} = \\ &\qquad \mathbf{b}_{n+1} - [\mathbf{T}_\sigma]\{\mathbf{f}_n + \Delta t\,(1-\gamma)\mathbf{g}_n\} \\ &\qquad -[\mathbf{S}]\{\mathbf{e}_n + \Delta t\,\mathbf{f}_n + \frac{\Delta t^2}{2}(1-2\gamma)\mathbf{g}_n\}. \end{aligned} \tag{2.31}$$

which relates $\mathbf{g}$ at time step $n+1$ to quantities at the previous time step. Once $\mathbf{g}_{n+1}$ has been found $\mathbf{f}_{n+1}$ and $\mathbf{e}_{n+1}$ can be determined from (2.28) and (2.29). This method is a single step, three stage algorithm and requires the first and second derivatives to be carried at each time step. It is also necessary to specify $\mathbf{f}_0$ and $\mathbf{g}_0$ as initial conditions. In practice it is more desirable to use a single stage algorithm which only uses values of the field, $\mathbf{e}$. This is given by the two step recurrence relation[2],

$$\begin{aligned} &\{[\mathbf{T}_\epsilon] + \gamma\Delta t[\mathbf{T}_\sigma] + \beta\Delta t^2[\mathbf{S}]\}\mathbf{e}_{n+1} = \\ &\qquad \{2[\mathbf{T}_\epsilon] - (1-2\gamma)\Delta t[\mathbf{T}_\sigma] - (0.5+\gamma-2\beta)\Delta t^2[\mathbf{S}]\}\mathbf{e}_n \\ &\qquad +\{-[\mathbf{T}_\epsilon] - (\gamma-1)\Delta t[\mathbf{T}_\sigma] - (0.5-\gamma+\beta)\Delta t^2[\mathbf{S}]\}\mathbf{e}_{n-1} \\ &\qquad +\Delta t^2\{\beta\mathbf{b}_{n+1} + (0.5+\gamma-2\beta)\mathbf{b}_n + (0.5-\gamma+\beta)\mathbf{b}_{n-1}\}. \end{aligned} \tag{2.32}$$

---

[2] A full derivation of (2.32) is given by Wood [1990].

As mentioned previously it is necessary to solve a matrix equation at each time step, with the matrix being given by $\{[\mathbf{T}_\epsilon] + \gamma\Delta t[\mathbf{T}_\sigma] + \beta\Delta t^2[\mathbf{S}]\}$. This is of the same order as the number of degrees of freedom. For a small number of unknowns an initial LU factorization means that only a single forward and backward substitution is required at each time step, however, in practical cases the number of unknowns makes factorization of the matrix unworkable so an iterative method is called for. Unlike the matrix produced by the frequency domain discretisation (2.18) this matrix is both real and well conditioned so that the pre-conditioned conjugate gradient method can be used to solve the matrix equation in as few as 10 iterations, even for systems which have in excess of 100,000 unknowns. It is found that diagonal pre-conditioning works extremely well in this case [Wathen, 1987]. The number of iterations required by the conjugate gradient method is dependent upon the eigenvalues of the system, a mesh having elements of roughly equal shape will produce a matrix with very few distinct eigenvalues, enabling very fast solution. The Gauss-Seidel method has also been used to solve the equations at each time step. A good approximation to the solution can be obtained from the field values at previous time steps,

$$\mathbf{e}_{n+1} \approx 2\mathbf{e}_n - \mathbf{e}_{n-1}, \tag{2.33}$$

for use as an initial guess which allows rapid solution with this technique. Also, since the matrix is well-conditioned it can be stored using single precision numbers, reducing the computer memory requirements. The different techniques that were used to solve (2.32) are described more fully in Chapter 3.

2.4.3 STABILITY

The characteristic equation for the recurrence relation (2.32) can be obtained by setting $\mathbf{e}_{n+1} = r\mathbf{e}_n$ and $\mathbf{f}_{n+1} = r\mathbf{f}_n$ [Wood, 1990];

$$\begin{aligned}&\{m + \gamma\Delta t\mu + \beta\Delta t^2 k\}r^2\\ &\quad+\{-2m + (1-2\gamma)\Delta t\mu + (0.5+\gamma-2\beta)\Delta t^2 k\}r\\ &\quad+\{m + (\gamma-1)\Delta t\mu + (0.5-\gamma+\beta)\Delta t^2 k\} = 0,\end{aligned} \tag{2.34}$$

where m, μ and k correspond to the eigenvalues of the matrices $[\mathbf{T}_\epsilon]$, $[\mathbf{T}_\sigma]$ and $[\mathbf{S}]$ respectively. For the system to remain stable the modulus of the roots of the characteristic equation (2.34) must be less than or equal to unity. By using the transformation $r = (1+z)/(1-z)$ the unit circle in the r-plane is mapped onto the imaginary axis in the z-plane. This produces an equation

$$a_0 z^2 + a_1 z + a_2 = 0, \tag{2.35}$$

where

$$\begin{aligned} a_0 &= 4m + 2(2\gamma - 1)\Delta t\mu + 2(2\beta - \gamma)\Delta t^2 k && (2.36)\\ a_1 &= \Delta t\mu + (\gamma - 0.5)\Delta t^2 k && (2.37)\\ a_2 &= \Delta t^2 k. && (2.38)\end{aligned}$$

The roots of (2.35) must then lie in the left half of the z-plane for the system to be stable. The Routh-Hurwitz stability conditions can then be used, which correspond to $a_0 > 0$, $a_1 \geq 0$ and $a_2 \geq 0$. If $m, \mu \,\text{and}\, k$ are all positive then the system will be stable for

$$2\beta \geq \gamma \geq 0.5. \tag{2.39}$$

However, if we choose to use an explicit scheme so that $\beta = 0$ we will no longer have unconditional stability. In this case, for $\gamma = 0.5$ equation (2.36) becomes,

$$m - \Delta t^2 k > 0 \tag{2.40}$$

so that,

$$\Delta t^2 < \frac{m}{k}. \tag{2.41}$$

This imposes a restriction on the choice of Δt so that many more time steps will be needed, however, there is a compensation since lumping (see §2.4.4) can be used to render the “mass” matrix diagonal and significantly reduce the amount of work required at each time step. In practice the quantities m and k are given by the eigen-values of the of the $[\mathbf{T}_\epsilon]$ and $[\mathbf{S}]$ matrices respectively. The stability condition therefore becomes

$$\Delta t^2 < \frac{\lambda_{\min}^{T_\epsilon}}{\lambda_{\max}^{S}}, \tag{2.42}$$

where $\lambda_{\mathrm{min}}^{T_\epsilon}$ and $\lambda_{\mathrm{max}}^{S}$ are the minimum and maximum eigenvalues of the $[\mathbf{T}_\epsilon]$ and $[\mathbf{S}]$ matrices respectively. When lumping is used $\lambda_{\mathrm{min}}^{T_\epsilon}$ is simply the smallest diagonal element of $[\mathbf{T}_\epsilon]$ since it is diagonal. $\lambda_{\mathrm{max}}^{S}$ can be found by using a standard method for solving eigen-value problems. Alternatively it is noted by Lee [1994] that,

$$\frac{\lambda_{\mathrm{min}}^{T_\epsilon}}{\lambda_{\mathrm{max}}^{S}} = \frac{1}{\kappa_{\mathrm{max}}} \tag{2.43}$$

where κ is a solution of the generalised eigenvalue problem [Parlett, 1980]

$$[\mathbf{S}]\mathbf{x} = \kappa[\mathbf{T}_\epsilon]\mathbf{x}. \tag{2.44}$$

2.4.4 Lumping

The lumping of the "mass" matrix is a standard technique for problems in structural dynamics, where nodal elements are used. Lumping corresponds to diagonalising the matrices $[\mathbf{T}_\epsilon]$ and $[\mathbf{T}_\sigma]$. If β is then chosen to be zero, the matrix to be inverted at each time step becomes diagonal. The saving in computational effort is generally thought to outweigh the marginal loss in accuracy that results. This choice of β, however, means that the algorithm is now only conditionally stable (see §2.4.3). This has the result of requiring considerably more time steps.

The nature of edge elements makes lumping more difficult than for nodal elements. Lumping techniques, however, have been developed for edge elements by Haugazeau & Lacoste [1993]. With nodal elements, one loses accuracy as the size of the element increases, since for lumping it is assumed that the field value is constant over the element when calculating $[\mathbf{T}]$. With tetrahedral edge elements the shape of the element is also crucial, with the error increasing significantly as the shape is distorted from a regular tetrahedron. Thus, for lumping to work satisfactorily it is necessary to ensure that the elements of the mesh are of a high quality. In practice this means ensuring Delaunay conformity of the mesh, failure to do so can lead to negative entries on the diagonal of the assembled $[\mathbf{T}_\epsilon]$ matrix which, from equation (2.42), will cause the method to become unstable. This puts a much more stringent set of conditions on the mesh generation program. Lumping has been implemented for the present code and used for some problems, however, the restrictions that are imposed upon the mesh have meant that its use has been limited.

2.5 Boundary Conditions

The solution of the finite element equations can only proceed once the boundary conditions have been correctly applied. The walls of the cavity and feed waveguide, shown in Figure 2.3, are assumed to be perfect conductors. Thus on the walls we have,

$$\mathbf{E} \times \mathbf{n} = \mathbf{0}. \tag{2.45}$$

This condition can be applied by setting the values of the electric field corresponding to edges that lie on the boundary to zero [Silvester & Ferrari, 1990]. For boundary value problems, such as the one described in this paper, it is also necessary to specify a source term. It is assumed that only a TE_{10} mode exists in the waveguide, which makes it necessary to model a sufficient length of waveguide, as shown in Figure 2.3, to ensure that disturbances caused by the aperture are not present at the point where the excitation is applied. For frequency domain problems it is simply necessary to specify the tangential components of the field at the terminating plane in the waveguide [Webb, 1981]. This can be carried out since the distribution of the transverse field across the waveguide is known;

$$\begin{aligned} E_y &= E_0 \sin\left(\frac{\pi x}{a}\right), \\ E_x &= 0, \end{aligned} \tag{2.46}$$

where a is the width of the waveguide. E_0 is normally chosen to be 1 and the fields can then be rescaled after the normalised distribution has been found (see §4.3).

The amplitude of the field at the terminating plane is the vectorial sum of both forward and reflected waves. In the time domain the amplitude of the reflected wave will vary as the system moves from a transient to a steady state condition. Consequently the amplitude of the field at the terminating plane cannot be determined in advance. It is therefore not possible to prescribe an inhomogeneous Dirichlet boundary on this plane in the time domain. To overcome this problem the waveguide is excited by a current sheet some distance from the terminating plane and the mesh terminated by an absorbing boundary, Figure 2.3. This technique has previously been used with the time domain finite difference method [Iskander, 1993]. In practice this approach has a good

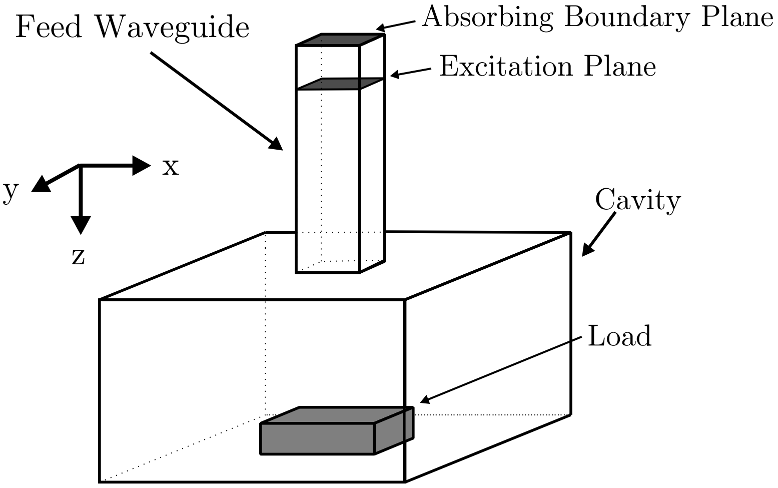

Figure 2.3: Multimode cavity with waveguide feed and absorbing boundary plane for time domain calculation.

physical basis when the applicator is supplied via an iso-circulator which has the effect of absorbing the majority of reflected energy.

2.5.1 Absorbing boundary conditions (ABCs)

Having determined that an ABC is required to terminate the waveguide feed in the time domain its implementation needs to be considered. Development of high quality ABCs has seen intensive effort for open problems, such as finding the scattering cross section of objects. Engquist & Majda [1977] proposed a method for generating good approximations to an ABC. This was extended by Mur [1981] explicitly for use with the finite difference method. Mur's ABC has become a standard for finite difference calculations, however, other methods which appear greatly superior to Mur have been suggested such as Liao's ABC [Liao *et al.*, 1984; Chew, 1990] and the Berenger ABC [Katz *et al.*, 1994]. These methods, while offering extremely good approximations to a perfect absorber are designed for open problems and are of a complexity that is unnecessary for this application. Second order Engquist-Majda and Mur ABCs lead to unsymmetric matrices while Liao's method requires the field at several time steps to be stored for points near to the boundary plane. For a simple waveguide we have a

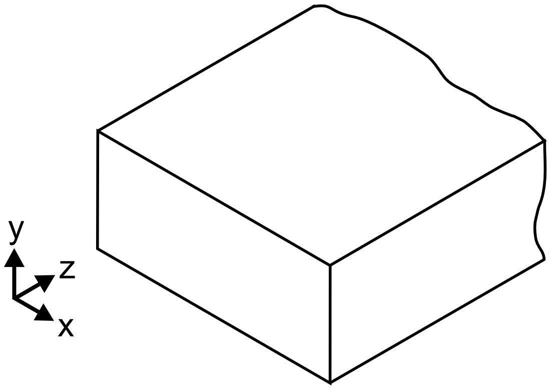

Figure 2.4: Rectangular waveguide.

considerable advantage: the field distribution is known *a priori*. This enables a simple but effective ABC to be derived that can be implemented with very little effort and that does not increase the computational effort during the time stepping. The ABC employed here simply involves terminating the waveguide with its characteristic impedance, which can be done by evaluation of the surface integral term of equation (2.22) [Dibben & Metaxas, 1994b]

In a rectangular waveguide, as shown in Figure 2.4, the transverse components of the field for the TE modes are related by [Collin, 1992]:

$$\begin{aligned} E_x &= Z(\omega)H_y, \\ E_y &= -Z(\omega)H_x, \end{aligned} \tag{2.47}$$

where $Z(\omega)$ is the characteristic impedance of the waveguide for a given mode. For the TE$_{10}$ mode

$$Z(\omega) = Z_0\frac{\lambda_g}{\lambda_0}, \tag{2.48}$$

where λ_g and λ_0 are the waveguide and free space wavelengths respectively and Z_0 is the impedance of free space. Equation (2.47) enables us to evaluate the surface integral of equation (2.22) over the terminating plane of the waveguide, where the cross product may be written as,

$$\mathbf{n} \times \frac{\partial \mathbf{H}}{\partial t} = -\frac{\partial H_x}{\partial t}\,\widehat{\mathbf{j}}$$

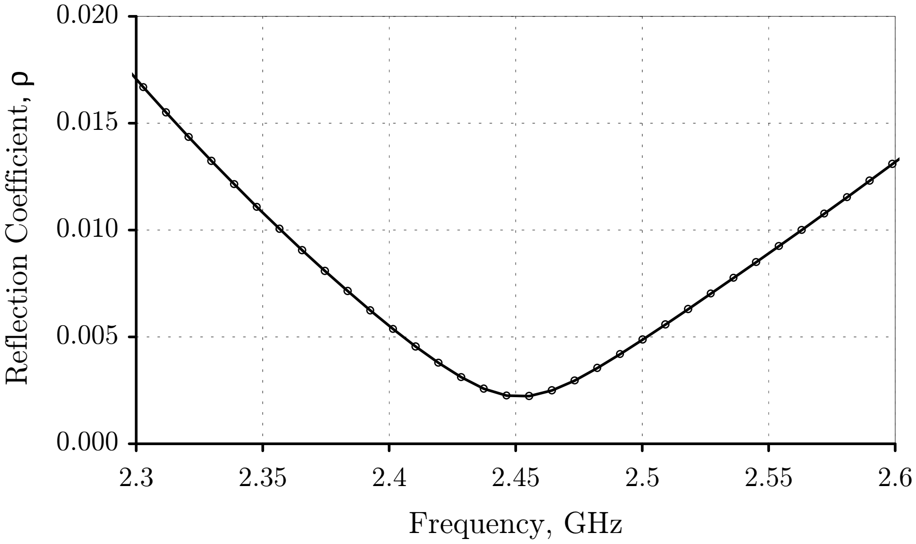

Figure 2.5: Magnitude of the reflection coefficient, ρ, for a waveguide terminated by the simple ABC, $Z(\omega)$ chosen at $\omega = 2.45$ GHz.

$$= \frac{1}{Z(\omega)} \frac{\partial E_y}{\partial t}\, \widehat{\mathbf{j}}, \tag{2.49}$$

since for the TE_{10} mode, $H_y = E_x = 0$. The surface integral term therefore becomes

$$\mu_0 \int_\Gamma \psi \cdot \left(\mathbf{n} \times \frac{\partial \mathbf{H}}{\partial t} \right) d\Gamma \qquad \rightarrow \qquad \frac{\mu_0}{Z(\omega)} \int_\Gamma \psi \cdot \frac{\partial \mathbf{E}_y}{\partial t} d\Gamma. \tag{2.50}$$

This integral can now be discretised in the same fashion as before, using equations (2.23). Only $\partial \mathbf{E}_y / \partial t$ is involved here, so the terms can be added directly into the matrix $[\mathbf{T}_\sigma]$ during the matrix assembly process. The connectivity remains unchanged so the sparsity of the matrix is not reduced and the matrix remains symmetric. This ABC can be seen as equivalent to adding a layer of lossy material at the terminating plane.

$Z(\omega)$ is frequency dependent, therefore this boundary will only be strictly valid at a single frequency, for which $Z(\omega)$ is specified. However, in practice we are interested in a narrow spectrum of frequencies and this method appears to provide a satisfactory approximation to an absorbing boundary when a mean value of $Z(\omega)$ is chosen. Figure

2.5 shows the magnitude of the reflection coefficient (see §4.2) for a length of waveguide with a cross section of 100 mm × 50 mm and terminated by an ABC of this type. Minimum reflection is produced at 2.45 GHz the frequency for which $Z(\omega)$ was specified. While this ABC is seen to be far from perfect it provides a satisfactory approximation for the type of problems considered here.

2.6 Post-Processing of Edge Element Results

The degrees of freedom associated with Whitney elements correspond to the circulations of the field along an edge, however, vector field values at points throughout the domain are often required. It is therefore desirable to convert the edge values into vector field values which are more convenient for graphical display. When a temperature calculation is performed, following the electromagnetic field calculation, it is necessary to know power density values. These can be obtained directly from the electric field values at each node of the finite element mesh used for the calculation. Since the mesh used for the temperature calculation may not be the same as that used for to determine the field it must also be possible to determine the electric field at any arbitrary point within the domain.

Determination of the field values is not as straightforward as it might first appear. Some of the large errors reported using Whitney elements [Bandelier & Rioux-Damidau, 1990] have originated not in the underlying field solution but in inadequate attention to the post-processing of the data. Whitney elements have a constant value of the tangential field along their edges while giving rise to linear variation within the element. This means that each element connected to a node P, as shown in Figure 2.6, will give a slightly different value of the field at that node. It is clear that if the Whitney basis functions are used to interpolate the field at any arbitrary point within the mesh then a point close to the border between two elements could have significantly different values depending upon which side of the border it lies. This is obviously unsatisfactory since, with the exception of dielectric interfaces, the field solution should be smooth. The linear edge elements do not suffer from these problems since they provide linear interpolation along the edges of the element.

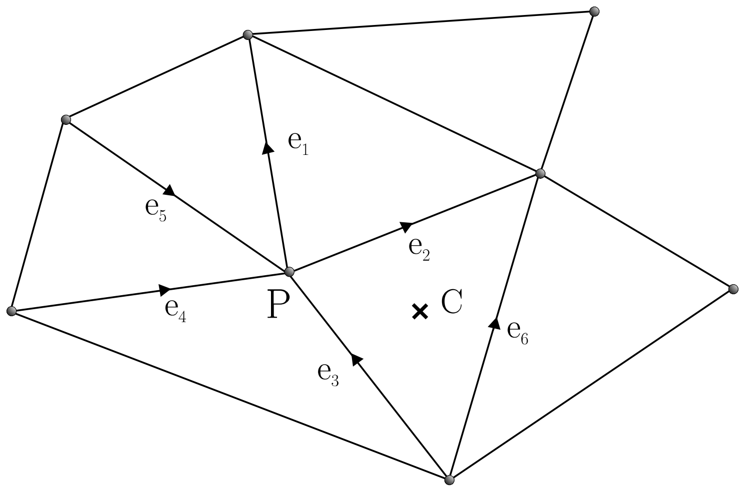

Figure 2.6: A portion of a triangular mesh.

To overcome the difficulty of jumps in the solution at edge boundaries there are a number of options available; one could simply calculate field values at the centroids of the elements. This, however, would not allow calculation at an arbitrary point unless a method of interpolating between centroids was available. A better approach is to average the contributions to the field at each node. These nodal values can then be interpolated throughout the mesh using the simple nodal based expansion functions as used for nodal elements. This method poses two questions: how is the averaging to be carried out and what happens at dielectric interfaces.

In order to average the field values at the nodes of the mesh we can borrow some of the ideas used for the differentiation of field values [Silvester & Omeragić, 1993]. The summation,

$$\mathbf{E}_P = \frac{\sum_i^n \xi_i \mathbf{E}_P^i}{\sum_i^n \xi_i}, \tag{2.51}$$

is performed for all elements, i, connected to node P where $\mathbf{E}_P^i$ is the value of the field at node P due to element i. It remains to chose the form of the weighting functions ξ. The basic choices are;

- Simple average: Values from each element connected to a node have an equal weighting, *i.e.* $\xi_i = 1$.

- Volume weighted average: Contributions from an element at a node are weighted by the volume of that element.
- Distance to the centroid: contributions from an element are weighted by the distance from the node to the centroid of the element

At dielectric interfaces the normal component of the electric field is discontinuous. The simple averaging techniques outlined above should therefore be applied with care. It would be possible to average the value while taking into account the continuity equation for the normal field at the boundary, in a similar manner to that proposed by Paulsen for nodal elements (see §2.2.1). This requires the definition of a normal at all interface nodes. A simpler alternative is to simply perform the averaging described above for elements of each material separately. Different values of the field will then be obtained in each material.

2.6.1 Error calculation

In order to assess the error from a given discretisation it is necessary to define some measure of this error. The one that is used here is the ℓ_2-norm, which for a vector space $\mathbf{y}$ is defined by,

$$\| \mathbf{y} \|_2 = \sqrt{\int_\Omega \mathbf{y}^2 \, \mathrm{d}\Omega} \tag{2.52}$$

The error is then given by,

$$\frac{\| \mathbf{E} - \mathbf{E}^h \|_2}{\| \mathbf{E} \|_2} \tag{2.53}$$

where $\mathbf{E}$ is the true solution and $\mathbf{E}^h$ is the solution obtained from the finite element method. This gives the error over the whole problem domain. In order to apply (2.53) it is necessary to know the correct solution for a problem. Consequently a short circuit waveguide has been modelled where the analytical solution is known. The integral (2.52) is evaluated in each element using quadrature integration, evaluating the field at 4 points within the tetrahedron, and 8 points in a hexahedron [Hammer, Marlowe, & Stroud, 1956; Ciarlet, 1978].

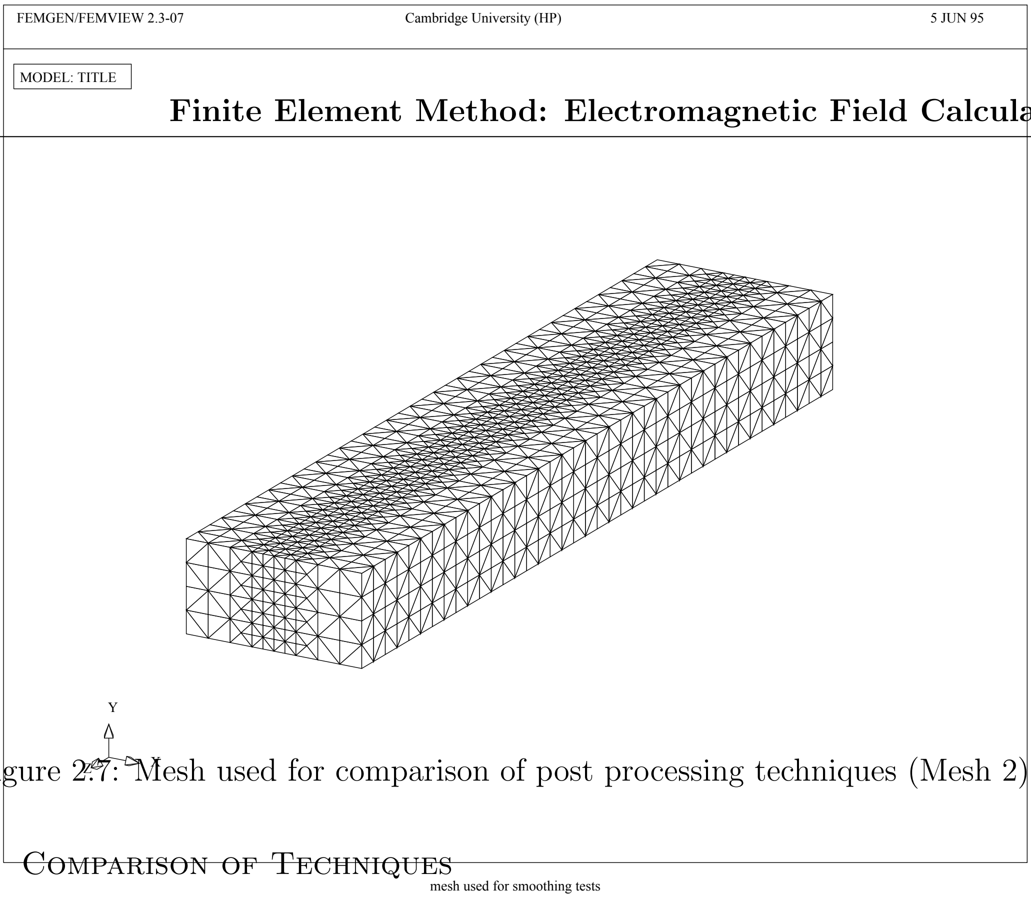

Figure 2.7: Mesh used for comparison of post processing techniques (Mesh 2).

2.6.2 COMPARISON OF TECHNIQUES

To examine the effect of using the different techniques described above they were applied to the problem of a short circuit waveguide, which had a cross section of 86 × 43 mm and was 400 mm in length. Table 2.1 shows the errors obtained for two different meshes. Mesh 1 was constructed by dividing the waveguide into a structured mesh of 8 × 4 × 40 hexahedra and the dividing each hexahedra into 5 tetrahedra, which produced a mesh containing 9,268 edges. The second mesh, shown in Figure 2.7, was constructed by taking mesh 1 and refining the elements in the central region. This gave elements of different shapes and sizes in the central region and produced a mesh with 33,338 edges.

Post-processing	Mesh 1	Mesh 2
None	0.1357	0.1143
Simple Average	0.0545	0.0384
Volume Weighted	0.0571	0.0468
Centroidal Distance	0.0550	0.0401

Table 2.1: Comparison of the errors obtained with different post processing techniques.

The figures in Table 2.1 show that the post processing significantly reduces the error when measured in the ℓ_2-norm. When a mesh containing elements of roughly equal size (mesh 1) is used there appears to be little to choose between the methods. When the sizes of the elements vary, the difference between the techniques is greater with the simple averaging method giving the lowest error. Consequently this method was the one adopted for this work.

2.7 Comparison of Element Types

Having outlined the finite element formulation that will be used for the field calculation there still remain a number of topics that need to be addressed before the method can be applied with confidence to problems of electromagnetic heating. It is necessary to gain some estimate for the possible errors that may be encountered when using a given element size to model the process. How fine does the mesh need to become before a suitable accuracy is obtained? This section compares both the element types and the different shapes, tetrahedra, hexahedra and prisms for accuracy. There are several different element types available for the computation of the electric field via the finite element method. These are,

- Whitney edge elements.
- Linear edge elements.
- Nodal elements.

So far it has been assumed that the first type, Whitney elements, would be used for the discretisation as they have many advantages over the other types.

2.7.1 COMPARISON OF WHITNEY ELEMENTS AND LINEAR EDGE ELEMENTS

There is still some debate about the relative merits of linear edge elements compared to Whitney elements. The lack of first order completeness for Whitney elements has produced doubts about their use. Most specifically in their convergence rate on mesh refinement. Mur [1994] states that linear edge elements are to be preferred since they posses a local approximation error of $O(h^2)$ compared to $O(h)$ for Whitney elements where h is some measure of element size. This gives them better convergence properties on mesh refinement. Bossavit [1994] on the other hand states that the asymptotic rate of convergence of the two elements are the same. The problem here lies in the definition and method of calculating the error. Whitney elements have basis functions that are constant along an edge so calculation of the field at a point just inside an element from the basis functions of that element will produce a large error compared to that produced by linear elements. This, however, is the wrong way of interpreting the field (see §2.6). Conversion of the space spanned by the Whitney forms to a vector field representation convenient for graphical display must be carried out with care.

In order to asses the relative errors of the two elements an empty waveguide (WG9A) was modelled. The waveguide had a cross section of 86 × 43 mm and a length of 400 mm. The problem was solved in the frequency domain at a frequency of 2.45 GHz. For this particular problem the analytical solution is known [Metaxas & Meredith, 1983]. Several different meshes were used producing successive orders of refinement. The meshes were based on regular hexahedra which were then broken into five tetrahedra. The error between the calculated solution and the true analytical solution is presented in Figures 2.8 to 2.10. Two results are presented for Whitney elements, the first shows the error calculated by performing the integration of equation (2.52) from the edge values of each element directly, the second smoothed solution is where the error has been calculated from the post-processed solution. The simple method using equal weighting for each element was used for post-processing (see §2.6).

These graphs explain some of the unfavorable reviews received by edge elements. When the ℓ_2-norm error is calculated directly form the edge values then a lower rate of convergence is obtained with the Whitney elements. This is the cause of many of the high errors reported using Whitney elements. However, when the post processing is carried out then the rates of convergence of the two elements become very similar and Whitney elements give a *consistently lower error* than the linear elements. This clearly demonstrates the importance of post-processing. Linear elements produce an error which is identical before and after post-processing due to the linear nature of the basis function along an edge.

The time taken for a given solution is dependent upon the number of non-zeros in the

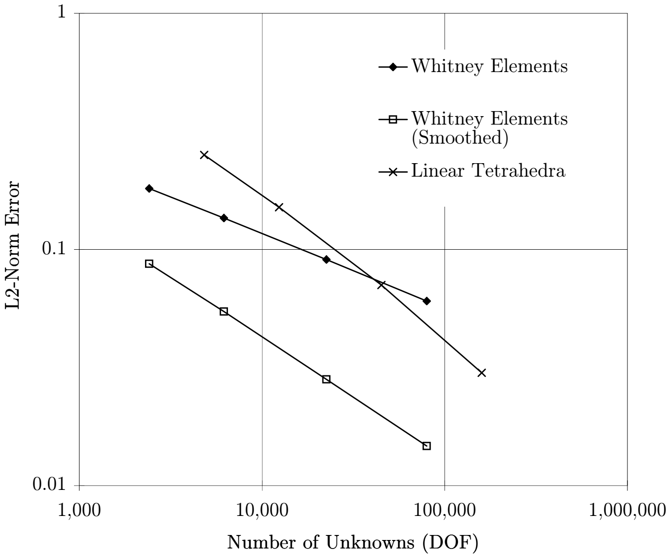

Figure 2.8: ℓ_2-norm error vs Degrees of Freedom for Whitney elements and linear elements.

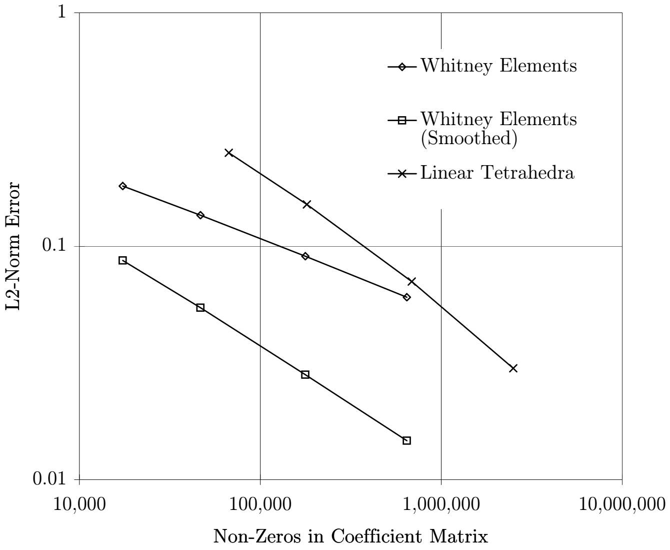

Figure 2.9: ℓ_2-norm error vs matrix size for Whitney elements and linear elements.

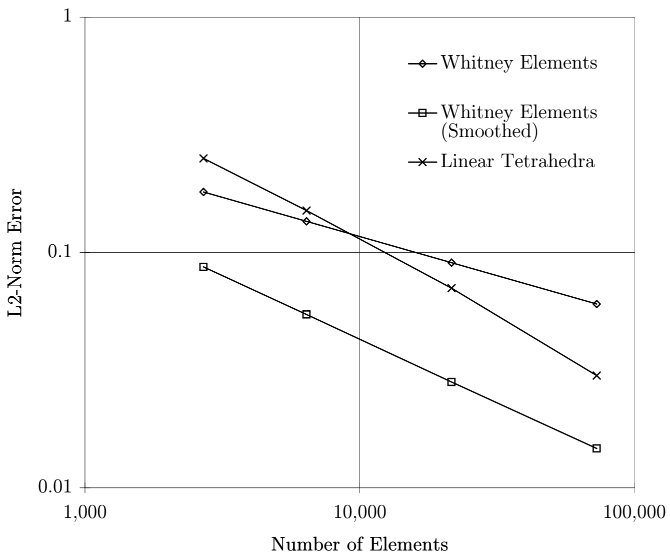

Figure 2.10: ℓ_2-norm error vs number of elements for Whitney elements and linear elements.

assembled matrix rather than the number of unknowns. This is because the heart of the iterative solution method is a matrix–vector multiplication. From Figure 2.9 it is clear that for a given error the Whitney elements produce a significantly smaller coefficient matrix than the linear elements providing much greater efficiency.

It was noted that in this particular problem the electric field is aligned with many of the edges since the mesh used was derived from regular hexahedra. In order to test the effect of a more irregular tetrahedral mesh a series of meshes were constructed using the GEOMPACK software [Joe, 1993]. This produces tetrahedra directly, as shown in Figure 2.11. The error produced by the irregular mesh is slightly larger than that of the regular mesh, depicted by Figure 2.12, however, the convergence properties remain the same.

2.7.2 COMPARISON OF WHITNEY ELEMENTS AND NODAL ELEMENTS

A further comparison that can be made is between edge elements and nodal based elements. Nodal elements have many problems, not least spurious modes and problems at

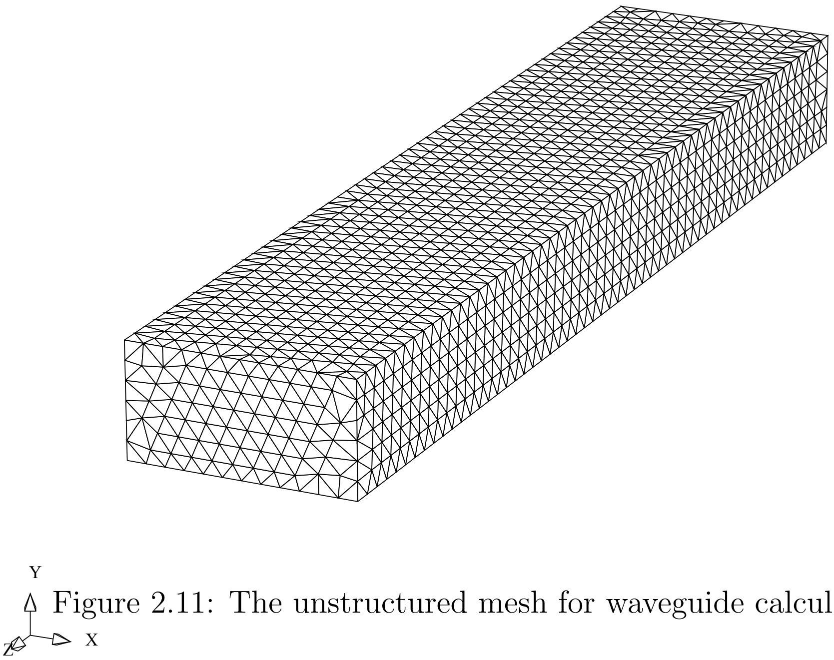

Figure 2.11: The unstructured mesh for waveguide calculation.

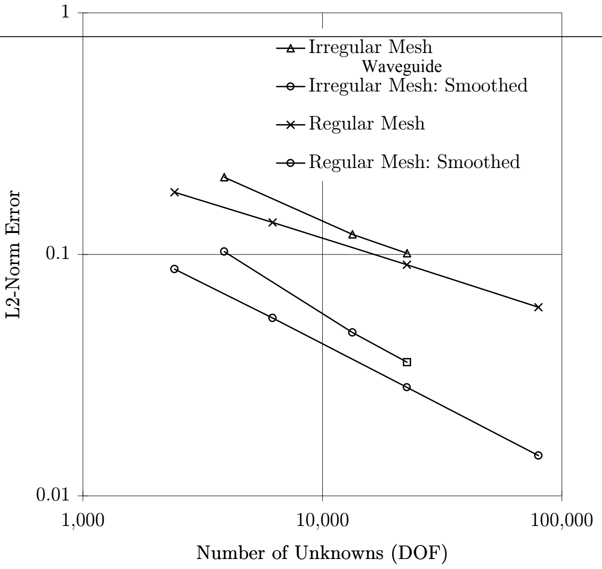

Figure 2.12: Comparison of Errors for different tetrahedral meshes for the waveguide problem.

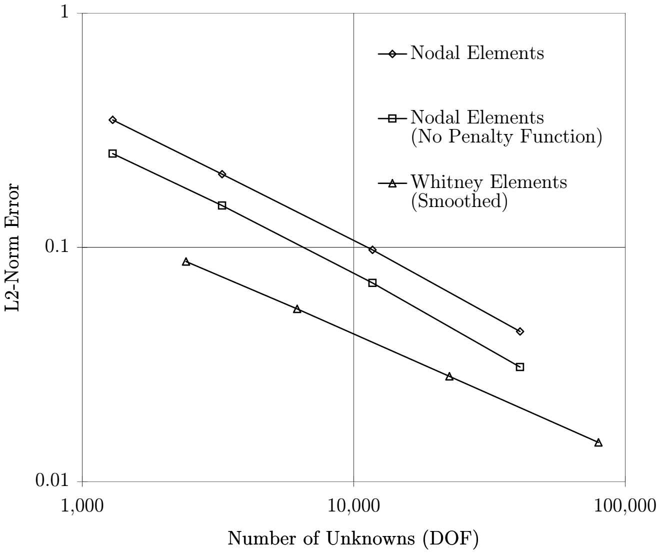

Figure 2.13: Comparison of errors for nodal elements and Whitney elements vs degrees of freedom.

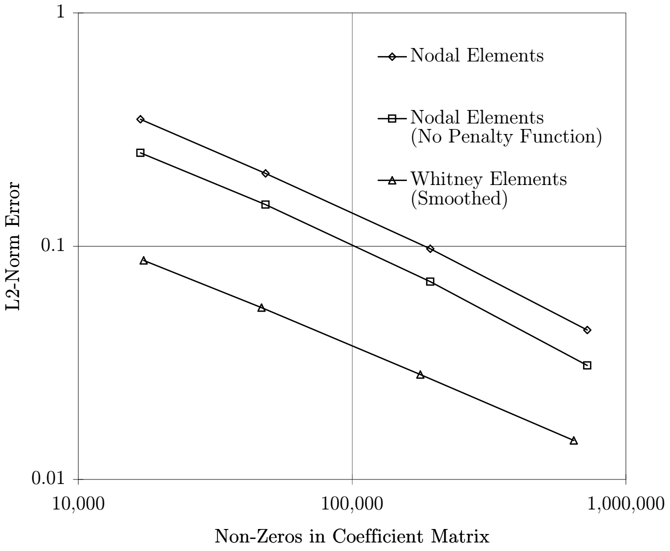

Figure 2.14: Comparison of errors for nodal elements and Whitney elements vs non-zeros entries in the coefficient matrix.

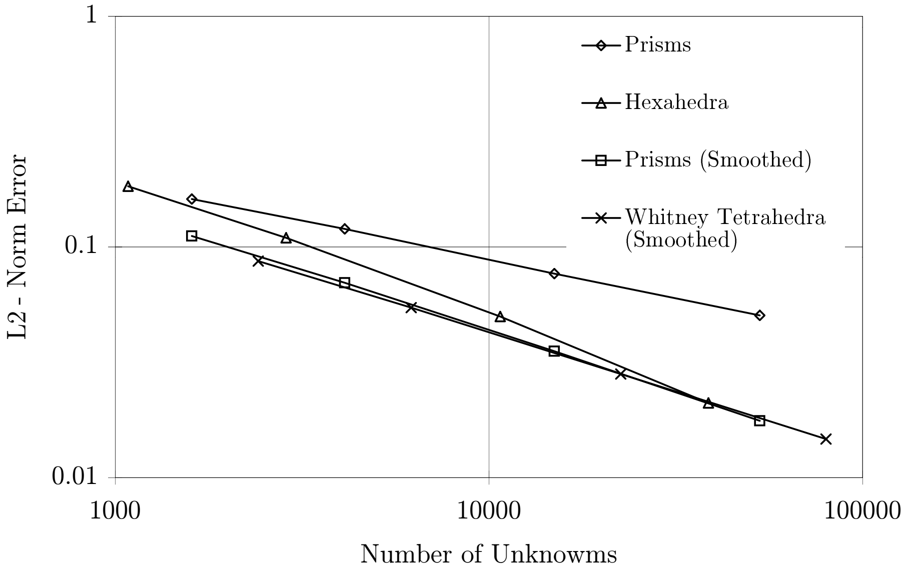

Figure 2.15: Comparison of errors for tetrahedral Whitney elements and hexahedral edge elements vs number of unknowns.

dielectric interfaces, they are, however, favoured by many workers [Mur, 1988; Paulsen & Lynch, 1991]. Since nodal elements are first order complete, they have a local approximation error of $O(h^2)$. However, these produce coefficient matrices with far fewer entries than the linear edge elements. Mur [1988] has therefore concluded that nodal elements are the most efficient choice in homogeneous regions. The use of a penalty function to explicitly enforce the divergence is thought sufficient to eliminate any spurious modes. Results for the waveguide problem are given in Figure 2.13 and 2.14. The very simple geometry means that spurious modes are not present in this particular problem even when the penalty function is not used. It is clear from the graphs that Whitney elements are superior to nodal elements, the good convergence after post processing being comparable to that of nodal elements. Furthermore, we see that the addition of the penalty function has a detrimental effect on the accuracy of the solution.

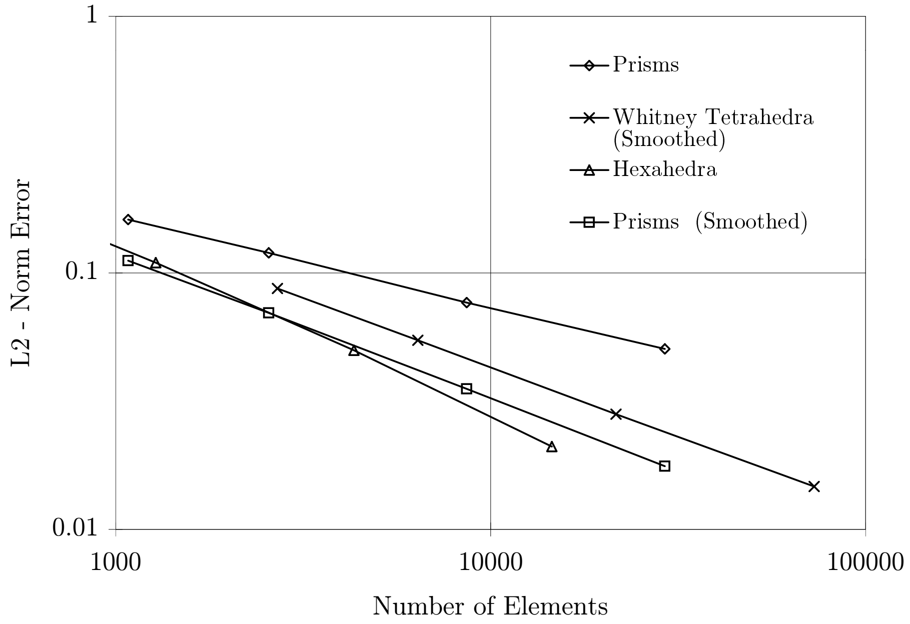

Figure 2.16: Comparison of errors for tetrahedral Whitney elements and hexahedral edge elements vs number of elements.

2.7.3 COMPARISON OF EDGE ELEMENT SHAPES

It was stated earlier that it is often desirable to use element shapes other than tetrahedra. This may be due to limitations in the available mesh generation software. It is therefore important to assess the relative merits of the different element types. Starting with the same structured hexahedral mesh that was used above, the waveguide was modelled using hexahedral edge elements and prismatic edge elements. The prismatic elements were formed by splitting each hexahedron into two, with the triangular faces lying on the x-z plane. The relative errors produced are shown in Figures 2.15 and 2.16. The rate of convergence appears to be marginally faster for hexahedral elements than for tetrahedral elements. For a particular mesh the number of unknowns is much lower for hexahedral elements, however, for a given number of unknowns hexahedral elements will produce a denser coefficient matrix. So for a given error hexahedral elements need a similar number of unknowns to Whitney tetrahedra but the coefficient matrix will have twice as many non-zero entries. Thus they are not as efficient as Whitney elements but superior to linear edge elements. Prismatic elements appear to give a very similar convergence to Whitney tetrahedral elements. The raw edge values giving a slower rate of convergence than the post-processed values.

2.8 Conclusions

This chapter has introduced the time domain finite element method that will be used for many of the problems considered in this thesis. The time domain method requires the solution of a linear system at each time step, which contrasts to the single solution required for the frequency domain method. For the time domain finite element method to be competitive with the more traditional frequency domain approach it is necessary for the solution of this system to be considerably easier in the time domain compared to the frequency domain. The solution of this system of linear equations is the subject of the next chapter.

It was clear from the results presented for the short circuit waveguide that Whitney elements, when coupled a with post-processing technique, are the superior choice for the discretisation. The method of post processing using simple averaging at the element's nodes was seen to be the most effective of the three methods discussed here. This allowed Whitney elements to produce consistently lower errors than the other element types and to show a similar rate of convergence on mesh refinement.

Chapter

3

Solution of Linear Equations

3.1 Introduction

The most computationally intensive part of obtaining a finite element approximation is the solution of the set of linear simultaneous equations produced by the discretisation. In the frequency domain only a single solution is required at each frequency of interest, whereas in the time domain the system has to be solved at each time step. However, it will be seen that the system to be solved in the time domain is considerably easier than the corresponding frequency domain one. When modelling a multimode applicator in three dimensions there are often more than 100,000 unknowns, which will be complex for the frequency domain problem when lossy material is present. The matrices are, however, very sparse with a non-zero structure which reflects the complexity of the region being modelled and the irregular nature of the mesh used. The solution method should be able to take full advantage of this sparsity to optimize both the number of arithmetic operations and the amount of computer memory that is required. The matrices arising from the frequency domain method are often indefinite [Webb, 1981] which makes solution more difficult. It is also found that systems arising from multimode cavities containing a dielectric with a large value of permittivity generally have a high condition number. This has the effect of slowing the convergence of iterative methods and increasing the possibility of numerical errors in the solution. The problems of ill-conditioning are discussed in §3.4.

Methods for the solution of the linear system,

$$\mathbf{A}\mathbf{x} = \mathbf{b} \tag{3.1}$$

where $\mathbf{A}$ is large and sparse can be divided into two categories; direct and iterative. The former perform a fixed number of steps to generate the solution, the accuracy of which is limited by the accumulation of round off errors caused by the finite precision of the arithmetic. Iterative methods generate successive refinements to an initial guess until the required accuracy is reached. The purpose of this chapter is to describe some of the methods that can be used for the solution of (3.1) and to compare their performance. Initially the methods that are suitable for the finite element problem are discussed then various preconditioning techniques that can be used to accelerate the convergence of the iterative techniques are outlined. Finally the performance of these methods for both frequency domain and time domain problems are compared.

3.2 Direct Methods

The most common direct method for solving the system (3.1) is Gaussian elimination, of which there are several variants [Duff *et al.*, 1986]. The matrix is factored into two triangular matrices such that

$$\mathbf{A} = \mathbf{L}\mathbf{U}, \tag{3.2}$$

where $\mathbf{L}$ is a lower triangular matrix and $\mathbf{U}$ is an upper triangular matrix. For symmetric matrices $\mathbf{U} = \mathbf{L}^T$ and the process is usually referred to as Cholesky factorization. After factorization the solution can easily be obtained by substitution. The methods are implemented so that they can take advantage of the sparsity of the matrix.

During the factorization process entries in the matrix which are initially zero become non-zero, *i.e.* they are “filled in”. The resulting reduction in the sparsity of the matrix increases the amount of storage[1] required to hold the matrix. This increase can be very significant. However, there are several algorithms available for reducing the fill in by

---

[1] Storage in double precision, so one complex value requires $2 \times 8 = 16$ bytes of memory. Only half of the matrix is stored since it is symmetric.

	Original		Factored	
Unknowns, n	Non Zeros, τ_c	Size Mbytes	Non Zeros, τ_f	Size Mbytes
2,415	34,686	0.3	173,050	1.3
6,196	93,432	0.8	749,546	5.8
22,542	354,996	2.0	5,969,700	45.7
79,821	1,291,266	10.5	41,023,244	313.0

Table 3.1: Number of non-zeros and storage requirement for the coefficient and factored matrices for some three dimensional waveguide problems.

reordering the variables [George & Liu, 1981]. One of the most effective methods for finite element computations is the minimum degree algorithm. Table 3.1 compares the number of non-zero entries in the original matrix , τ_c, and the factored matrix, τ_f, for several three-dimensional short circuit waveguide problems when reordering using the minimum degree algorithm has been employed. These results are shown graphically in Figure 3.1. The size of the coefficient matrix increases as $O(n)$ whereas the factored matrix increases as $\sim O(n^{1.6})$ in this case. The tetrahedral meshes used were based on a structured hexahedral mesh, when an irregular unstructured mesh is used the connectivity will be different and may give rise to a different dependence on n. Without reordering the number of non-zero entries in the factored matrix would be considerably higher, with the exact number being dependent on the actual ordering. If the matrices were to be held as dense matrices then the storage would grow as $O(n^2)$, with the largest problem of Table 3.1 requiring a massive 95 G bytes of memory.

Even when the minimum degree algorithm is used the increase in storage requirement is very large. For realistic three-dimensional cavity problems this increase in storage is beyond the resources available in the majority of workstation computers. This makes “in core” Cholesky factorization unsuitable for solving this type of problem. To overcome this large storage demand Irons [1970] proposed a frontal method which combines the matrix assembly and factorization phases. The idea being to eliminate a variable as soon as possible and to write the associated equation to a secondary storage device. In this way only a small portion of the matrix, the wave front, need be kept in mem-

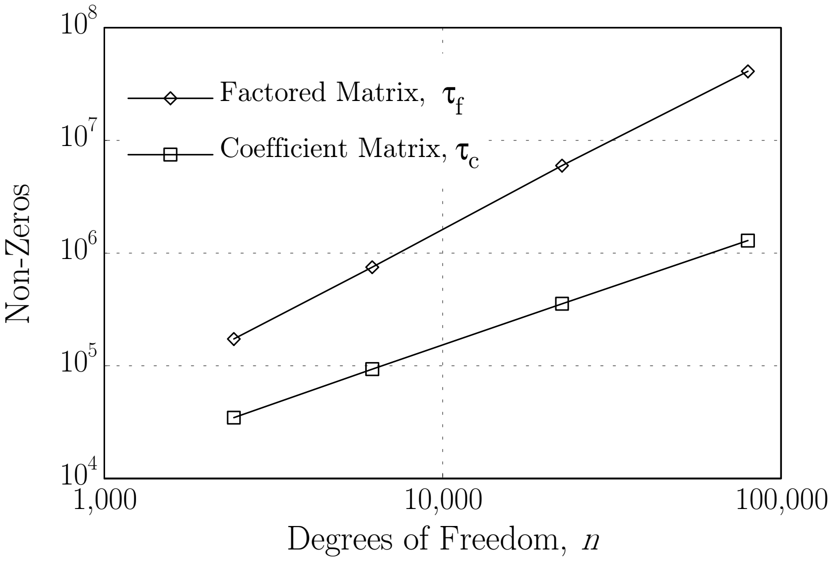

Figure 3.1: Number of non-zero entries in the coefficient and factored matrices from the short circuit waveguide problem.

ory. Secondary storage is considerably slower than main memory so using this method immediately increases the solution time.

Direct methods generally scale poorly with increasing numbers of unknowns, with the number of arithmetic operations required for factorization being $O(n.\tau_f)$. Since τ_f depends upon both the mesh connectivity and the renumbering algorithm used precise operations counts are not available for the general case. However, as shown in Table 3.1 the number of non-zeros in the factored matrix and therefore operations increases rapidly with the number of unknowns.

When the matrices are indefinite the Cholesky decomposition can fail unless precautions are taken. Pivoting is nearly always used when dealing with dense matrices to prevent both breakdown and to minimise round off errors caused by small pivot elements. The re-arrangement of the rows and columns during pivoting, however, destroys the symmetry of the matrix. This will have the adverse effect of doubling both the storage requirement and the computational cost of the factorization and following substitutions as it is now necessary to work with both the upper and lower triangular matrices. Without pivoting, however, the method may fail to give accurate solutions or indeed any solution at all. A block pivoting method has been proposed that preserves symmetry and allows a stable factorization, see for example Duff, Erisman, & Reid [1986]. This would allow the direct methods to be used for general problems without doubling the storage, however, the use of this method has not been investigated.

In the time domain a solution of equation (3.1) is required at each time step. The main cost of a Cholesky factorization is associated with the the factorize phase, the solution at each time step can then be carried out in $O(\tau_f)$ operations. For small problems the Cholesky decomposition is well suited to the time domain problem, however, storage requirements preclude its use for larger problems. It will also be seen that iterative methods are particularly well suited to the time domain problem. For large problems $\tau_f \gg \tau_c$ so if the number of iterations, k, of an iterative method required for solution satisfies $k\tau_c < \tau_f$ then the iterative method will be faster at each iteration. Of course the Cholesky method also has a large cost associated with the factorization.

Direct methods are only suitable for small problems such as waveguides where the number of elements and hence the number of unknowns, can be kept small. For larger problems such as three dimensional cavities the memory requirements are too great for them to be useable. This is true for both the time domain and frequency domain problems. However, incomplete factorizations can be used as preconditioners to the iterative methods described below.

3.3 Iterative Techniques

3.3.1 INTRODUCTION

The development of iterative techniques for the solution of linear systems arising from discretized partial differential equations is a vigorous branch of numerical analysis. Iterative methods produce a sequence of approximations to the solution of equation (3.1), which is terminated when the error has been reduced to a satisfactory level. The methods often operate directly on the coefficient matrix **A** via a matrix-vector multiplication. When the matrix is large and sparse the cost of such a multiplication is $O(n)$ compared to $O(n.\tau_f)$ for the sparse Gaussian elimination. So as long as the number of iterations is not too large the iterative solver can be considerably faster than direct methods. Furthermore, the matrix-vector product is easily vectorized allowing easy implementation on fast parallel architectures, the development of which has given further impetus to the drive towards better iterative solution techniques [Saad, 1989]. Since the coefficient matrix is used directly the storage requirement is considerably smaller than for the direct methods. Assuming that, as the mesh is refined each edge remains on average connected to an equal number of elements then the number of non-zero entries in each row will remain constant. The storage requirement will therefore grow as $O(n)$ which is a considerable improvement over the direct methods. The lower storage overhead is often the overriding reason for the use of iterative methods in finite element solutions.

Many different iterative techniques exist, each being suited to a particular class of problem. When the matrix $\mathbf{A}$ arises from the frequency domain discretisation it is complex and indefinite. Consequentially many of the classical iterative methods such as Gauss-Seidel or Successive Over Relaxation (SOR) [Barret *et al.*, 1993] do not converge and are therefore unsuitable. They are suitable, however, for use for the time domain discretisation. The performance of several methods will be compared in section 3.6.

The iterative method that is currently favoured by the finite element community and which is receiving wide attention is the conjugate gradient (CG) method and the related family of Krylov subspace methods. The CG method was developed independently by Hestenes and Stiefel and presented in a joint paper [Hestenes & Stiefel, 1952]. Initially it was considered a direct method, requiring n steps before terminating[2] with the exact solution. Reid [1970] noted that in many cases a satisfactory approximation to the solution was obtained in far fewer than n steps so the CG method should be viewed as a true iterative method which was particularly applicable to large sparse systems. The CG method is only suitable for real positive definite systems and is therefore unsuitable for the present frequency domain problem, however, subsequent extensions have produced related algorithms that are applicable to a wide range of unsymmetric and indefinite complex systems.

In order to extend the CG method to unsymmetric indefinite systems Fletcher [1976] proposed the use of the bi-conjugate gradient (Bi-CG) method which was originally de-

---

[2] The finite termination property of the CG method holds only in exact arithmetic.

veloped by Lanczos [1950]. This method no longer satisfies the minimization property of the conjugate gradient algorithm [Barret *et al.*, 1993]. Indeed it has been shown that the minimization property of the CG method cannot be ensured for non-Hermetian matrices when short recurrences are used [Faber & Manteuffel, 1984]. The generalized minimum residual (GMRES) algorithm [Barret *et al.*, 1993] which satisfies the minimization property for general matrices does so at the expense of storing all residual vectors, so that the storage requirement and operations count grows linearly at each iteration. In practice this makes it necessary to periodically restart the algorithm once storage has been exhausted, which can result in slow convergence [Freund & Nachtigal, 1991].

The Bi-CG method suffers from extremely erratic convergence and can suffer break down under certain circumstances. The erratic convergence is problematic because it makes the determination of convergence difficult since it is possible for a low value of the residual to be obtained while the error remains high. Several techniques have been proposed to deal with this; a stabilized version of the Bi-CG algorithm, (Bi-CGSTAB), was developed by van der Vorst [1992] which has smooth convergence and Weiss [1994] uses a smoothing method to ensure a monotonic decrease in the norm of the residual. The problem of breakdown, caused by a division by zero is more serious and has led to the development of alternative algorithms. Paige & Saunders [1975] give details of such an alternative method for solving symmetric indefinite systems and more recently Freund & Nachtigal [1991] describe a Quasi-Minimum Residual (QMR) algorithm that is suitable for unsymmetric indefinite systems and which does not suffer from breakdown and has smooth convergence.

3.3.2 COMPLEX SYSTEMS

When the matrix coefficients are complex the standard CG algorithm cannot be used even when the matrix is complex symmetric [Jacobs, 1981]. There are several approaches that can be taken in order to solve equation (3.1). Firstly, it would be possible to solve the real system

$$\begin{bmatrix} \Re e(\mathbf{A}) & -\Im m(\mathbf{A}) \\ \Im m(\mathbf{A}) & \Re e(\mathbf{A}) \end{bmatrix} \begin{bmatrix} \Re e(\mathbf{x}) \\ \Im m(\mathbf{x}) \end{bmatrix} = \begin{bmatrix} \Re e(\mathbf{b}) \\ \Im m(\mathbf{b}) \end{bmatrix} \tag{3.3}$$

using one of the methods suitable for unsymmetric systems such as GMRES, CGS or Bi-CG. This approach has been considered unsatisfactory due to slow convergence [Jacobs, 1981; Freund, 1992]. An alternative is to form the normal equations,

$$\mathbf{A}^H\mathbf{A}\mathbf{x} = \mathbf{A}^H\mathbf{y} \tag{3.4}$$

where the subscript H denotes the conjugate transpose of the matrix. The matrix $(\mathbf{A}^H\mathbf{A})$ is now real and symmetric positive definite and so suitable for solution by the CG method. The rate of convergence of the CG method is proportional to the square root of the condition number [Axelsson, 1980] and since forming the normal equations has the effect of squaring the condition number it is clear that this method will have an adverse effect on the convergence which may already be slow for ill-conditioned systems.

In view of the above remarks it is preferable to use a method developed specifically for complex systems. Jacobs [1981] presents a complex bi-conjugate gradient algorithm, which is an extension of the work by Fletcher [1976] to complex systems. When the matrix to be solved is symmetric, the Bi-CG algorithm can be reduced so that only a single matrix vector product is required during each iteration. In fact the steps that are performed are the same as those for the CG algorithm, however, the algorithms are different since the minimization property no longer holds for the Bi-CG method which satisfies Galerkin's condition instead [Freund, 1992]. A better approach than the Bi-CG method is to use the QMR algorithm developed by Freund [1992] specifically for complex symmetric matrices. This method has smooth convergence and does not suffer from the breakdown associated with the Bi-CG method. Furthermore it does not require the use of the normal equations so there is no squaring of the condition number.

3.3.3 PRECONDITIONING

Iterative methods often converge fairly slowly so it is desirable to find some method of speeding them up. Preconditioning the matrix is one method that has been extremely successful at this in many applications. Instead of solving equation (3.1) directly an equivalent system that has more favourable convergence properties is solved. For example, the system is preconditioned using a matrix $\mathbf{M}$ by forming

$$\mathbf{M}^{-1}\mathbf{A}\mathbf{x} = \mathbf{M}^{-1}\mathbf{b}. \tag{3.5}$$

Here $\mathbf{M}$ is chosen so that it approximates $\mathbf{A}$ in some way but also so that its inverse can be found with little effort. The iterative method is then applied to the matrix $(\mathbf{M}^{-1}\mathbf{A})$.

Many different preconditioning methods have been suggested for a variety of classes of matrix. The simplest is diagonal scaling, in this case $\mathbf{M} = \mathbf{D}$ where $\mathbf{D}$ is the diagonal of $\mathbf{A}$. By applying it in the form

$$\left(\mathbf{D}^{-\frac{1}{2}}\mathbf{A}\mathbf{D}^{-\frac{1}{2}}\right)\left(\mathbf{D}^{\frac{1}{2}}\mathbf{x}\right) = \left(\mathbf{D}^{-\frac{1}{2}}\mathbf{b}\right), \tag{3.6}$$

then if $\mathbf{A}$ is symmetric $\left(\mathbf{D}^{-\frac{1}{2}}\mathbf{A}\mathbf{D}^{-\frac{1}{2}}\right)$ will also be symmetric. This technique of preserving symmetry is used for all the preconditioners considered here. Preconditioning using (3.6) is no more than symmetrical scaling of the coefficient matrix so that its diagonal elements are ones. Although simple this method is not very effective for general problems, however, it can be extremely effective for the matrices arising from the time domain discretisation.

Another type of preconditioner, suitable for symmetric matrices, uses an SSOR decomposition, where the matrix is factored as

$$\mathbf{M} = \frac{1}{(2-\omega)}\left(\frac{1}{\omega}\mathbf{D} + \mathbf{L}\right)\left(\frac{1}{\omega}\mathbf{D}\right)^{-1}\left(\frac{1}{\omega}\mathbf{D} + \mathbf{L}\right)^{T} \tag{3.7}$$

where ω is the over-relaxation parameter and where the original matrix is given by $\mathbf{A} = \mathbf{D} + \mathbf{L} + \mathbf{L}^T$, The diagonal matrix $\mathbf{D}$ contains the diagonal entries of $\mathbf{A}$ while $\mathbf{L}$ contains the lower triangular entries. The choice of the parameter ω is not as critical when SSOR is used as a preconditioner compared to its use as an iterative solver in its own right [Evans, 1967]. One advantage of this method is that it requires no extra storage and there is no construction cost since $\mathbf{D}$ and $\mathbf{L}$ are already available. One can also use the procedure given by Eisenstat [1981] to reduce the amount of computation at each iteration to be only slightly greater than that for the unpreconditioned system.

Preconditioners based on an incomplete factorization were first[3] proposed by Varga [1960]. A factorization is incomplete if during during the factorization process some of the zero entries that would normally be filled in are ignored. The degree to which $\mathbf{M} = \mathbf{LU}$ approximates $\mathbf{A}$ determines the effectiveness of the preconditioner. Since some fills have been ignored it is possible that the factorization may break down, due

---

[3] Nicolaides & Choudhury [1986] state that a paper by Buleev [1960] also contains this idea.

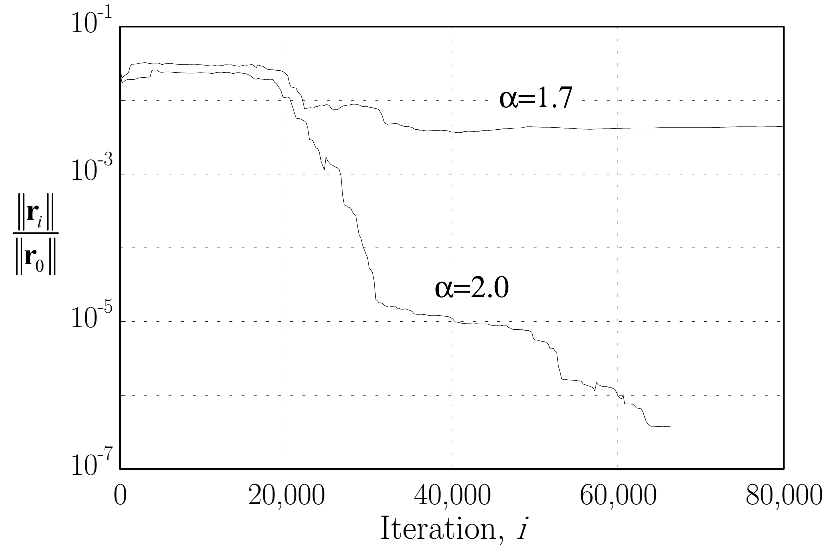

Figure 3.2: Effect of α on convergence for the SIC-QMR algorithm for a multimode cavity loaded with mashed potato ($n = 51,506$).

to a division by zero or result in an indefinite matrix $\mathbf{M}$, having negative diagonal entries, that will result in the iterative method failing to converge. The application of incomplete factorization as a preconditioner for the CG method was first carried out by Meijerink & van der Vorst [1977] who also proved that if the coefficient matrix is an M-matrix[4] then the incomplete factorization is guaranteed to exist. Kershaw [1978] applied the technique to a wider class of matrices from laser fusion problems, proposing that if the pivot entry became negative then it should be replaced by a positive number to prevent the breakdown of the factorization. Manteuffel [1980] suggested the use of shifted incomplete Cholesky factorization (SIC). If the original matrix is split $\mathbf{A} = \mathbf{D} - \mathbf{B}$ where $\mathbf{D}$ is the diagonal of the matrix then the factorization is applied to the system

$$(1 + \alpha)\mathbf{D} - \mathbf{B}. \tag{3.8}$$

The quantity α is chosen so that the factorization is positive. Since constructing the incomplete factorization is generally very fast compared to the overall solution time

---

[4] A matrix $\mathbf{A} = (a_{ij})$ is an M-matrix if $a_{ij} \leq 0$ for $i \neq j$, $\mathbf{A}$ is nonsingular and $\mathbf{A}^{-1} \geq 0$.

the process can be repeated with different values of α until a positive factorization is obtained. Figure 3.2 shows the value of the relative residual norm against iteration, i, for two values of α. When $\alpha = 1.7$ the factorization contains one pivot that has a negative real part and convergence stops after $\sim 22,000$ iterations, whereas when $\alpha = 2.0$ is chosen all pivots have positive real parts and the method converges slowly.

Several possible techniques for generating the incomplete factorization exist. The most common, which is used here, is to force $\mathbf{L}$ to have the same sparsity pattern as the original matrix. This has the immediate advantage of not requiring further storage to hold the structure of $\mathbf{L}$ since it is the same as that of $\mathbf{A}$ with only the values being different. The factorization is constructed as a normal Cholesky factorization [George & Liu, 1981] except all elements that are zero in $\mathbf{A}$ remain zero in $\mathbf{L}$. An alternative, often called ICCG(0) or ILU(0) [Meijerink & van der Vorst, 1981] is to write $\mathbf{M}$ as

$$\mathbf{M} = \left(\tilde{\mathbf{D}} + \mathbf{L}\right)\left(\tilde{\mathbf{D}}\right)^{-1}\left(\tilde{\mathbf{D}} + \mathbf{L}^T\right) \tag{3.9}$$

where $\mathbf{L}$ is the lower triangular part of $\mathbf{A}$. This approach is similar to the SSOR preconditioner except that now $\tilde{\mathbf{D}}$ is chosen such that

$$\text{diag}(\mathbf{M}) = \text{diag}(\mathbf{A}). \tag{3.10}$$

As well as only requiring storage for $\tilde{\mathbf{D}}$ this technique also allows the use of the procedure given by Eisenstat [1981] to reduce the amount of computation at each iteration to be similar to that required for the unpreconditioned system.

Gustafsson [1978] developed a further modification to the factorization process; instead of using (3.10) the matrix $\tilde{\mathbf{D}}$ is chosen so that the row sums of $\mathbf{M}$ are equal to the row sums of $\mathbf{A}$. This factorization is known as modified incomplete Cholesky (MICCG) and has the property of reducing the condition number from an $O(h^{-2})$ dependence to $O(h^{-1})$ for certain problems arising from 5-point and 7-point finite difference discretisations, where h is a measure of the size of the discretisation. The method does, however, increase the likelihood of breakdown. If the SIC method is used to prevent breakdown then the row sum criteria cannot apply.

Many other preconditioners exist, for example the polynomial preconditioner which can be effective with parallel machines that have a very large number of processors

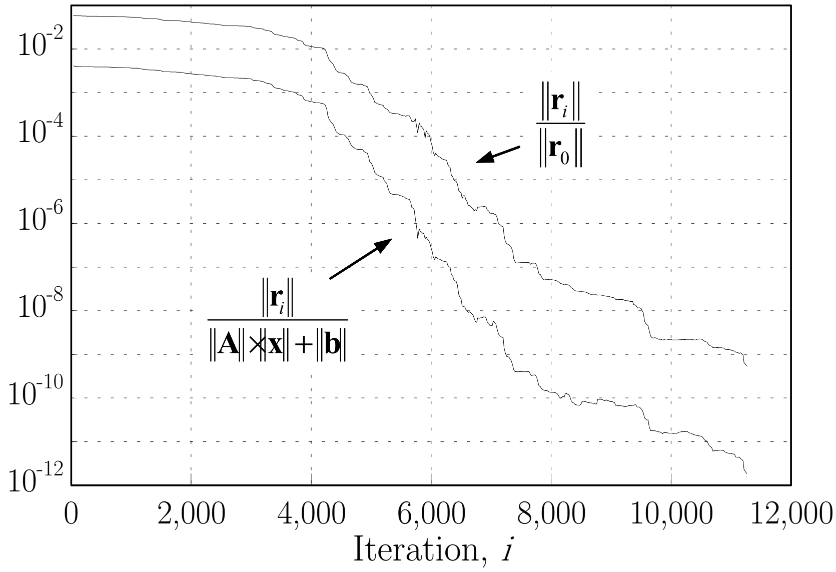

Figure 3.3: Comparison of two methods of determining convergence ($\mathbf{x}_0 = 0$).

[van der Vorst, 1989]. Multigrid [Nicolaides & Choudhury, 1986] and domain decomposition [Cai & Widlund, 1992] methods are currently the subject of much research, however, as Ramage & Wathen [1994] point out most of these are developed and tested on problems using regular grids, often in two dimensions. Their performance in this environment can be exceptional but extending this to irregular tetrahedral meshes in three dimensions is often very difficult. Multigrid methods require a series of meshes and functions to interpolate and extrapolate values from one to another. This is a difficult requirement for general problems where many geometries may require a fine mesh simply to represent the dimensions of the problem accurately. Domain decomposition methods require the problem to be broken into a number of separate regions. In some cases the splitting is obvious from the geometry of the problem [Ise *et al.*, 1990], however, for the general case this is not so.

3.3.4 Terminating Criteria

The iterative techniques described above need some measure of the error to determine when a suitable accuracy has been reached. The true error $\|\delta\mathbf{x}_i\|$ is generally unavailable so it is usual to base the terminating criteria on the residual norm $\|\mathbf{r}_i\|$ instead. Some method of normalising $\|\mathbf{r}_i\|$ is required since its absolute magnitude will depend upon the nature of the problem. One of the more common choices is to monitor the ratio $\|\mathbf{r}_i\|/\|\mathbf{r}_0\|$ where $\|\mathbf{r}_0\|$ is the norm of the initial residual. When $\mathbf{x}_0 = 0$ is chosen initially then this is also equivalent to $\|\mathbf{r}_i\|/\|\mathbf{b}\|$, another common measure. An alternative, given by Barret *et al.* [1993] is to choose

$$\frac{\|\mathbf{r}_i\|}{\|\mathbf{A}\| \cdot \|\mathbf{x}_i\| + \|\mathbf{b}\|}. \tag{3.11}$$

Figure 3.3 shows the behaviour of both criteria for a typical problem using the SIC-QMR algorithm. The shapes of the two curves is very similar with the second method giving a value which is consistently smaller. This would suggest that either method can be used to determine convergence with the stopping tolerance being chosen appropriately.

3.4 Ill-Conditioning

The magnitude of the condition number $\kappa(\mathbf{A})$ of the matrix $\mathbf{A}$ has important consequences for the solution of the linear system (3.1). The condition number, which is defined by

$$\kappa(\mathbf{A}) = \|\mathbf{A}\| \cdot \|\mathbf{A}^{-1}\|, \tag{3.12}$$

has two main effects. Firstly it measures the sensitivity of the system to small changes. If the right hand side of (3.1) is perturbed by $\delta\mathbf{b}$ and the matrix $\mathbf{A}$ is changed by a small amount $\delta\mathbf{A}$ then the relative change in $\mathbf{x}$ is bounded by [Duff *et al.*, 1986]

$$\frac{\|\delta\mathbf{x}\|}{\|\mathbf{x}\|} \leq \frac{\kappa(\mathbf{A})}{1 - \kappa(\mathbf{A})\dfrac{\|\delta\mathbf{A}\|}{\|\mathbf{A}\|}} \left(\frac{\|\delta\mathbf{b}\|}{\|\mathbf{b}\|} + \frac{\|\delta\mathbf{A}\|}{\|\mathbf{A}\|} \right). \tag{3.13}$$

Small changes in the excitation frequency or in the boundary conditions of the finite element system will produce small changes in both $\mathbf{A}$ and $\mathbf{b}$. If the condition number is large then these small changes can produce very large changes in the solution vector $\mathbf{x}$. In practice multimode cavities often show large variations in field patterns when subject to small perturbations which would suggest that the matrices arising from the discretisation of multimode systems are likely to possess large condition numbers (see §1.2.2).

The condition number also gives an upper bound on the relative error in the computed solution, $\mathbf{x}$, for a given residual $\mathbf{r} = \mathbf{b} - \mathbf{A}\mathbf{x}$, we get

$$\frac{\|\delta \mathbf{x}\|}{\|\mathbf{x}\|} \leq \kappa(\mathbf{A}) \frac{\|\mathbf{r}\|}{\|\mathbf{b}\|}. \tag{3.14}$$

For ill-conditioned matrices the error in the solution may be large even when the residual is small. This is an important observation when considering the stopping criteria for iterative methods where the actual error in the solution $\|\delta \mathbf{x}\|$ is unavailable and the criteria has to be based on the residual. As the condition number increases it is necessary to lower the level to which the residual must be reduced in order to ensure an accurate solution.

The condition number also affects the rate of convergence of conjugate gradient type methods. Barret *et al.* [1993] give the following result for the convergence of the standard conjugate gradient method,

$$\|\delta \mathbf{x}_i\|_A \leq 2 \left(\frac{\sqrt{\kappa_2} - 1}{\sqrt{\kappa_2} + 1} \right)^i \|\delta \mathbf{x}_0\|_A \tag{3.15}$$

where $\|\delta \mathbf{x}_i\|_A$ is the error in the solution at iteration i and $\|\mathbf{y}\|_A \equiv (\mathbf{y}, \mathbf{A}\mathbf{y})$. The rate of convergence is therefore dependent upon $\sqrt{\kappa}$. A large condition number has the dual effect of producing slow convergence and requiring the residual to be reduced to a lower level to ensure an acceptable accuracy.

3.4.1 ESTIMATION OF THE CONDITION NUMBER

The calculation of the condition number for a general matrix cannot be carried out cheaply. The exact calculation would require the formation of the inverse, a process which is computationally very expensive. Many alternative methods of estimating the condition number have been proposed that avoid the formation of the inverse. These often require the solution of several sets of linear equations (3.1) with different right hand sides [Hager, 1984]. An alternative is the LINPACK estimator [Cline *et al.*, 1979] which requires the construction of a special vector during the back substitution phase of

Gaussian elimination. If Gaussian elimination is used for the solution of (3.1) then the condition number can be found at little *extra* cost using Hager's algorithm, however, if iterative techniques are used then this method will be very slow unless the matrix is very well conditioned.

For real symmetric positive definite matrices the condition number can also be found from

$$\kappa_2(\mathbf{A}) = \frac{\lambda_{max}(\mathbf{A})}{\lambda_{min}(\mathbf{A})}. \tag{3.16}$$

So if the extremal eigenvalues are known then the condition number can be found. The Lanczos process, which is closely related to the conjugate gradient method can be used to find these eigenvalues during the solution of the linear system at the cost of a few extra vector operations. However, in the frequency domain the matrices are not, in general, positive definite so equation (3.16) does not apply. It would still be possible to use the Lanczos method by applying it to the normal equations $\mathbf{A}^H\mathbf{A}$ which are real symmetric positive definite and using the relation [Barret *et al.*, 1993],

$$(\kappa_2(\mathbf{A}))^2 = \frac{\lambda_{max}(\mathbf{A}^H\mathbf{A})}{\lambda_{min}(\mathbf{A}^H\mathbf{A})}. \tag{3.17}$$

However, while an accurate value of λ_{max} is available from the Lanczos method after only a few iterations, a good estimate of λ_{min} is not obtained until the algorithm has converged. Since the normal equations are involved convergence will be very slow for large ill-conditioned problems which makes this method unattractive. Consequently values for the condition number of the large frequency domain systems considered in this thesis are not given.

3.5 Application to the Frequency Domain Method

The convergence behaviour of the iterative techniques, when applied to frequency domain problems, shows significant differences for multimode cavities and single mode cavities. The performance for single mode systems is generally very good whereas convergence sometimes is often very slow for multimode cavities. This section is therefore split into two, with the systems being discussed separately.

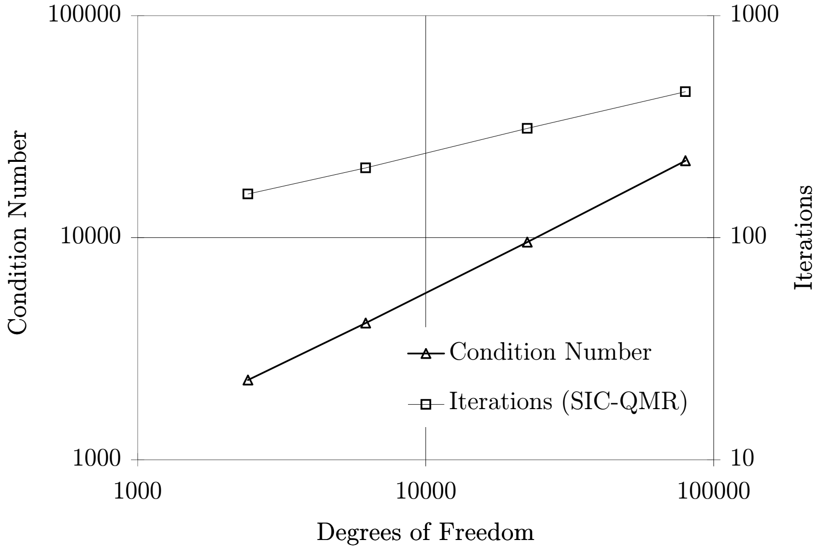

Figure 3.4: Condition number of the coefficient matrix and number of iterations required for the SIC-QMR method against the number of degrees of freedom for a short circuit waveguide, (WG9A 400 mm long).

3.5.1 Single Mode and Waveguide Problems

The condition number is dependent upon both the mesh discretisation and the nature of the problem being modelled. Figure 3.4 shows the increase in the condition number as the mesh is refined for a simple short circuit waveguide problem. The condition number in this problem remains relatively small and so no accuracy difficulties are encountered when the system is solved using double precision arithmetic. The number of iterations required to solve these problems are shown in Table 3.2, very rapid convergence being obtained with the number of iterations required being considerably less than the order of the matrices. Also shown are the results for a TM_{010} cavity problem (see §5). The times for solution on a Sparc-10 workstation are also given. They should be treated as a rough indication only since they are very dependent on both the machine used for the computation and the degree to which the code has been optimised. Generally, the number of iterations for the solution provides a better indication of the efficiency of the method since it will be machine independent.

Problem	Degrees of Freedom	Iterations	Time
S/C Waveguide	2,415	157	40 seconds
S/C Waveguide	6,196	206	1.5 minutes
S/C Waveguide	22,542	310	7 minutes
S/C Waveguide	79,821	454	38 minutes
TM_{010} cavity	21,976	1,144	26 minutes

Table 3.2: Number of iterations required for the SIC-QMR method to reduce the residual below 5×10^{-10}.

The waveguide problem is relatively simple, there are no resonant modes and the solution varies as a smooth function of frequency giving a small condition number. A consequence of which is the very rapid convergence seen for these systems. Even for the single mode system loaded with high permittivity material, such as the TM_{010} cavity containing a tubular water load, the rapid convergence is still apparent. The frequency domain method is therefore ideally suited to solving this type of problems as the SIC-QMR method provides a very fast technique for solving the resulting set of linear equations.

3.5.2 Multimode Cavity Problems

Multimode cavity problems by their very nature possess many resonant modes. This has the effect of significantly increasing the condition number of the system, even when the mesh is relatively coarse. In practice this manifests itself by producing very slow convergence of the conjugate gradient method. The performance of both the Bi-CG method and QMR methods were tested for the linear system arising from the frequency domain discretisation of a cavity loaded with a tray of mashed potato. One quarter of the problem was modelled. The field results for this problem are discussed in §6.4 along with a more detailed description of the geometry. Figure 3.5 shows the comparative rates of convergence for the two methods with and without preconditioning using shifted incomplete Cholesky factorization. The convergence rates are very similar for both the QMR and Bi-CG algorithms, with the QMR giving smoother convergence as expected.

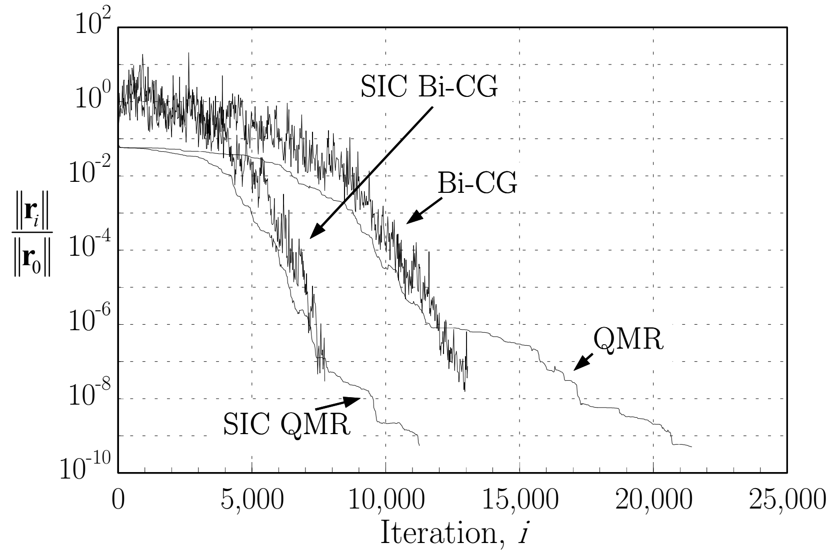

Figure 3.5: Convergence of the QMR and Bi-CG algorithms with and without preconditioning for a multimode cavity containing a mashed potato load. (Mesh 1 of Table 3.3)

The preconditioner is effective at reducing the number of iterations, however, a large number of iterations were still needed to produce a satisfactorily small residual.

The mesh used for Figure 3.5 was very coarse so further tests were carried out using a total of three different meshes with differing degrees of refinement. Table 3.3 gives the number of degrees of freedom and the number of non-zeros in the coefficient matrix for the three meshes. The first mesh was a coarse mesh with a small amount of refinement near the waveguide aperture and in the potato. The second mesh had more refinement inside and around the dielectric while the third mesh was refined throughout the whole domain. It can be seen from Figure 3.6 that the first two meshes produce systems that converge in a number of iterations approximately equal to half the number of degrees of freedom whereas the third shows much slower convergence. Since the rate of convergence is dependent upon the condition number this would suggest meshes 1 and 2 produce a system with a moderate condition number giving fairly slow convergence. Mesh 3 would appear to have a much higher condition number that causes the very slow convergence

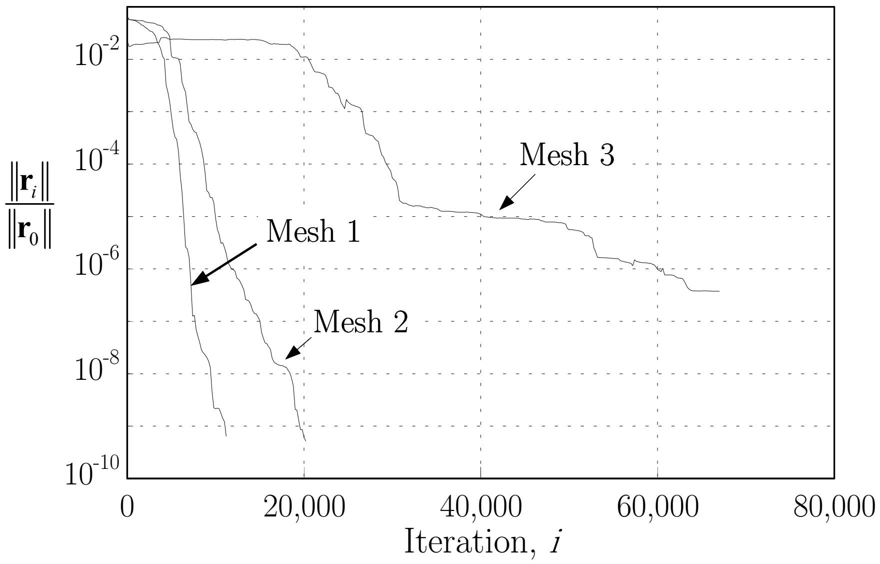

Figure 3.6: Reduction in the residual using the SIC-QMR algorithm with three different meshes for the mashed potato problem.

of the SIC-QMR algorithm.

The major difference between meshes 2 and 3 is the discretisation of the air in the cavity. The former has a very coarse discretisation with the largest elements being approximately one fifth of a wavelength in size while mesh 3 has elements of approximately one tenth of a wavelength. Meshes 1 and 2 cannot be expected to give good accuracy because of this coarse discretisation: a coarse mesh being able to only represent a small number of mode patterns accurately so artificially restricting the solution, and therefore the accuracy. The finer mesh allows considerably more modes to be represented by the discretisation, some of these modes may have high Q-factors, and indeed as suggested by Bossavit [1995] may be "air modes", that is, ones with an infinite Q-factor. The presence of these modes near or at the excitation frequency may cause a loss of uniqueness of the solution in the *discrete* problem and result in a very ill-conditioned system even though the continuous problem is well posed. This very slow convergence seems to be characteristic of multimode cavities when loaded with a dielectric having a high permittivity.

Mesh	Degrees of Freedom	Non Zeros	Final Residual	Iterations	Time
1	22,600	365,148	4.9×10^{-10}	11,270	4 hours
2	39,278	649,246	5.0×10^{-10}	20,316	10 hours
3	51,388	832,002	3.7×10^{-7}	67,000	43 hours

Table 3.3: Comparison of performance of SIC-QMR for three meshes used for the mashed potato problem.

To determine the effect of the permittivity of the load on the convergence, the problem was re-run using mesh 3 but with different values of the permittivity and the results are shown in Figure 3.7. As the permittivity of the load increases the convergence of the SIC-QMR method becomes progressively slower. The increase in condition number with increasing variation in material properties has been noted previously [Vavasis, 1993]. In multimode cavities this may be due to the higher number of modes that are capable of being supported by the more heavily loaded cavity. The higher permittivity will also cause more energy to be reflected from the surface of the load, in some cases this will reduce the coupling of a particular mode to the load. This is a serious computational problem since for microwave heating it is common to have a large cavity loaded with a large block of dielectric which has both a high permittivity and high loss factor, the example of mashed potato being typical.

At each iteration of the SIC-QMR it is necessary to perform two substitutions (one forward, one backward) plus a matrix-vector multiplication which will require a total of $\approx 2\tau_c$ complex floating point operations. The use of ICCG(0) preconditioning in conjunction with Eisenstat's procedure may allow this to be reduced to $\approx \tau_c$, halving the work per iteration. Even so when the number of iterations required for realistic loads of food like materials is $> n$ the solutions will take a considerable amount of time as shown in Table 3.3 unless a supercomputer is used.

The problems examined here are relatively small, with the largest having 51,000 unknowns. Many problems will be considerably larger making the slow convergence even more problematic since the work per iteration will increase. The larger problems are also

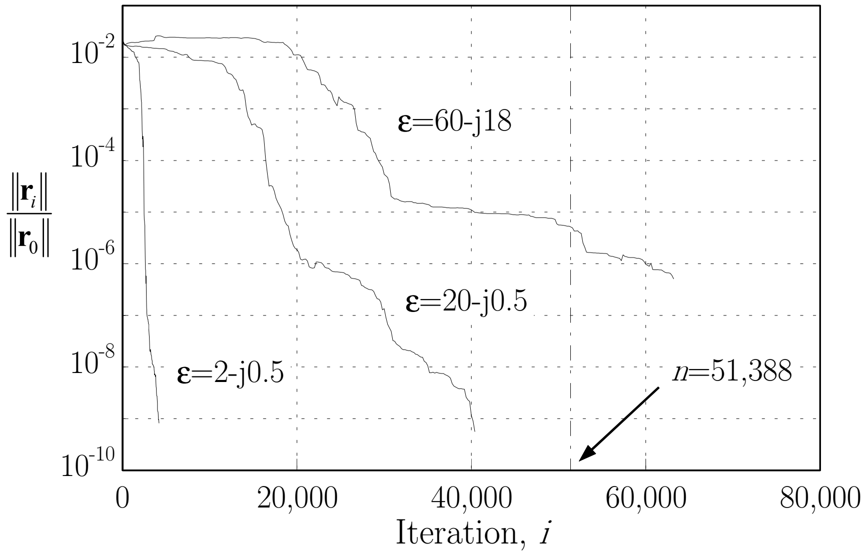

Figure 3.7: Effect of the permittivity on the convergence of the SIC-QMR algorithm using mesh 3.

likely to have larger condition numbers to further exacerbate the problem. These small examples were chosen since convergence could be achieved while still demonstrating the problems of using the frequency domain method for multimode cavities. The use of other preconditioners, such as multigrid, may improve the situation but a considerable amount of research is required for this to be realizable for microwave heating problems.

3.6 Application to the Time Domain Method

The time domain finite element method produces a matrix **A** which is both real and symmetric so that the CG method can be used. Furthermore, it is found that the condition number of this matrix is generally very small so that an accurate solution can be found after only a few iterations. As stated in §2.4 a good initial guess, $\mathbf{x}_0$ is also available which can be used to reduce the solution time. This section compares the performance of various methods and preconditioning strategies for the solution of the time domain system. The matrices from the time domain discretisation for multimode cavities and single mode systems show very similar behaviour so are dealt with together in this section.

3.6.1 DIAGONAL SCALING

		Condition Number	
Problem	n	Diagonal Scaling	No Scaling
S/C Waveguide	6,196	4.83	11.08
S/C Waveguide	80,334	3.73	9.00
S/C Waveguide (irregular mesh)	13,525	9.35	28.46
TM_{010} cavity (Prism elements)	22,174	241.78	3223.36
Mashed Potato loaded cavity	51,506	31.3	1439.24

Table 3.4: Condition number, $\kappa_1(\mathbf{A})$ of the matrices from the TDFE discretisation of various three dimensional problems (30 time steps/cycle).

Table 3.4 compares the condition numbers, calculated using Hager's algorithm, for several problems with and without diagonal scaling. Since the condition numbers are very low the solution of the linear systems required by the algorithm can be carried out very quickly. It is interesting to note that for the waveguide problem the condition number actually reduced slightly as the mesh was refined, the complete reverse of the frequency domain case. The first two waveguide problems have meshes produced by dividing the domain into a regular hexahedral mesh and then splitting each hexahedron into five tetrahedra. This produces a mesh with only ten distinct shapes and orientations of the elements. The irregular mesh was produced using GEOMPACK which produces the tetrahedra directly using a Delaunay technique. The irregular mesh has a larger number of element sizes and orientations which produces a higher condition number. If nodal elements were used then the condition number of the mass matrix ($[\mathbf{T}_\epsilon]$) becomes independent of both element size and shape and the size of the mesh [Wathen, 1987]. This is not the case for edge elements, and when an implicit time stepping scheme is used $\mathbf{A}$ contains contributions from $[\mathbf{S}]$ and it does not hold for nodal elements either. The TM_{010} cavity mesh was constructed from prism elements the size of which varied greatly throughout the mesh (see §5). This is the cause of the relatively large condition number.

The mesh used for the cavity loaded with mashed potato has localised refinement near the aperture and in the dielectric which produces elements with different sizes and orientations. This, coupled with the large variation in material properties causes the condition number, prior to scaling, to be significantly larger than for the waveguide problems which have uniform dielectric properties. Scaling has the effect of removing the dependency of the condition number on material properties. Since diagonal scaling is so effective at reducing the condition number it has been used for all the calculations. The equations being scaled before the application of any further preconditioning.

3.6.2 Direct Methods

Direct methods suffer from exactly the same memory problems when applied to the time domain solution as for the frequency domain problem. This makes them applicable only to very small problems where they may be competitive with iterative methods. In §3.2 it was suggested that if the number of iterations, k, required for an iterative solution of (3.1) satisfied $k\tau_c < \tau_f$ then the iterative method would be faster. For the smallest problem considered in Table 3.1 we see that $\tau_f \approx 5\tau_c$, however, the very low condition number means that only 2–3 iterations of the SSOR-CG method is required, so even for this small problem the iterative method should be faster. For the larger problems the difference is much greater.

3.6.3 SOR Iteration

The time domain method permits the solution of equation (3.1) using SOR or Gauss-Seidel iteration. This method is very simple and can give good results when the initial guess is chosen according to (2.33). The SOR algorithm has a performance which is very dependent upon the choice of the over relaxation parameter ω. However, since we are solving many systems in succession, one at each time step, it is possible to continually vary ω and therefore dynamically optimise its value during the calculation.

Table 3.5 shows the performance of the SOR method for various problems along with the value of ω used. The systems were diagonally scaled prior to starting the SSOR

Problem	n	Iterations	ω
S/C Waveguide	2,532	8	1.29
S/C Waveguide	22,812	8	1.27
S/C Waveguide	80,388	11	1.26
TM_{010} cavity	22,174	11	1.24
Mashed potato loaded cavity	51,506	11	1.21

Table 3.5: Performance of SOR iteration for different TDFE problems.

iteration.

3.6.4 Preconditioned Conjugate Gradients

The preconditioned conjugate gradient method was applied to the mashed potato loaded cavity problem. Table 3.6 shows the number of iterations required to reduce the residual to 1×10^{-6} both with and without SSOR preconditioning and for different initial guesses for $\mathbf{x}_0$. The system of equations was diagonally scaled prior to starting the solution for all problems. SSOR preconditioning was chosen since it allows Eisenstat's procedure to be used which means the work per iteration for the preconditioned and unpreconditioned systems is about the same and no extra storage is required. Table 3.6 clearly shows the effectiveness of this preconditioner for this particular problem. The use of $\mathbf{x}_0 = 0$ has the advantage that, since $\mathbf{r}_0 = \mathbf{b}$ no matrix-vector multiplication is required prior to starting the iteration. This is not the case for the other two initial guesses where it is necessary to calculate the residual. The first and third options for choosing $\mathbf{x}_0$ appear equally good, however, it is found that option three is slightly better because it causes the number of iterations at each time step to be reduced slightly as the solution approaches the steady state condition. The results in Table 3.6 show that the SSOR preconditioned conjugate gradient method, when coupled with diagonal scaling, gives a very effective method of solving the system in the time domain.

Initial Guess	No Preconditioning	SSOR Preconditioning
$\mathbf{x}_0 = 0$	11–12	4
$\mathbf{x}_0 = \mathbf{b}$	10	4
$\mathbf{x}_0 = 2\mathbf{e}_n - \mathbf{e}_{n-1}$	6	3

Table 3.6: Average number of iterations required for mashed potato loaded cavity problem for different preconditioners and initial guesses.

3.7 Conclusions

This chapter has investigated the various techniques that can be used for the solution of the linear system of equations arising from the finite element discretisation. Direct methods are applicable only to small matrices and so are generally unsuitable for microwave heating problems. The equations arising from the frequency domain finite element method can be solved using the QMR algorithm with shifted incomplete Cholesky preconditioning. Convergence for the multimode cavity problems, however, is very slow. When applied to single mode applicators the finite element method produced a system of equations which is very amenable to solution with this method.

The system arising from the time domain discretisation can be solved in very few iterations. The combination of SSOR preconditioning and the conjugate gradient method was seen to be particularly efficient, allowing solution in as few as 3 iterations. The effect of different starting values was investigated and the most effective choice being found to be that obtained from values of the field at previous time steps.

Chapter

4

Calculation of the Reflection Coefficient and Absorbed Power

4.1 Introduction

A simple determination of the normalised electric field distribution inside the cavity and the load is in itself insufficient to determine the temperature rise that will be produced in the load. It is also necessary to calculate the power density distribution and then to solve the heat flow equation to obtain the temperatures. Discussion of the heat flow equation will be postponed until Chapter 7. This chapter discusses the determination of the reflection coefficient and the power density.

Some of the energy supplied to the applicator will be reflected back to the source. The calculation of the amount of reflected energy is necessary in order to determine the amount of energy that will be absorbed by the load being heated.

4.2 Calculation of Reflection Coefficient

The reflection coefficient for a multimode applicator can be found by considering the field in the feed waveguide. It is assumed that only the TE_{10} mode is present in the guide, so by considering the magnitude and phase of the field at two planes inside the waveguide, as shown in Figure 2.3, the reflection coefficient can be found [de Pourcq, 1984]. When using a modulated Gaussian pulse to excite the system, the instantaneous

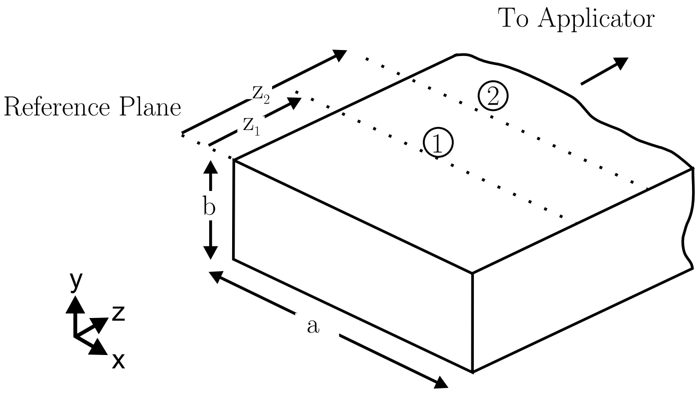

Figure 4.1: Planes in waveguide for the calculation of reflection coefficient

values of the field at these planes are recorded at each time step. Then either a fast Fourier transform (FFT) or a discrete Fourier transform (DFT) can be performed in order to obtain the field values at a range of frequencies either side of the modulating frequency [Ma *et al.*, 1994]. These values are then used to find the reflection coefficient over the frequency range.

The reflection coefficient can be calculated from the field inside the waveguide. If we assume that only a TE_{10} mode exists in the waveguide, then the transverse field is described by [de Pourcq, 1984],

$$\mathbf{E}_{\mathrm{tr}} = (Ae^{-\jmath\beta z} + Be^{\jmath\beta z})\sqrt{\frac{2}{ab}}\sin\frac{\pi x}{a}\hat{\mathbf{j}} \tag{4.1}$$

$$\mathbf{H}_{\mathrm{tr}} = -\frac{1}{Z_w}(Ae^{-\jmath\beta z} - Be^{\jmath\beta z})\sqrt{\frac{2}{ab}}\sin\frac{\pi x}{a}\hat{\mathbf{i}} \tag{4.2}$$

where A is the amplitude of the forward travelling wave and B the amplitude of the reflected wave travelling in the opposite direction. The constant β is the phase constant, which for the TE_{10} mode in an air filled waveguide is given by,

$$\beta = \sqrt{\omega^2\mu_0\epsilon_0 - \left(\frac{\pi}{a}\right)^2}. \tag{4.3}$$

The $\sqrt{\frac{2}{ab}}$ term appears in equations (4.1) and (4.2) so that the integral over the waveguide cross section, S, of the TE_{10} mode eigenvector $\vec{e}$ is normalised [de Pourcq, 1984]

$$\int_S |\vec{e}|^2 \,\mathrm{d}S = 1. \tag{4.4}$$

The reflection coefficient is given by the ratio of reflected to forward waves,

$$\rho = \frac{B}{A}\, e^{\jmath 2\beta z}, \tag{4.5}$$

and the impedance as seen looking towards the applicator from the reference plane is given by [Collin, 1992]

$$Z = Z_w \frac{1+\rho}{1-\rho}, \tag{4.6}$$

where Z_w is the intrinsic characteristic impedance of the waveguide, given by

$$Z_w = Z_0 \frac{\lambda_g}{\lambda_0}. \tag{4.7}$$

where λ_g is the waveguide wavelength,

$$\lambda_g = \frac{\lambda_0}{\sqrt{1-\left(\dfrac{\lambda_0}{2a}\right)^2}} \tag{4.8}$$

Considering the transverse component of the field at two planes z_1 and z_2 in the waveguide, as shown in Figure 4.1, we get from equation (4.1)

$$A = \sqrt{\frac{ab}{2}}\frac{1}{\sin\frac{\pi x}{a}}\left[\frac{E_y(x,y,z_1)e^{-\jmath\beta z_1} - E_y(x,y,z_2)e^{-\jmath\beta z_2}}{e^{-2\jmath\beta z_1} - e^{-2\jmath\beta z_2}}\right] \tag{4.9}$$

$$B = \sqrt{\frac{ab}{2}}\frac{1}{\sin\frac{\pi x}{a}}\left[\frac{E_y(x,y,z_1)e^{+\jmath\beta z_1} - E_y(x,y,z_2)e^{+\jmath\beta z_2}}{e^{+2\jmath\beta z_1} - e^{+2\jmath\beta z_2}}\right] \tag{4.10}$$

where $E_y(x,y,z_1)$ and $E_y(x,y,z_2)$ are point values of the electric field.

de Pourcq [1984] notes that better results can be obtained for the reflection coefficient if $E_y(x,y,z_1)$ and $E_y(x,y,z_2)$ in equations (4.9) and (4.10) are replaced by integrals over the cross section of the guide:

$$I_1 = \int_{S_1} \{E_y(x,y,z_1)\cdot\vec{e}\}\,\mathrm{d}S_1, \tag{4.11}$$

$$I_2 = \int_{S_2} \{E_y(x,y,z_2)\cdot\vec{e}\}\,\mathrm{d}S_2. \tag{4.12}$$

This ensures that only the field values corresponding to the TE_{10} mode are used: it also solves the problem of where on the cross section to select $E_y(x,y,z_1)$ and $E_y(x,y,z_2)$.

Substituting from (4.1) into (4.11) produces,

$$\begin{aligned} I_1 &= \int_S \left\{ \left((Ae^{-\jmath\beta z_1} + Be^{\jmath\beta z_1}) \sqrt{\frac{2}{ab}} \sin\frac{\pi x}{a} \right) \cdot \left(\sqrt{\frac{2}{ab}} \sin\frac{\pi x}{a} \right) \right\} \mathrm{d}S \\ &= Ae^{-\jmath\beta z_1} + Be^{\jmath\beta z_1} \end{aligned} \tag{4.13}$$

and similarly for I_2. Therefore, rearranging gives

$$A = \frac{I_1 e^{-\jmath\beta z_1} - I_2 e^{-\jmath\beta z_2}}{e^{-2\jmath\beta z_1} - e^{-2\jmath\beta z_2}} \tag{4.14}$$

$$B = \frac{I_1 e^{+\jmath\beta z_1} - I_2 e^{+\jmath\beta z_2}}{e^{+2\jmath\beta z_1} - e^{+2\jmath\beta z_2}} \tag{4.15}$$

In order to simplify the calculation of the integrals (4.11) and (4.12) the mesh used for the discretisation is constructed such that there are a number of x-y planes in the waveguide formed by element faces: that is no elements are cut by these planes. The tangential field on these planes is therefore described entirely by the edges of the mesh that lie on the plane. For each triangular face that lies on the plane the integral over that face is found using quadrature integration [Ciarlet, 1978]. If the midpoint of an edge, i, belonging to a triangular face, f, is given by (x_i, y_i, z_i) then the integral (4.11) over that face is given by

$$I_f = \frac{A}{3} \sum_{i=1}^{3} \left\{ \mathbf{w}_i(x_i, y_i, z_i) \cdot \hat{\mathbf{j}} \right\} \sin\left(\frac{\pi x_i}{a}\right) e_i, \tag{4.16}$$

where A is the area of the face. The integrals (4.11) and (4.12) are then calculated from the summation of the integrals over each face on two different planes respectively. Four points inside the face are used for the integration over the faces of hexahedral elements. As an alternative it would be possible to calculate the integrals from the smoothed solution (see §2.6) rather than from the edge values.

4.3 Power Calculation

The power density can be obtained directly from the electric field using the simple expression [Metaxas & Meredith, 1983],

$$p_v = \frac{1}{2}\sigma_e |\mathbf{E}|^2 \qquad \mathrm{W\,m^{-3}}. \tag{4.17}$$

The electric field values calculated by the finite element method, however, will be normalised to some value depending on the technique used to apply the boundary conditions. To proceed with a temperature calculation it is necessary to know absolute values of the power density. This can be achieved in one of two ways. One approach is to find the absolute values of the electric field from which the power density can be found. This requires knowledge of the magnitude of the field at some point in the domain, say in the waveguide feed. This can be calculated if the power flowing in the guide is known. The other method is to consider the total power dissipated inside the cavity and match that to the total power that is supplied.

4.3.1 Power Calculation by E-Field Scaling

The power flowing in the waveguide is given by the integral of the Poynting vector over the cross section of the waveguide,

$$P = \frac{1}{2}\Re e \int_0^a \int_0^b \mathbf{E} \times \mathbf{H}^* \cdot \hat{\mathbf{z}} \, \mathrm{d}y \, \mathrm{d}x. \tag{4.18}$$

Substituting the $\mathbf{E}$ and $\mathbf{H}$ fields for the TE_{10} mode using equations (4.1) and (4.2) and considering only the forward wave gives,

$$\begin{aligned} P_f &= \frac{1}{2}\Re e \int_0^a \int_0^b -E_y \, H_x^* \, \mathrm{d}y \, \mathrm{d}x, \\ &= \frac{1}{2Z_w}\Re e \int_0^a \int_0^b E_y \, E_y^* \, \mathrm{d}y \, \mathrm{d}x, \\ &= \frac{|A'|^2}{2Z_w} \end{aligned} \tag{4.19}$$

where A' is the magnitude of the forward wave at power P_f. If the supplied power P_f is known then the electric field can be scaled using the magnitude of A obtained from equation (4.14),

$$\mathbf{E} = \hat{\mathbf{E}} \, \frac{\sqrt{2Z_w P_f}}{|A|}, \tag{4.20}$$

where $\hat{\mathbf{E}}$ is the normalised value of the electric field obtained directly from the finite element solution. The power density calculated from this $\mathbf{E}$ field will be absolute values.

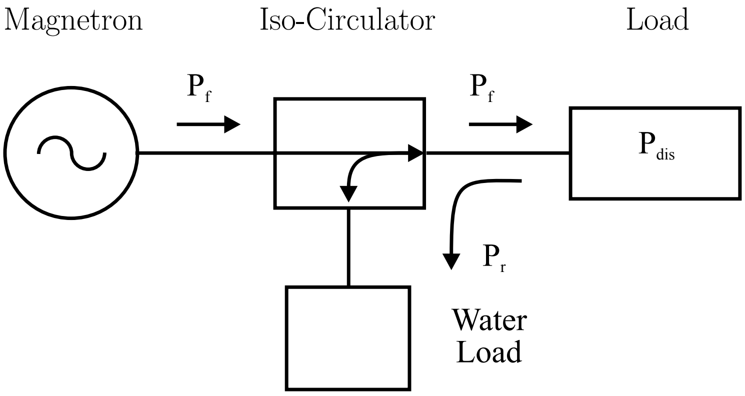

Figure 4.2: Power flows when an iso-circulator is used

4.3.2 Power Calculation by Scaling Total Power

The absolute values of the power density can also be found by calculating the total power dissipated in the material and relating this to the power being supplied to the cavity. Having found the reflection coefficient in the feed waveguide the power dissipated in the cavity, P_{dis}, can be determined from,

$$P_{dis} = P_f(1 - |\rho|^2), \tag{4.21}$$

where P_f is the forward power supplied by the magnetron, as shown in Figure 4.2. The field inside the cavity can now be scaled so that the power calculated from the integral of equation (4.17) over the cavity,

$$P = \frac{1}{2}\int_{\Omega} \sigma_e |\mathbf{E}|^2 \mathrm{d}\Omega, \tag{4.22}$$

is equal to the power calculated from equation (4.21). A scaling factor, ξ, is defined such that

$$\xi = \frac{P_{dis}}{\displaystyle\int_{\Omega} \hat{p}_v \, \mathrm{d}\Omega,} \tag{4.23}$$

where $\hat{p}_v$ is the power density obtained from the normalised electric field. All values of $\hat{p}_v$ can then be scaled by this factor,

$$p_v = \xi \hat{p}_v, \tag{4.24}$$

to give the absolute values of the power density. The electric field may also be scaled by

$$\mathbf{E} = \sqrt{\xi}\ \hat{\mathbf{E}}. \tag{4.25}$$

to give actual values of the electric field. This technique has the advantage that the actual power dissipated in the material can be controlled exactly. However, this form of scaling can only take place when lossy materials are present in the cavity. The method uses ρ rather than the wave amplitudes A and B which may improve the accuracy slightly. If the calculated values of A and B are both in error by a constant factor then this will cancel when ρ is formed. This could occur if the integrals I_1 and I_2 which are calculated from the field solution contain such an error.

4.4 Gaussian Pulse Excitation

Gaussian pulse excitation is a commonly used technique for obtaining the response of a system at a range of frequencies from a single time domain calculation. The pulse is modulated with a frequency at the centre of the range of interest. Figure 4.3 shows a typical pulse in both the time and frequency domains. This particular pulse has been modulated at 2.45 GHz and produces a 3 dB bandwidth of approximately 300 MHz. This is significantly larger than the allowable tolerance on the magnetron operating frequency of ±50 MHz.

Application to microwave heating was suggested by Ma *et al.* [1994] who used this method of excitation conjunction with the FDTD technique. For the TDFE method described in this thesis the excitation is applied via a current sheet in the feed waveguide (see Figure 2.3). The system is then time stepped until either the fields have all decayed to zero or a sufficient number of cycles has been reached. For simple, non-resonant systems the fields die away quickly, especially when a lossy material is present. Figure 4.4 show the results of applying a Gaussian pulse excitation to a short circuited waveguide, shown in Figure 4.4(a). The open end of the waveguide was terminated in an ABC (see §2.5.1) and a current sheet placed 20 mm into the guide. Figures 4.4(b)–(d) show the amplitude of the field at a point 40 mm into the guide. When the waveguide is empty, that is with no dielectric present, the trace shows two pulses. The first pulse

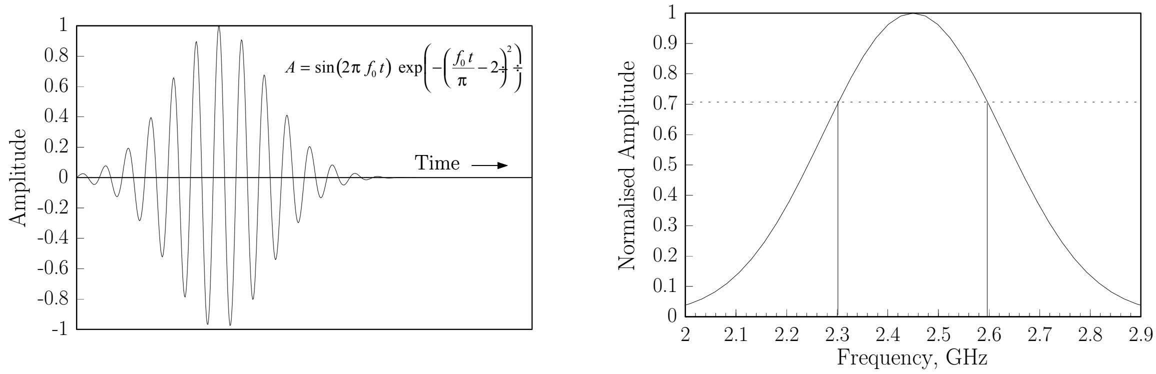

(a) Time Domain

(b) Frequency Domain

Figure 4.3: Typical Gaussian pulse modulated at 2.45 GHz.

is due to the forward travelling wave while the second is the reflection from the end of the guide. When the end of the guide is filled with a glass dielectric the trace shows different characteristics due to the reflections from the air-glass interface. When a wooden dielectric is used which contains substantially more loss, then the oscillations die away more quickly. After 25 or so cycles the fields in the waveguide have decayed practically to zero with all the loadings and the calculation is terminated.

Once the system has settled a discrete Fourier transform (DFT) [Ludeman, 1987] can be taken of the time domain fields in order to obtain the response at individual frequencies. In practice, however, storing all the values of the field at each time step would require an enormous amount of disk space so the DFTs at selected frequencies are accumulated during the time stepping process.

Similarly, it is often required to calculate the reflection coefficient at a range of frequencies instead of storing all the field values required for this, the integrals (4.11) and (4.12) are found at each time step so that only one value per integration plane per time step needs to be stored. A DFT is then performed on these values so that the reflection coefficient can be found at the desired frequency. In order to speed up the calculation a series of weights are determined before the time stepping begins, so that

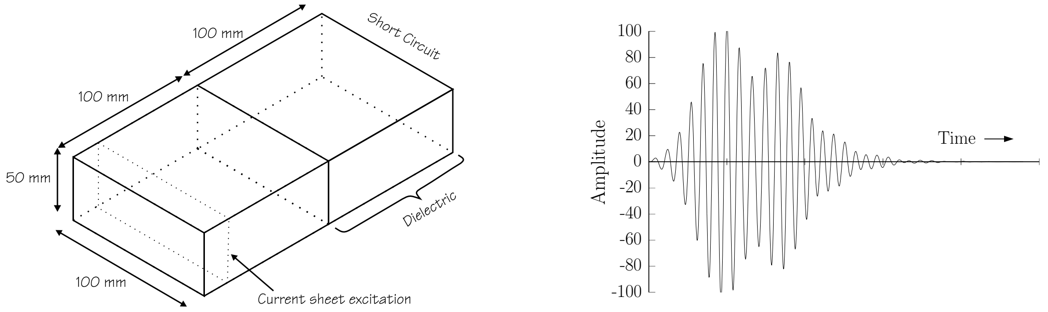

(a) Short Circuit Waveguide

(b) Glass Dielectric ($\epsilon = 4.0 - \jmath 0.001$)

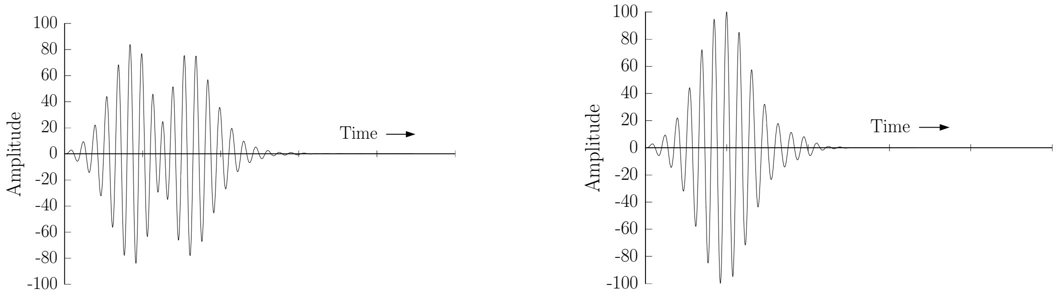

(c) Empty Waveguide

(d) Wood Dielectric ($\epsilon = 2.0 - \jmath 0.5$)

Figure 4.4: Time history of the field at a point inside a waveguide for different terminations and excitation with a Gaussian pulse.

the integrals (4.11) and (4.12) can be calculated from

$$I = \sum_{i=0}^{p} w_i e_i \tag{4.26}$$

where e_i is an edge on the integration plane and w_i is the corresponding weight.

The fields in Figures 4.4 settled very quickly so the calculation could be stopped after only a few cycles, however, this is not always the case. When the system contains resonances with a high Q-factor the fields take considerably longer to settle. Collin [1992] defines a damping factor δ given by,

$$\delta = \frac{\omega}{2Q}. \tag{4.27}$$

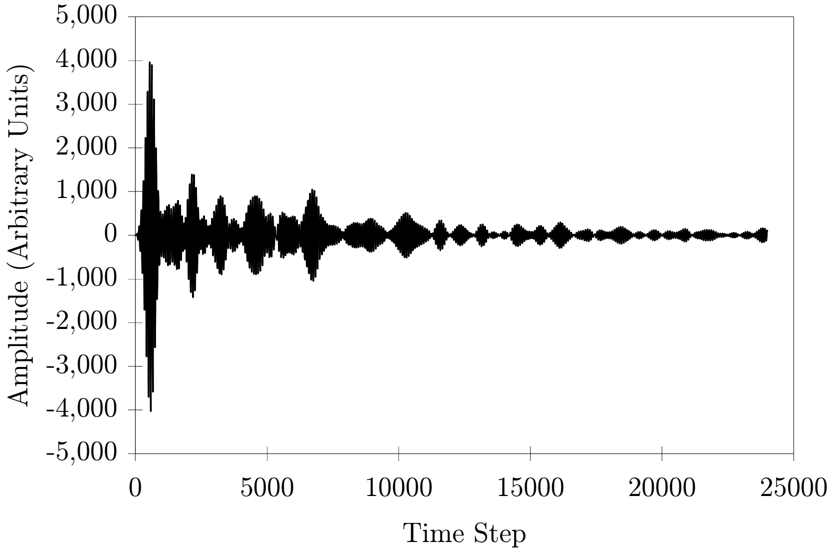

Figure 4.5: Field inside the waveguide feed of a multimode cavity loaded with a plastic slab (80 time steps per cycle, 300 cycles).

This determines the rate of decay of the stored energy, W, in the system after any excitation has been removed,

$$W = W_0 e^{-2\delta t}. \tag{4.28}$$

The inverse dependence of the damping factor on the Q shows that a large number of cycles will be required for the fields to fall to a level which can be taken as zero when modelling high Q-factor systems. The damping factor also determines the time the fields take to build up in the cavity [Collin, 1992]. Therefore, steady state conditions will take a long time to be reached for high Q systems. For the FDTD method Taflove [1988] suggests that a number of cycles equal to the Q-factor are required to achieve a steady state solution.

Figure 4.5 shows the field at a point in the waveguide feed of a multimode cavity loaded with a slab of plastic (see §6.6). The field does not decay to zero in the same way that it did for the waveguide examples above. This has important consequences when carrying out the DFT, which is given by

$$F_i(\omega) = \sum_{n=0}^{p} e_i(n\Delta t)e^{-\jmath\omega n\Delta t} \tag{4.29}$$

where $e_i(n\Delta t)$ is the value of the field on edge i at a time $n\Delta t$. If $e_i(n\Delta t) = 0$ for $n \geq p$ then the summation (4.29) can effectively be carried out to $n = \infty$. The degree to which individual frequencies can be resolved is given by

$$\Delta f = \frac{1}{p\Delta t} = \frac{f_0}{s}, \tag{4.30}$$

where s is the number of cycles at frequency f_0 for which system has been time stepped. It can be seen that when p remains finite there is a limit to the frequency resolution that can be obtained. For example, if we modulate the pulse at 2.45 GHz and time step for 300 cycles then the frequency resolution, Δf, will be 8.16 MHz.

For cavity problems, where the fields take a long time to decay, a large number of cycles are required in order to accurately determine the field at a given frequency. It will be seen in Chapter 6 that for a lightly loaded cavity the system can be very sensitive to small changes in frequency so that it is necessary to be able to discriminate between two frequencies close together. For more heavily loaded cavities the field pattern is much less sensitive to frequency so good frequency resolution is less of a requirement.

4.5 Signal Processing Techniques

The large number of cycles required to achieve good frequency resolution is common to all time domain methods. Recent work by several authors has attempted to reduce this requirement by using signal processing techniques such as linear predictors or system identification methods. Chen *et al.* [1994] claim improvements of up 90% in efficiency when using linear and non-linear predictors with the FDTD method. A number of cycles of the FDTD solution are used to train the predictor which is then used to generate further time domain information. Eswarappa & Hoefer [1994] have used autoregressive and spectral estimation techniques in conjunction with the TLM method to gain a five times speed increase for the analysis of microwave circuits.

Another alternative, the system identification method, has been proposed by Kümpel & Wolff [1994]. The time domain information from a number of cycles is used to determine the coefficients of an equivalent digital filter that is used to represent the system. Once the coefficients have been found the filter can be used to generate further time domain data or alternatively, the frequency response of the system can be determined directly from the coefficients. Other techniques, such as Prony's method [Ko & Mittra, 1991] or the MUSIC algorithm [Bi *et al.*, 1992] may also be used.

The problems given as examples in the above papers tend to be considerably simpler than the case of a large multimode cavity loaded with a lossy dielectric. It remains to be seen whether these techniques may be successfully applied to the problem of microwave heating. For systems that require many time steps at present these methods would appear to offer a considerable saving in computational cost.

Chapter

5

Results: Single Mode Cavities

5.1 Introduction

This chapter presents results for single mode resonant cavities. While the use of these applicators is not as widespread as the multimode type they still play an important role for specialist applications. The field pattern can often be obtained analytically for the isolated cavity, however, when coupled to a waveguide system via an aperture this is not the case. Both cylindrical and rectangular cavities will be considered with comparisons to experimental data being made in order to assess the accuracy of the solution. Two of the problems, the waveguide loaded cavity (§5.2.1) and the cylindrical cavity (§5.3) are TEAM[1] problems. This allows the results obtained here to be compared to solutions by other workers using different methods. Comparison with empirically obtained data often poses certain difficulties due to the inability to accurately model the experimental geometry or to measure accurately material properties. Comparison with other numerical methods therefore allows the method to be tested against a solution for which exactly the same geometry and material properties were used. Ultimately, however, comparison with experiment is necessary to verify the underlying assumptions.

---

[1] TEAM (Testing Electromagnetic Analysis Methods) problems started as a means of aiding in the development and validation of 3D eddy current problems but have now expanded to include other electromagnetic problems [Bossavit & Chaussecourte, 1994].

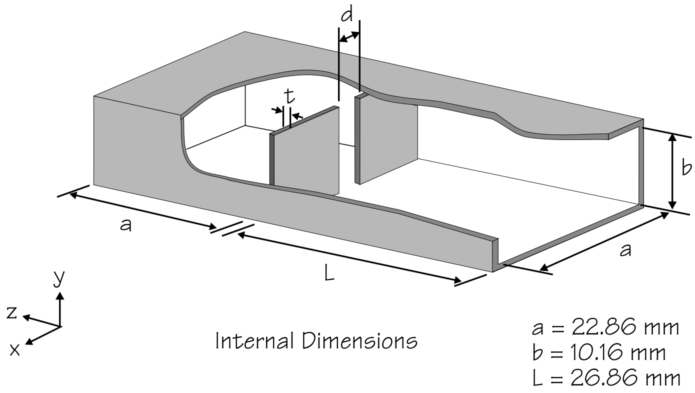

Figure 5.1: Cutaway diagram of waveguide loaded cavity.

5.2 Rectangular Cavities

Two different rectangular cavities were modelled, both being of TE_{101} type. Firstly TEAM problem 19 was studied allowing the method to be compared to another computational method. Then an experimental TE_{101} was modelled so that comparisons with empirical data could be made.

5.2.1 Waveguide Loaded Cavity: TEAM Problem 18

TEAM problem 18 consists of a waveguide containing an iris so that the end section forms a cavity, as shown in Figure 5.1. This is not, strictly speaking, a microwave heating problem. It does not involve lossy dielectrics and the frequency of interest for this problem is 9.15 GHz, which is well above that normally used for heating applications. However, it is a microwave problem for which results have been published so that results can be compared. It is for this reason that it is included in this study. This problem has been solved by Bardi *et al.* [1994b] using an $\mathbf{A} - \psi$ formulation with curvilinear brick elements. Nodal shape functions were used for the scalar field and the longitudinal component of the field while edge based shape functions were used for the transverse component. They only provide graphical results for the particular case of $t = a/32$ and $d = 2a/8$, (c.f. Figure 5.1) so it is this situation that is looked at first.

The mesh used, shown in Figure 5.2, consisted of 13,200 tetrahedral elements which

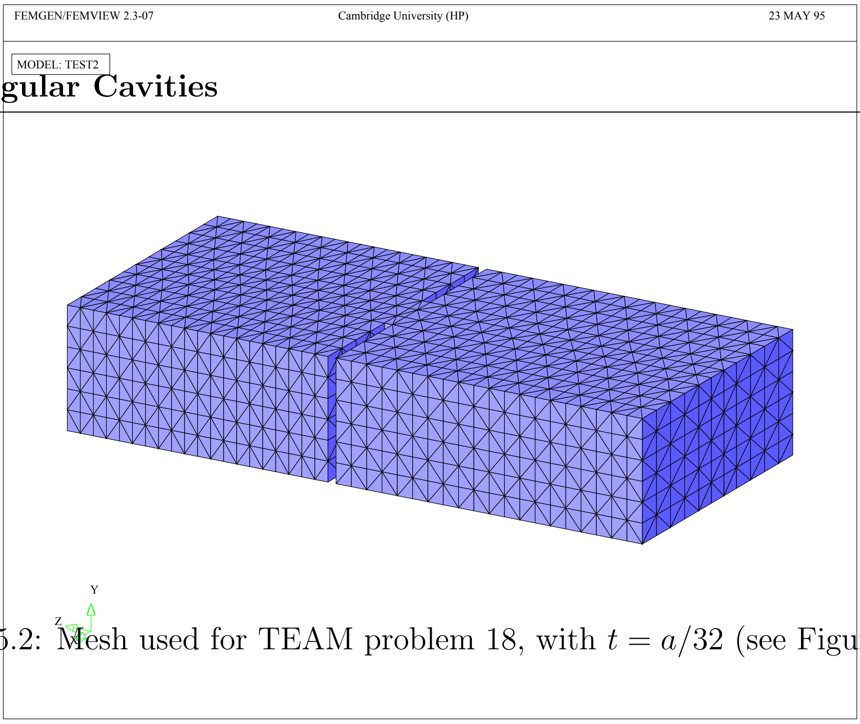

Figure 5.2: Mesh used for TEAM problem 18, with $t = a/32$ (see Figure 5.1).

gave rise to a total of 18,135 edges of which 13,523 were free to vary. The problem was solved in the frequency domain since a good frequency accuracy is required in order to accurately calculate resonant frequency. A TE_{10} mode was prescribed on the open end of the waveguide and the reflection coefficient calculated as from the field solution (§4.2). The SIC-QMR method required approximately 260 iterations to reduce the residual norm to $5 \times 10^{-7} \cdot \|\mathbf{b}\|$, the exact number varying slightly with the excitation frequency. The small number of iterations meant that a single solution at one frequency took only a few minutes to complete. The calculated phase of the reflection coefficient at the input plane is shown in Figure 5.3(a). The calculations were performed for 50 different frequencies and took a total of 109 minutes on a Sparc-10 workstation. This gives an average of 2.18 minutes per frequency. Figure 5.3(a) also shows the results due to Bardi *et al.* [1994b] which show the resonance at a slightly lower frequency. The field distribution is shown in Figure 5.4. The peak magnitude of the field inside the cavity is nearly 30 times the value of the field applied at the input plane.

The magnitude of the reflection coefficient is unity at all frequencies since the system is lossless. The phase, however, varies with frequency undergoing a 360° shift as the resonance is passed. The reflection coefficient is measured at a plane in the waveguide but because of the intrinsic impedance of the waveguide the phase will be dependent upon the position of this plane. Since the position of the input plane is somewhat arbitrary Bardi *et al.* [1994b] suggest the use of a reference plane, see Figure 5.5, which is positioned such that the phase angle of the reflection coefficient, measured at this plane,

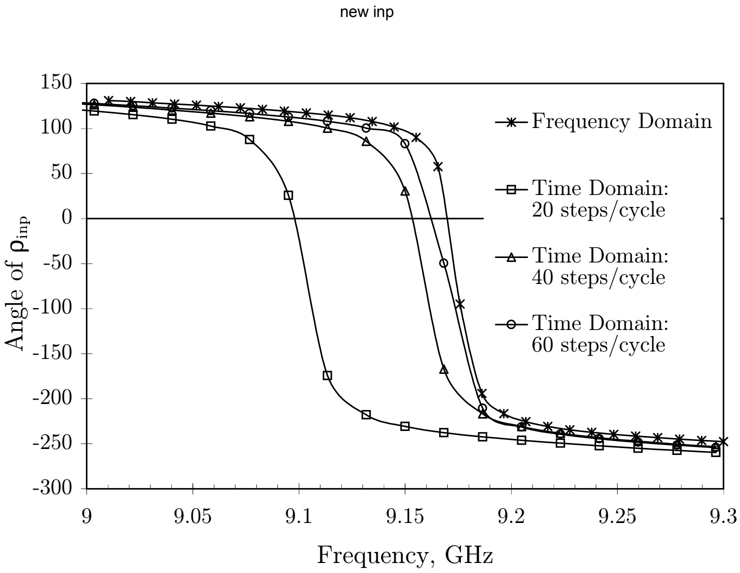

(a) Phase angle at the input plane.

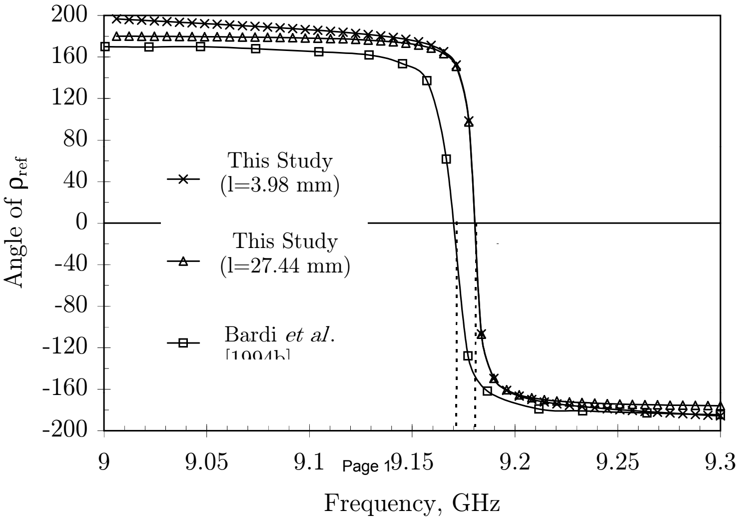

(b) Phase angle at the reference plane.

Figure 5.3: Phase angle of the reflection coefficient for $t = a/32$ and $d = 2a/8$ (see Figure 5.1).

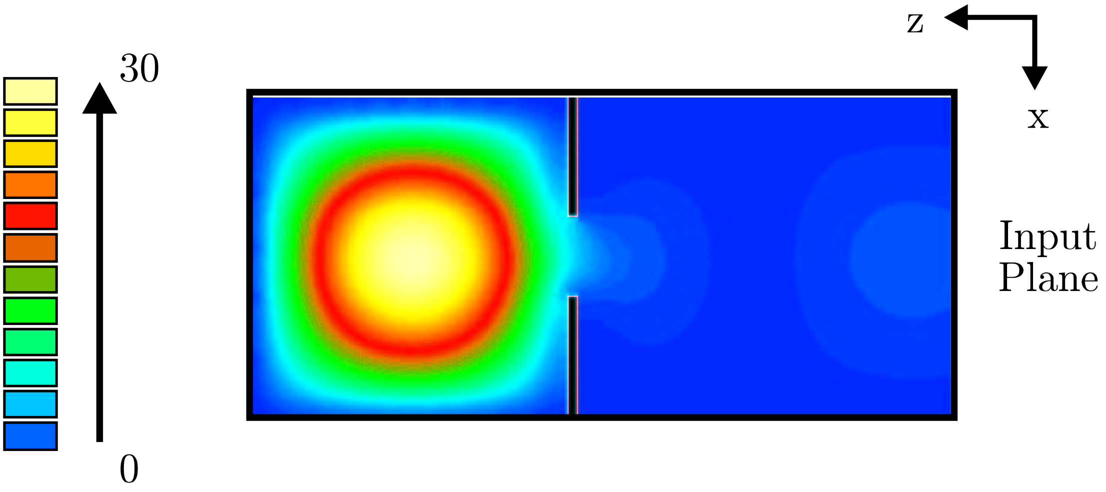

Figure 5.4: Magnitude of the electric field at the resonance, $t = a/32$ and $d = 2a/8$.

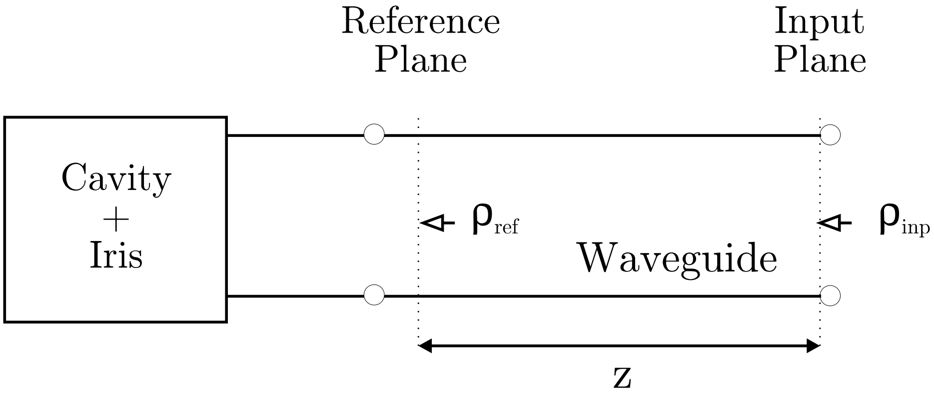

Figure 5.5: One port model of the waveguide and cavity (after Bardi *et al.* [1994b]).

is symmetric about the zero axis. This makes identification of the resonant frequency of the cavity straightforward. Finding the position of this plane is computationally cheap since it does not require any further field calculations. Having found the reflection coefficient at the input plane using the techniques described in Chapter 4 the phase at any plane, z, can be found from

$$\rho_{ref} = \rho_{inp} e^{\jmath 2\beta z}. \tag{5.1}$$

It can be seen from equation (5.1) that there will be series of planes, $\lambda_g/2$ apart for which the reflection coefficient will have zero phase at the resonant frequency of the cavity. Figure 5.3(b) shows the phase of the reflection coefficient at two different planes, one at $z = 3.98$ mm and the other at $z = 27.44$ mm. The latter is actually inside the iris, so it is debatable whether this is a valid choice of plane since it is no longer in the waveguide. Bardi *et al.* do not give the position of the reference plane used for their results, which are also shown in Figure 5.3(a). One can note from the graph that when the plane at 27.44 mm is chosen the frequency response either side of the main resonance is flat. This is to be expected since here only the cavity is affecting the response. At 3.98 mm the phase angle away from the parallel resonance reduces with increasing frequency due to the impedance of the waveguide. The calculated resonant frequency for this problem is 9.180 GHz, whereas Bardi *et al.* [1994b] give 9.1685 GHz, which corresponds to a difference of only 0.125% indicating good agreement between the two methods.

A second problem was modelled, this time with $t = 0$ and $d = 2a/8$, the results are shown in Figure 5.6. Here the resonant frequency was calculated as 9.1734 GHz whereas Bardi *et al.* [1994b] give 9.1519 GHz in this case, a difference of 0.235%. In addition to the frequency domain method this problem was also solved using the time domain technique in order to compare the results and observe the effect of changing the size of the time step. Three different time steps were used, corresponding to 20, 40 and 60 steps per cycle at 9.15 GHz. Figure 5.6 compares the time domain results with the frequency domain results for the phase at both the input plane and the reference plane. The time domain solution was excited by a Gaussian pulse modulated at 9.15 GHz and then run for 500 cycles at this frequency. This allows a frequency resolution of 18.3 MHz, giving 16 different frequencies in the range 9.0 to 9.3 GHz. One of the major

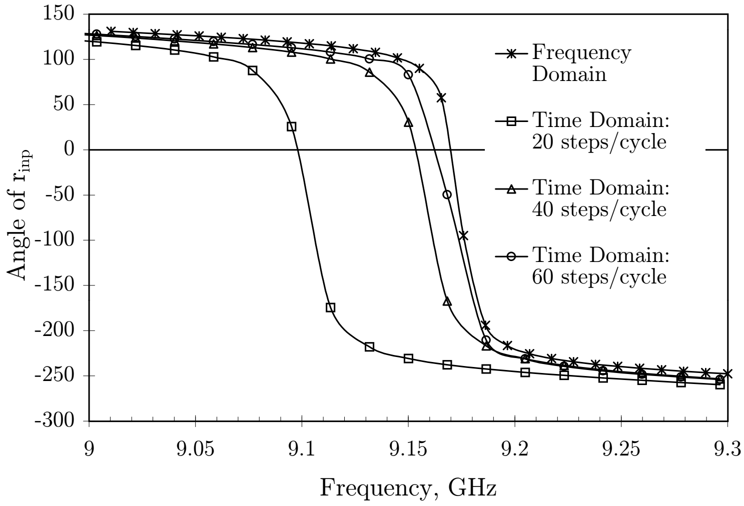

(a) Phase angle at the input plane

new ref

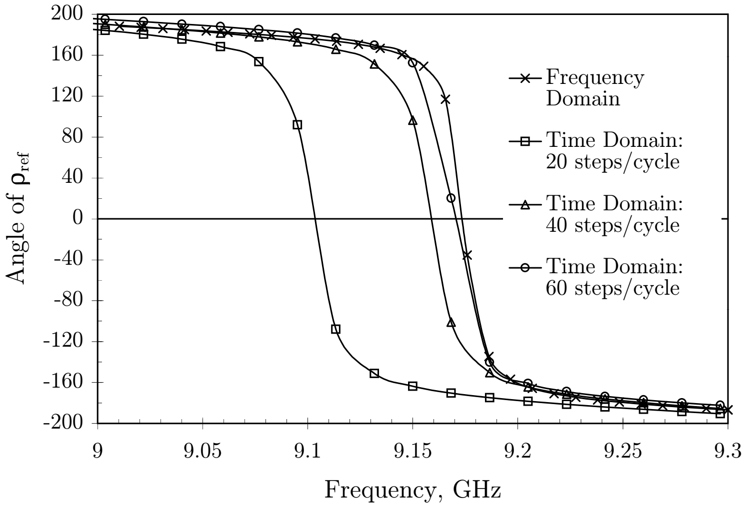

(b) Phase angle at the reference plane

Figure 5.6: Comparison of time domain and frequency domain results for the phase angle of the reflection coefficient for $t = 0$ and $d = 2a/8$ (see Figure 5.1).

problems with solving this type of problem in the time domain is that the fields decay very slowly, requiring a large number of time steps to get good resolution. It is clear from Figure 5.6 that as the time step is reduced the accuracy of the solution is increased, which is to be expected. Table 5.1 shows the discrepancy between the frequency domain solution and the time domain solution, even at 20 time steps per cycle the difference between them is less than one percent. It is interesting to note that as the number of steps per cycle is increased the number of iterations required per time step is reduced significantly. This is due to the reduction in the contribution from the [**S**] matrix to the matrix that requires solution. This has the effect reducing the solution time for the smaller time steps: doubling the steps per cycle does not double the solution time.

Steps / cycle	Iterations per time step	Resonant Frequency	Discrepancy	Solution Time (minutes)
Frequency Domain	—	9.1734	—	109
20	8	9.1035	0.762%	253
40	4	9.1589	0.158%	341
60	3	9.1706	0.031%	445

Table 5.1: Comparison of frequency domain (50 frequencies) and time domain calculations (500 cycles).

5.2.2 EXPERIMENTAL TE_{101} APPLICATOR

This cavity is similar to TEAM problem 18 but the dimensions are such that the resonance occurs near to 2.45 GHz and the cavity is loaded with a lossy dielectric. The applicator, shown in Figure 5.8, was used to obtain empirical values for the reflection coefficient. The cavity had a plunger which can be moved by virtue of being connected to a screw thread. The iris was formed by using two thin metal plates sandwiched between the flange at the open end of the cavity and the adjoining waveguide, with a width of 28.6 mm. The applicator itself had a cross section of 86 × 43 mm, which is a standard waveguide size (WG9A) for this frequency. Two different plunger positions were used, giving cavity length of 75 mm and 80 mm. The cavity was loaded with a

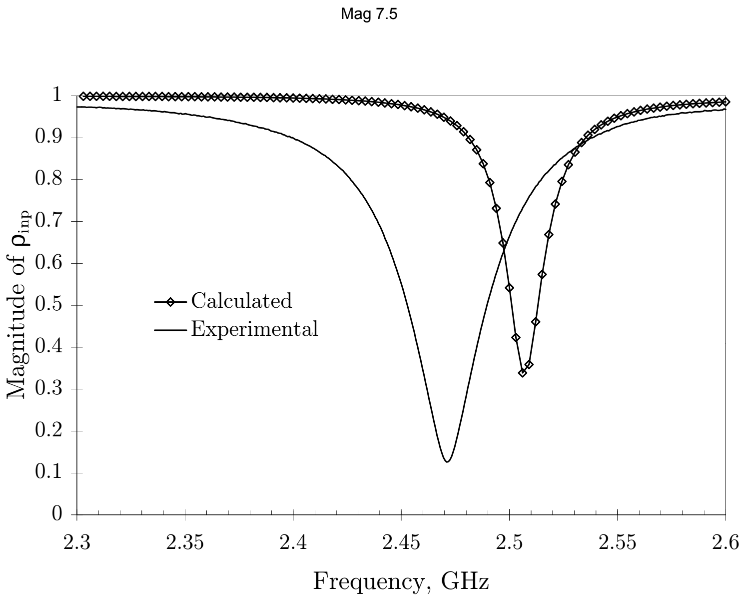

(a) Cavity length 75 mm

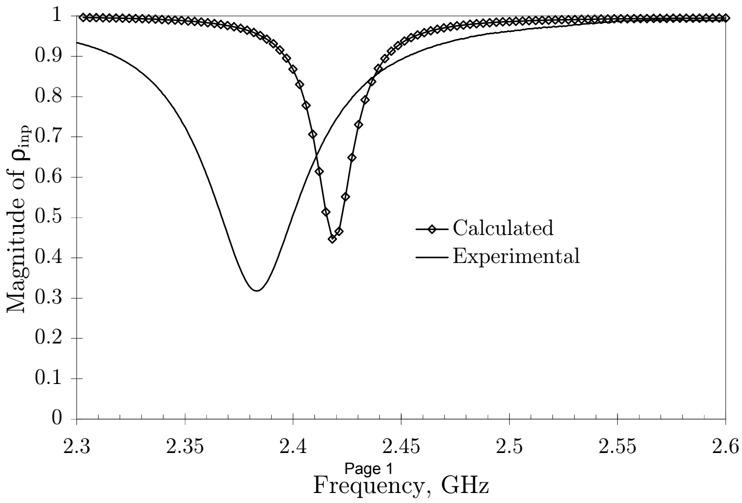

(b) Cavity length 80 mm

Figure 5.7: Magnitude of reflection coefficient for the TE_{101} cavity loaded with a tufnel rod for two different cavity lengths.

Figure 5.8: Photograph of the experimental TE$_{101}$ cavity.

tufnel rod, 10 mm in diameter and placed so that its axis was 50 mm from the aperture. The dielectric properties of the tufnel were measured using a cavity perturbation technique to be $\epsilon_r = 3.275 - \jmath 0.193$.

Figure 5.7 compares the magnitude of the reflection coefficient for the experimental and calculated results for both plunger positions. The calculated values of the resonant frequency are $\sim 1.6\%$ higher than the empirical ones. A possible reason for this discrepancy is the presence of wall losses in the real system. Figure 5.9 shows the magnitude of the reflection coefficient for the empty cavity, where a significant dip is recorded at 2.5 GHz. The finite element method will always give a magnitude of unity for the reflection coefficient of the empty cavity when the walls are assumed to be perfect conductors. The low value of the reflection coefficient at 2.50 GHz would suggest that, for this applicator, the wall losses are significant. The calculated magnitude of the reflection coefficient is significantly higher than the experimental value. This may again be be due to either

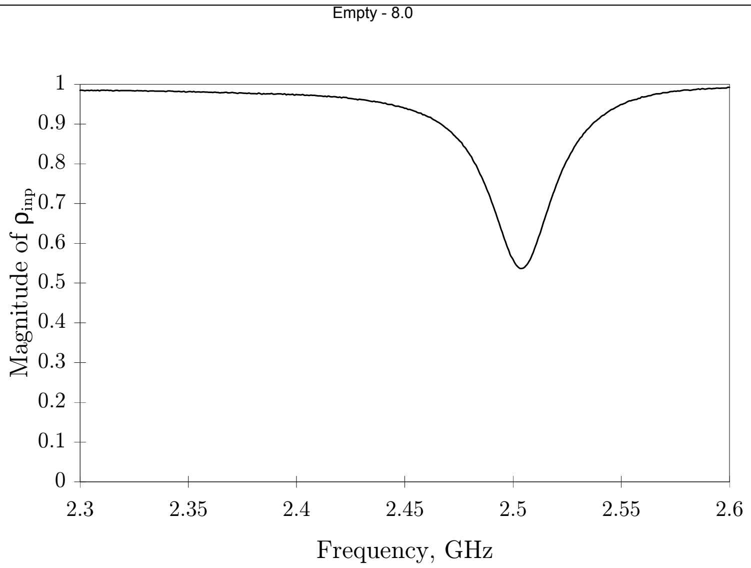

Figure 5.9: Experimental value of the magnitude of the reflection coefficient for the empty TE$_{101}$ cavity with the plunger set so the cavity length was 80 mm.

the wall losses or the inaccurate modelling of the iris. The iris plays a crucial role in determining the impedance match between the feed and the cavity. Small changes in the iris size can have a large effect on the coupling efficiency. This will be seen in the next section when a TM$_{010}$ cavity is studied.

This example clearly shows the sensitivity that a microwave system can have to changes in dimensions. If a good accuracy is required then the system geometry must be modelled accurately. This is one of the great strengths of the finite element method for this type of problem.

5.3 Cylindrical TM$_{010}$ Cavity

Two different TM$_{010}$ cavities have been analysed; the TEAM problem number 19 [Dyczij-Edlinger, 1994] and a cavity for which experimental results could be obtained. This allowed comparisons to be made against both experimental data and published results from different analysis techniques.

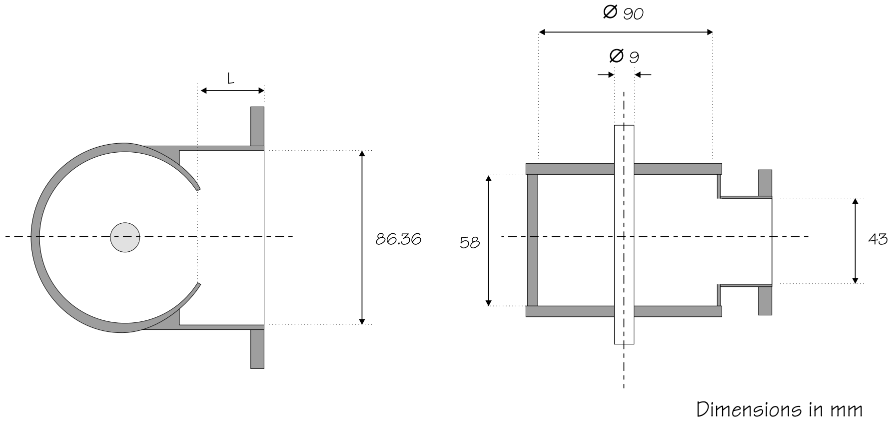

Figure 5.10: Geometry of TEAM problem 19

5.3.1 TM$_{010}$ Cavity: TEAM Problem 19

TEAM problem 19 consists of a cylindrical TM$_{010}$ cavity coupled to a waveguide via an iris. The geometry is shown in figure 5.10. Unlike TEAM problem 18, this is a true microwave heating problem since the cavity is loaded with lossy material. The mesh that was used to model the problem is shown in Figure 5.11, with only one half of the problem being modelled. The mesh consisted of 5,080 prismatic elements producing 12,007 edges of which 8,415 were free to vary. The SIC-QMR took 340 iterations to reduce the residual to 5×10^{-6} of its starting value, corresponding to approximately 1.5 minutes per frequency on a Sparc-10.

The phase angle and magnitude of the reflection coefficient at the input plane for the empty cavity is shown in Figure 5.12 for an iris width of 15 mm. The iris modelled was assumed to be the full height of the waveguide feed. The resonant frequency being calculated as 2.572 GHz. For this iris width Dyczij-Edlinger [1994] calculates the resonant frequency as 2.545 GHz, which is 1.05% lower, however, the wall losses have not been accounted for in the calculation given here whereas Dyczij-Edlinger includes them. The insertion of extra loss into the system can be expected to reduce the resonant frequency of the system slightly. Slight differences between the methods and the meshes used for the calculation may also account for the difference, which is small.

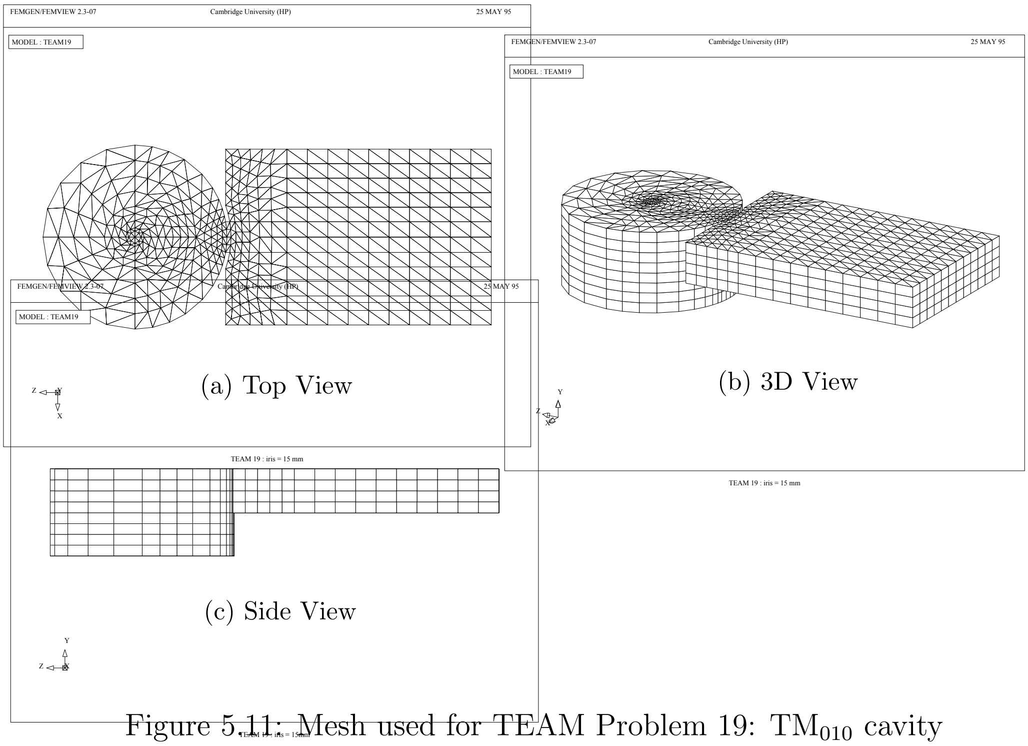

(a) Top View

(b) 3D View

(c) Side View

Figure 5.11: Mesh used for TEAM Problem 19: TM$_{010}$ cavity

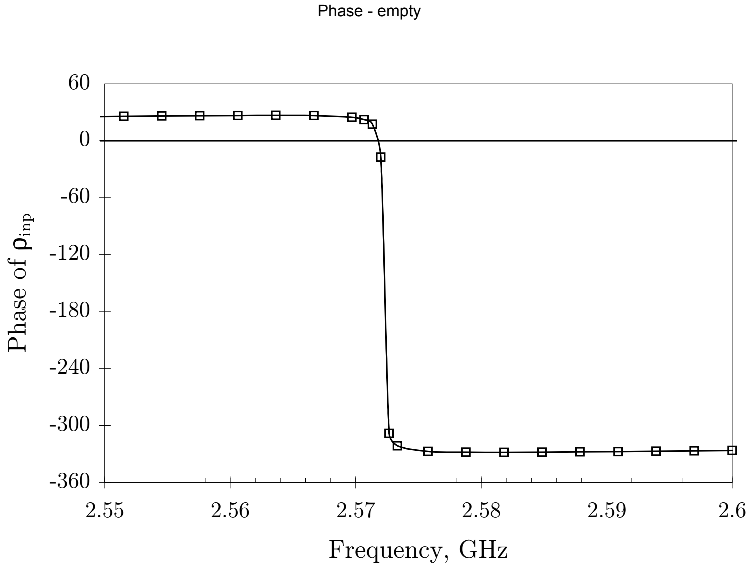

Figure 5.12: Phase angle of reflection coefficient at input plane for the empty TM$_{010}$ cavity (iris = 15 mm).

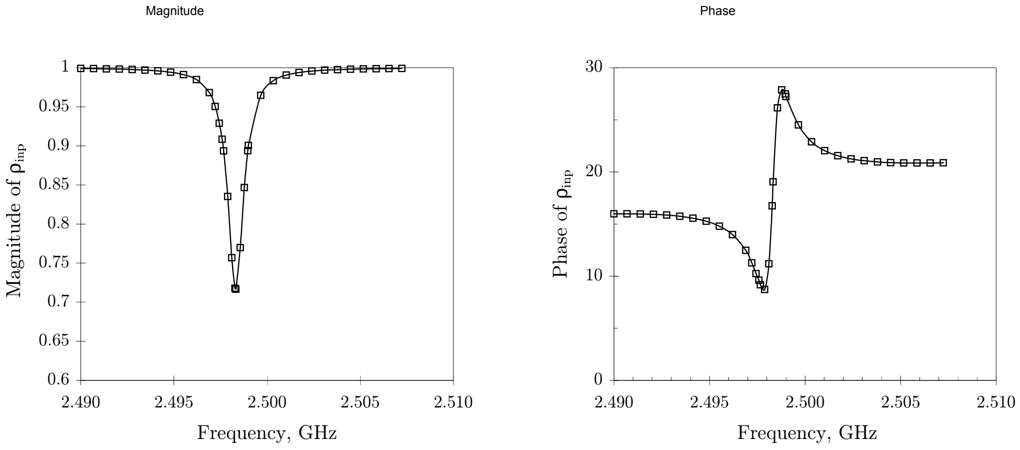

(a) Magnitude of reflection coefficient (b) Phase of reflection coefficient

Figure 5.13: Phase and magnitude of the reflection coefficient of the TM_{010} cavity (iris width = 1 5mm, load = 9 mm diameter plexiglass rod).

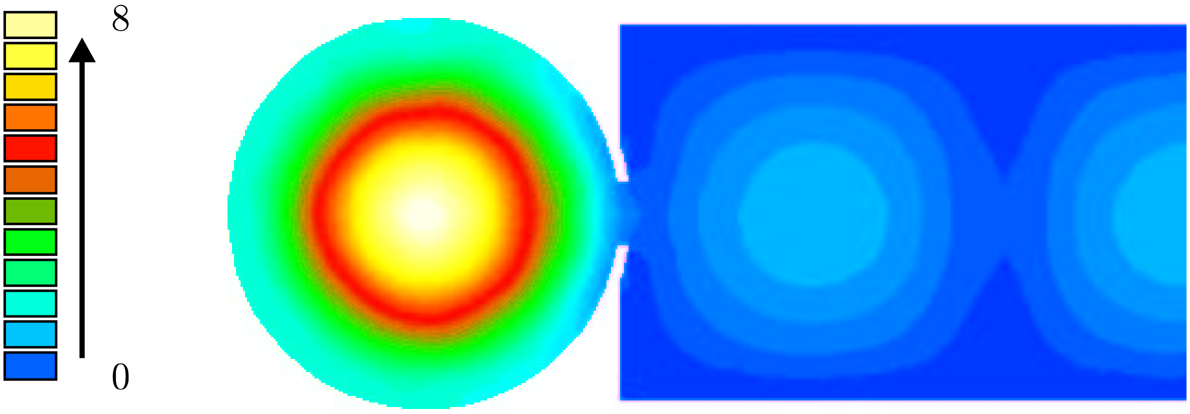

Figure 5.14: Magnitude of the electric field in the TM_{010} cavity near the resonance (iris width = 15 mm, load = 9 mm diameter plexiglass rod).

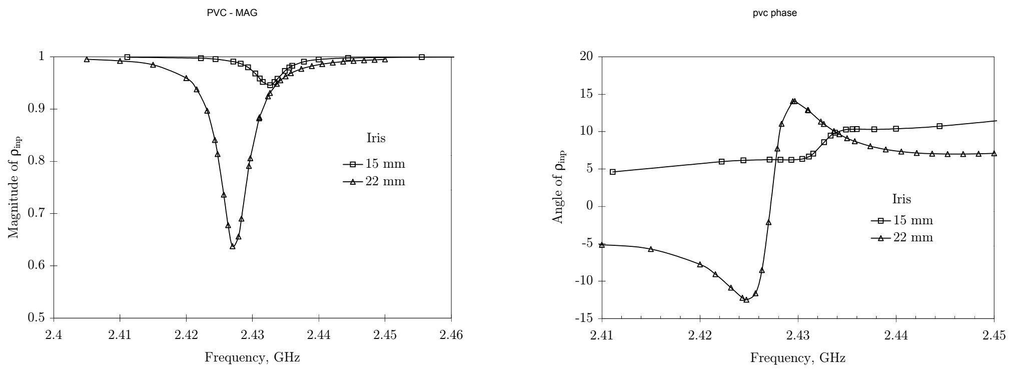

(a) Magnitude of Reflection Coefficient (b) Phase of Reflection Coefficient

Figure 5.15: Phase and magnitude of the reflection coefficient of the TM_{010} cavity for two different iris widths (load = 9 mm diameter PVC rod).

A calculation was then performed for the cavity loaded with a 9 mm diameter plexiglass rod, a problem which has also been solved by Sekkak *et al.* [1994]. The magnitude and phase of the reflection coefficient at the input plane are shown in Figure 5.13 and the electric field distribution at resonance in Figure 5.14. The resonant frequencies calculated by various authors for a 15 mm iris and plexiglass load are tabulated below,

Source	f_r GHz
This study	2.498
Dyczij-Edlinger [1994]	2.465
Sekkak *et al.* [1994]	2.480

The three values are all very close being within 1.4% of each other.

Finally, the cavity was loaded with a PVC rod, also of 9 mm diameter and the reflection coefficient calculated. This time however, two different iris sizes, 15 mm and 22 mm, were used. The results are shown in Figure 5.15. When an iris of 15 mm is used the coupling to the cavity is very poor, giving rise to a large reflection coefficient. The situation improves considerably when an iris width of 22 mm is used, however, the reflection coefficient is still large with 40% of the incident power being reflected. If this cavity was to be used for a real microwave heating problem then further optimisation

Figure 5.16: Photograph of TM_{010} cavity showing connection to the network analyser for measurement of the reflection coefficient.

of the iris width would be required to reduce the amount of reflected power. The larger iris width also has the effect of reducing the resonant frequency slightly.

5.3.2 Experimental TM_{010} Cavity

The dimensions of the cavity are shown in Figure 5.17. This cavity is smaller than that used for the TEAM problem since it has been designed specifically for the heating of liquids which have a strong loading effect on the cavity. The unloaded resonant frequency of the cavity is 3.28 GHz which allows the frequency of the loaded cavity to be close to 2.45 GHz. The waveguide flange of the cavity was connected to a tapered section of waveguide 208 mm long that increased the waveguide cross section to 86 × 43 mm (WG9A). This was so that the cavity could be connected to the rest of the experimental system that uses WG9A. The cavity was meshed using prismatic elements, as shown in Figure 5.18 which enabled the available commercial mesh generation software to be used [Femsys Ltd., 1993]. The electric field solution is shown in Figure 5.19 for excitation at 2.45 GHz and where the cavity is loaded by a quartz glass tube ($\epsilon_r = 4 - \jmath 0.001$) of

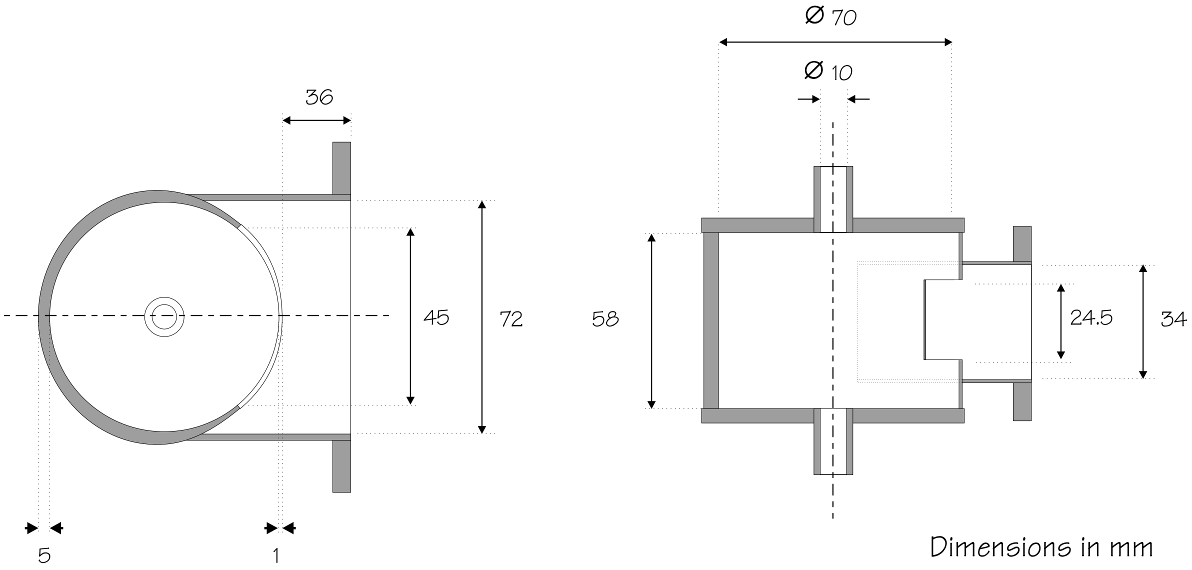

Figure 5.17: Dimensions of TM$_{010}$ cavity

external diameter 6 mm and internal diameter 2 mm containing water ($\epsilon_r = 77 - \jmath 12$). A strong resonance can be observed inside the cavity and a low standing wave ratio in the waveguide feed showing that the energy is being effectively coupled into the water load. Figure 5.20 shows the magnitude of the reflection coefficient at a number of different frequencies and compares the calculated and empirical values. In order to determine the reflection coefficient experimentally the cavity was connected to a Hewlett Packard network analyser, as shown in Figure 5.16. The network analyser was calibrated, using a waveguide calibration kit, so the reference plane was located on the flange of the co-ax to waveguide transition.

The calculated reflection coefficient has a minimum which is both at a lower frequency and lower in magnitude than the experimental system. The resonant frequency is approximately 1.8% too low whereas the percentage difference in the magnitude at resonance is much greater. For the purpose of the calculation it was assumed that water has a relative permittivity of $77 - \jmath 12$, which is that of pure water [Metaxas & Meredith, 1983], whereas ordinary tap water was used for the experiment. The difference in material properties may account for some of the difference. A more probable cause for this discrepancy is the nature of the iris. The cavity used for the experiment had an iris with

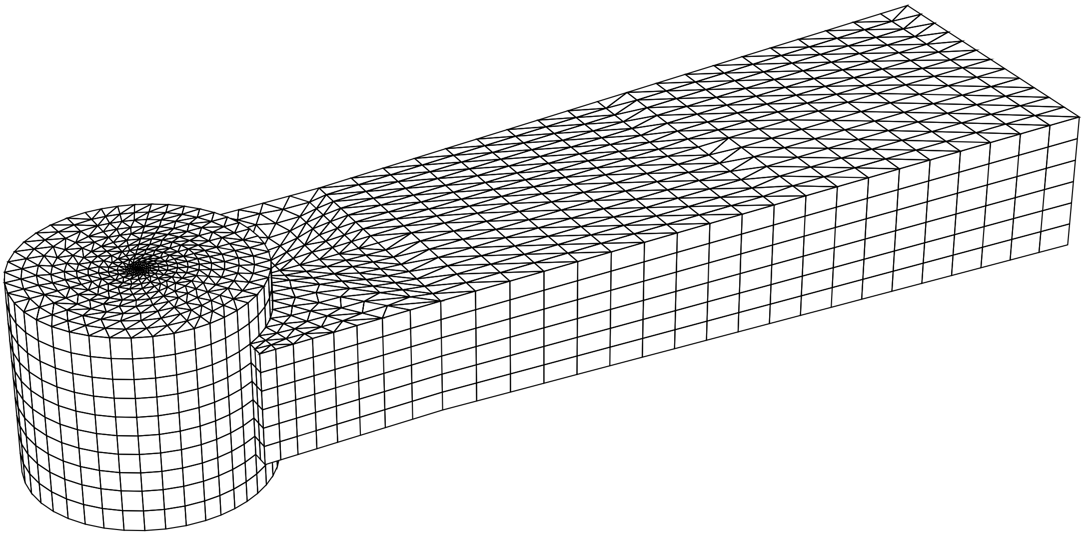

Figure 5.18: Prismatic mesh used for modelling TM_{010} cavity.

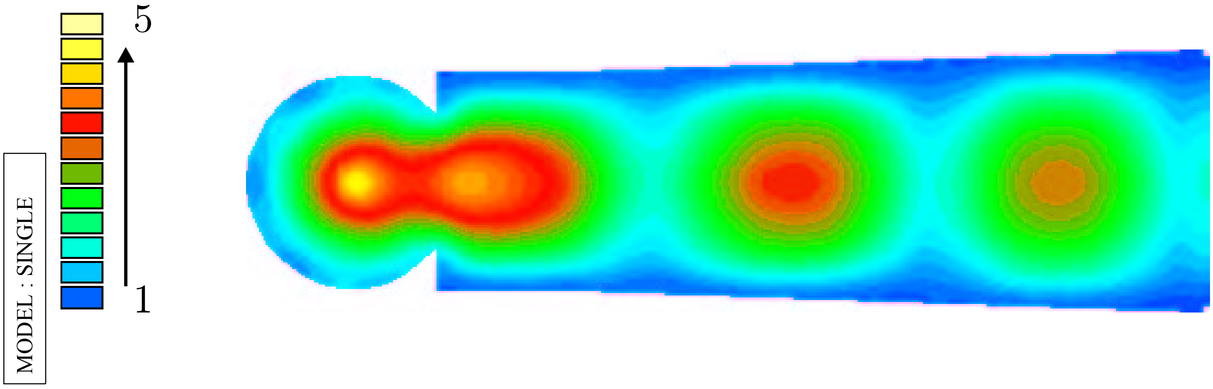

Figure 5.19: Electric field amplitude TM_{010} cavity, normalised so that $|\mathbf{E}| = 1$ at the input plane.

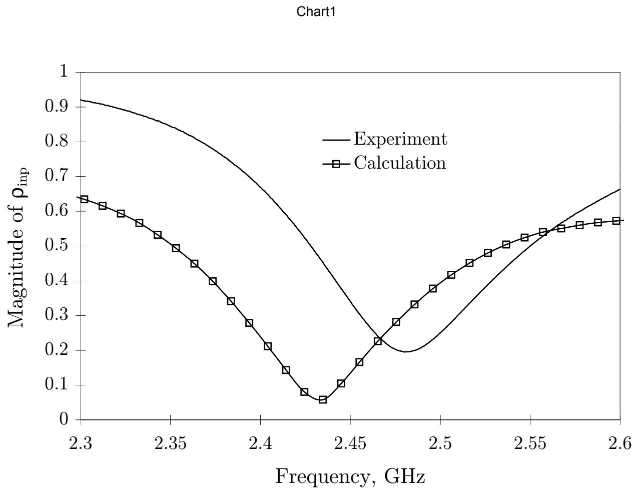

Figure 5.20: Calculated reflection coefficient for TM_{010} cavity loaded with a glass tube containing water

rounded corners whereas the model assumed the iris to be rectangular. This assumption was made because the mesh generation software available was incapable of modelling the curved iris. This may make the iris in the model appear larger, so increasing the loading on the cavity due to the iris and consequently reducing the resonant frequency.

5.4 Conclusions

The results in this chapter have indicated that the resonant frequency of single mode applicators loaded with lossy material can be calculated to within 2% of the true value using the finite element method. For lightly loaded cavities the wall losses may be significant in determining the behaviour of the cavity so for future calculations their inclusion should be seriously considered. The results have also shown that a simple treatment of the iris, with only slight mesh refinement in its vicinity, will produce reasonable results. However, to improve the accuracy it will be necessary to improve the quality of the meshes, particularly around the iris.

It is clear that, for most solutions, the frequency domain method is to be preferred for single mode applicators. The time taken to obtain a solution at a single frequency is considerably less than for the time domain method. In certain situations, where results at a large number of frequencies over a fairly wide range are required, then the time domain method starts to look more attractive. The results do show that as the time step is reduced in size the results for the time domain method approach those of the frequency domain, with a difference of only 0.03% when 60 steps per cycle are used.

Comparisons with other numerical methods show differences as low as 0.125%, whereas comparisons with experiment show errors of 2% for the resonant frequency. This suggests that the numerical method implemented here is performing as well as other methods, however, discrepancies between calculation and experiment still remain.

Chapter

6 Results: Multimode Cavities

6.1 Introduction

The modelling of multimode cavities has many difficulties and it is vital therefore that the solutions obtained from any numerical model are compared to experimental work. It also useful in many cases to compare the results from different numerical techniques since many quantities cannot be measured accurately experimentally. There is a noticeable lack of published results for field patterns in multimode cavities. Several papers have outlined methods that are claimed to be applicable to multimode cavities but either show no results or restrict their work to problems other than multimode systems [de Pourcq, 1984; Sekkak *et al.*, 1994] Of the papers that do publish results they often do not include experimental verification for their work [Jia & Jolly, 1992], so that it is difficult to assess the applicability of their results to real multimode cavities.

This chapter presents some results for multimode cavities produced using the time domain finite element method described in Chapter 2. Wherever possible verification with experimental data has been made. This takes the form of either comparisons between thermal images take of a heated load or the comparison of reflection coefficients measured using the network analyser. Firstly, food-like materials are modelled since they are representative of the major use for microwave heating with multimode applicators. The results for the plastic block demonstrate some of the problems encountered with low loss materials. The results are seen to be very sensitive to small changes in frequency and to changes in the dielectric properties of the material.

6.2 Mesh Generation

The mesh generation for problems in the previous chapter was carried out using a commercial package designed for problems in structural mechanics. This was found to be unsuitable for many multimode cavity problems since it did not allow the localised refinement in regions of a three-dimensional mesh. A very simple mesh generation program was written specifically to overcome this problem. It is, however, restricted to roughly rectangular geometries but allows localised refinement. A brief description is included here since mesh generation is an integral part of the solution of multimode cavity problems using the finite element method.

Quality mesh generation is a fundamental requirement for all finite element methods. One of the major benefits of using the finite element method over simpler finite difference schemes is its ability to use an unstructured mesh. As well as conforming to the geometry, unstructured meshes allow a fine mesh to be used in specified regions. This is particularly important when modelling food like materials, which can have dielectric constants with real parts in the range 30 – 80 at 2.45 GHz giving wavelengths of 1 – 2 cm inside the material. The free space wavelength inside the material being given by

$$\lambda_\epsilon = \frac{\lambda_0}{\sqrt{\epsilon}}. \tag{6.1}$$

The smaller wavelength inside a dielectric material means that variation of the field with distance is greater. In multimode cavities the wavelength gives only a rough guide to the variation of the field since many other factors play an important role in determining the distribution. Furthermore, a large effective conductivity will produce rapid attenuation of the field near the surface of the dielectric. These two factors mean that the mesh discretisation inside the food load needs to be much finer than in the air for a comparable accuracy. If the whole cavity volume is filled using a fine grid the computational cost becomes enormous. The use of an unstructured mesh allows a fine mesh to be used in the dielectric and a coarse mesh elsewhere.

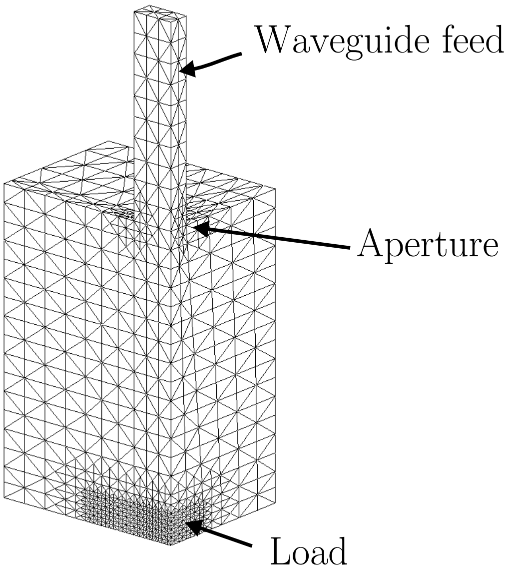

Figure 6.1: Typical mesh for a microwave cavity, one quarter of the cavity is modelled

Many commercial mesh generation programs are available, however, they are often not well suited to producing the three dimensional meshes required for microwave heating problems. Consequently a simple mesh generation program has been written that combines the multi-block [Dawes, 1992] and octree approaches to mesh generation [George, 1991]. The region to be meshed is divided into a number of blocks, a structured mesh is then constructed using an octree method for each block. The structured mesh is then warped to conform the real world geometry of the problem. This method has many disadvantages, being restricted to very simple geometries, however, it is very fast and allows refinement in specified areas and is thus superior to the commercial programs that were available. Figure 6.1 shows a typical mesh that can be generated for a cavity problem containing a dielectric load. For this problem only one quarter of the cavity has been modelled. Note that the mesh has been refined around the load and around the aperture where the waveguide enters the cavity.

The octree mesh generation technique based on the method proposed by Mitchell & Vavasis [1992] was initially used to divide each octree block into tetrahedra. Their method is designed in order to produce a mesh of guaranteed quality, that is the elements so generated have an aspect ratio which is the best possible up to a constant. In order to ensure compatibility between adjacent octree boxes, nodes are inserted on the centre of each face and in the centre of the box. In this way all faces appear identical ensuring compatibility between boxes of the same size. This method does, however, suffer from a major disadvantage. The insertion of these extra nodes means that each octree box is divided into 24 tetrahedra, each of which have an edge equal in length to the size of the box on that face. The method used by Webb [1981] divides a hexahedron into five tetrahedra, the longest edge being equal to $\sqrt{3}$ of the box size. The former method obviously will produce considerably more elements for given edge length. Therefore the mesh will contain more edges and substantially increase the amount of work required to obtain a solution of a given accuracy. Another difficulty with Mitchell & Vavasis's method is that at the boundary between an octree box and four of half its size several poorly shaped elements elements can be produced. The major advantage being ensured compatibility between octree boxes. Webb's scheme was adopted to reduce the number of unknowns for a given discretisation.

Better schemes are available for generating meshes, most notably those based on the Delaunay property. These meshes have particular advantages for edge element based calculations [Haugazeau & Lacoste, 1993]. However, these approaches while being more flexible are considerably more complicated and research into effective algorithms for three dimensional fully automatic mesh generation is continuing. The development of more general tools was considered to be outside the scope of this work.

6.2.1 ADAPTIVE MESHING

When considering the degree of mesh refinement necessary in different regions it was suggested above that a finer mesh is required inside the dielectric. This comes form a consideration of the underlying equations. It is also possible to let the field solution drive the mesh generation: a process known as adaptive mesh refinement. The problem is solved on a coarse mesh to obtain an approximate solution from which the error can be estimated. The mesh is then refined in those areas where the error is deemed to be too high and the process repeated. Since the true solution is unknown the errors can only be estimated, for example Golias *et al.* [1994] use the discontinuity in the flux between two adjacent elements as a measure of the error.

The simple case of a finer mesh being used in regions of higher dielelectric properties, as dictated by equation (6.1), can produce an unnecessarily large number of elements. When the load has a high loss factor then the field in a large portion of it will often be close to zero, with large variations in the field confined to the surface. It is unnecessary therefore to use a fine mesh in the centre of such a load. This is the advantage of using an adaptive technique: the fine areas of mesh can be targeted to where they are most effective.

More work is required in the field of adaptive refinement applied to microwave heating problems as it has the potential for producing significant gains in accuracy while reducing the computational cost of the problem. The time domain method described in this thesis would appear ideally suited to the adaptive process because an approximate solution can be obtained very quickly: it will be unnecessary to allow the field to fully settle before estimating the refinement required.

6.3 Experimental Setup

The experimental apparatus used is as shown in Figure 6.2. A magnetron source operating at a nominal frequency of 2.45 GHz supplies power to the cavity via an iso-circulator. The iso-circulator is used to absorb any reflections from the cavity. The cavity used has internal dimensions of 391 mm × 292 mm × 300 mm and is centrally fed from the top by a waveguide 86 mm × 43 mm in cross section (WG9A). The cavity is of a size comparable with the smaller industrial microwave applicators used for batch processing of loads. To determine the power density distribution within the heated plastic a thermal image of the surface was taken after heating. The heating period was kept short to limit the temperature rise and so prevent a significant change in dielectric properties.

A directional coupler was placed in the waveguide feed to the cavity, as shown in Figure 6.2, the output from which was connected to a Hewlett Packard spectrum analyzer. The coupler is described in Appendix B.

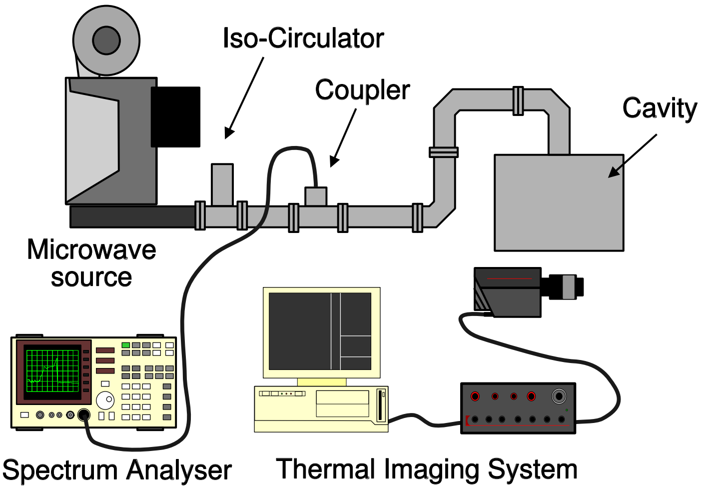

Figure 6.2: Experimental setup

6.3.1 THERMAL IMAGING TECHNIQUE

In order to determine the surface temperature of the heated loads an Agema infra-red camera was used. The cavity set up was such that it was not possible to take an image during the heating process, rather it was necessary to remove the load form the cavity and place it beneath the camera which was mounted on a tripod, as shown in Figure 6.3. The process of transferring the load from the cavity to a position suitable for taking the thermal image was fast, only requiring a few seconds. However, because the image could not be taken in situ, loads with low thermal conductivities were chosen to minimise the temperature changes during transit. The camera was connected directly to a host computer where the images were stored for later retrieval. Since the images were stored in an electronic form it was possible to use the same graphics package for displaying both the thermal images and calculated results. This gives a uniformity of representation that makes comparisons easier.

6.4 Mashed Potato Loaded Cavity

Multimode cavities are often used for the heating or re-heating of food-like materials which generally have both large permittivities and large effective conductivities due to

Figure 6.3: Infra red camera used to obtain the thermal images.

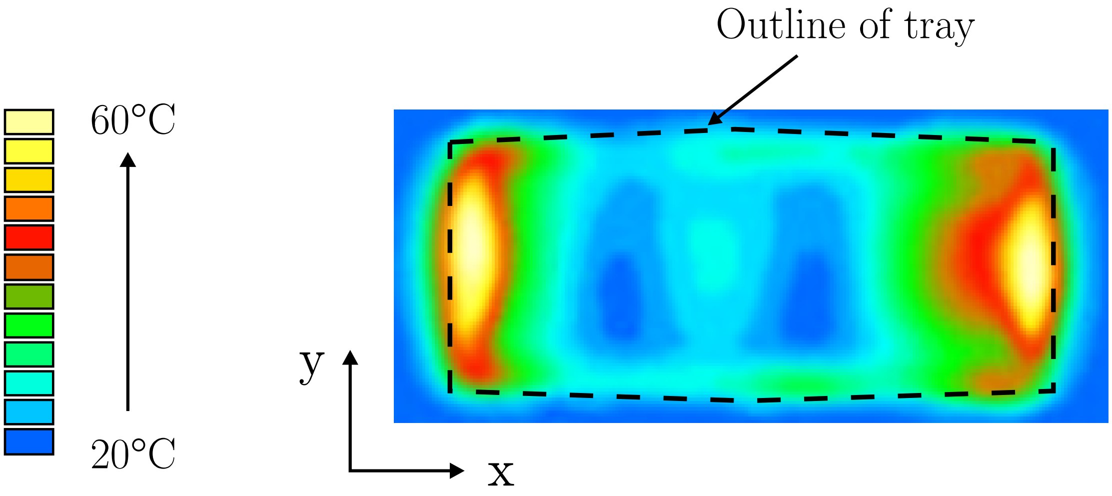

Figure 6.4: Thermal image of upper side of mashed potato after heating for 20 seconds.

a combination of high water content and dissolved salts. The load that was selected had to have certain properties to allow an accurate comparison between experiment and theory. A liquid load, for example water, was ruled out because of the convective mixing that would occur. This would make it impossible to determine the power density distribution from the temperature rise. A material with a low thermal conductivity was also required so that the surface temperature would be representative of the surface power density. The load also had to be a homogeneous material and of a simple geometric shape, in order that geometrical factors could be discounted in any discrepancies between numerical and experimental results. Mashed potato was selected as fitting these requirements. The dielectric properties of several samples were measured using a HP dielectric measurement probe and was found to have an average value of $\epsilon_r = 65 - \jmath 20$ at room temperature. The instant mashed potato used was reconstituted with hot water, thoroughly stirred to ensure its homogeneity, and allowed to cool before being heated in the cavity. The dry form of the potato is a fine powder enabling good homogeneity to be obtained. The potato is liquid enough to easily conform to the boundaries of the container in which it is put and viscous enough to prevent any convective mixing from occurring.

The mashed potato was placed into a thin plastic tray 210 mm long by 90 mm

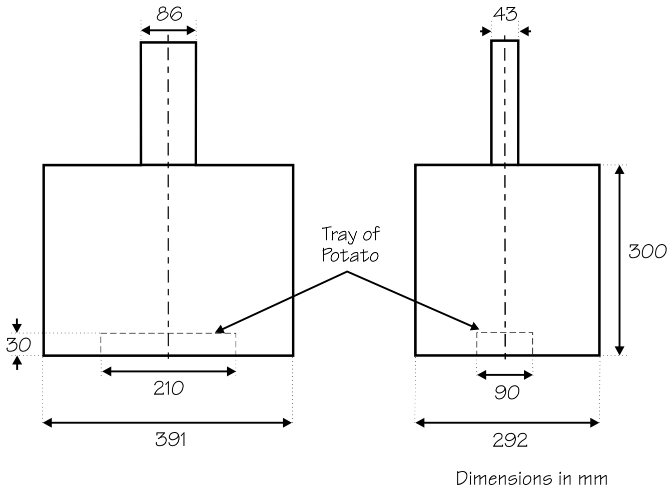

Figure 6.5: Cavity geometry showing the position of mashed potato.

wide to a depth of 30 mm. This was then placed centrally inside the cavity, the longer edge of the tray being aligned with the longer side of the cavity, as shown in in Figure 6.5. The cavity had dimensions of 391 mm × 292 mm × 300 mm and was fed from a waveguide of dimensions 86 mm × 43 mm placed centrally at the top of the cavity with the longer edge of the waveguide aligned with the longer edge of the cavity. The sample was then heated using different powers and for various lengths of time. The heating pattern was found not to change with either heating duration or power. A thermal image of the top surface is shown in Figure 6.4. The power is concentrated at the ends of the tray where very strong heating occurred. Localized boiling occurred here if the heating continued for more than 25 seconds. The power density pattern produced is clearly highly non-uniform.

The loaded cavity was modelled using a mesh which contained 45,364 tetrahedral elements producing 59,111 edges. This mesh produces systems which have 51,388 unknowns in the frequency domain and 51,473 in the time domain. The slight difference is due to the different treatment of the open end of the waveguide feed. Only one quarter of the cavity was modelled, with two planes of symmetry being used [Webb, 1981]. The frequency domain discretisation of this problem was discussed at in Chapter 3 where it was seen that the SIC-QMR algorithm took 67,000 iterations to reduce the residual

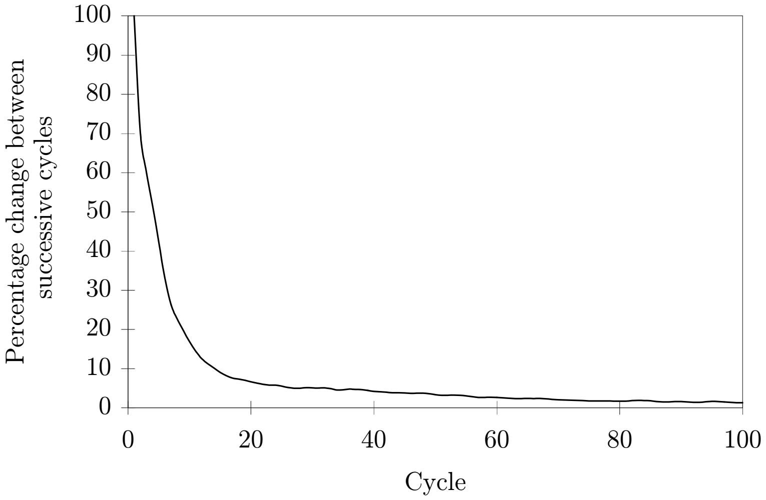

Figure 6.6: Percentage change between successive cycles against cycle number for the time domain solution of the mashed potato loaded cavity.

to 3.7 × 10^{-7} of its original value, taking 43 hours to complete. The problem was also solved in the time domain with the SSOR-CG method requiring 5 iterations per time step to reduce the residual to below 5×10^{-6} when solving equation (2.32). This gave a solution time of 3 hours 40 minutes when the field was time stepped for 100 cycles at 2.45 GHz using 30 time steps per cycle. After 100 cycles the change between successive cycles had fallen to 1.3%. Figure 6.6 shows the percentage change between successive cycles of the field. Initially there is a large change as the fields inside the cavity become established then the change becomes much smaller, however, in order to obtain good accuracy many cycles are needed.

The electric field distribution on a vertical slice through the centre of the cavity is shown in Figure 6.7. The standing wave pattern in the waveguide feed is clearly visible along with a strongly non-uniform distribution inside the cavity. The position of the tray of mashed potato is indicated at the bottom of the cavity and it can be seen that the field inside the potato is very small compared to that inside the cavity. This is to be expected given the high loss factor and high permittivity of the dielectric. The power density at the top of the potato and for a vertical slice through the centre of the tray is

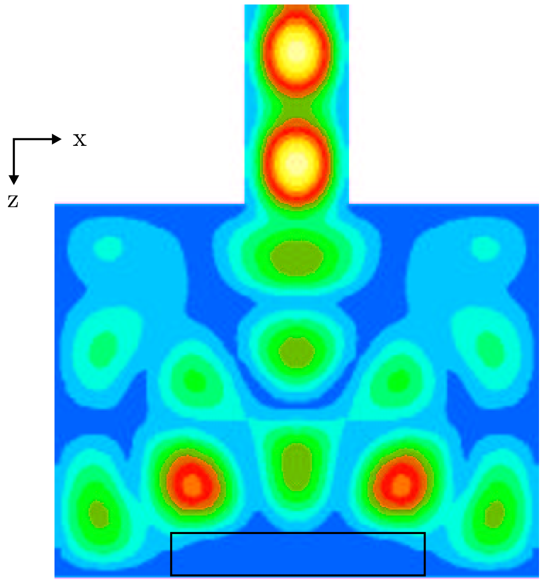

Figure 6.7: Magnitude of the electric field at y=146 mm in the cavity loaded with mashed potato.

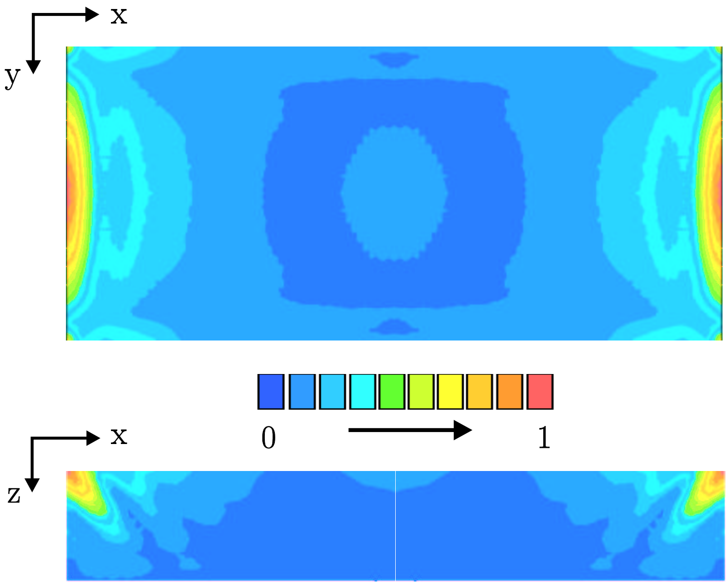

Figure 6.8: Normalised power density on the topside and in the centre of the mashed potato

shown in Figure 6.8.

This example demonstrates the advantage of using the time domain method for multimode cavities containing a lossy dielectric with a high permittivity. A solution was achieved in under 4 hours compared to in excess of 40 hours for the frequency domain method. Each of the time steps requires 2 matrix-vector products to assemble the right hand side of equation (2.32) and then a quantity of forward and backward substitutions equal to the number of iterations plus 2. For the mesh used here only 5 iterations per time step were required so that 2 matrix multiplications and 7 sets of substitutions were needed per time step. Assuming that the matrix multiplications and substitutions require a similar amount of work and that the additional vector operations required at each time step are fast in comparison, this leads to a total cost equivalent of 27,000 matrix-vector multiplications for 100 cycles at 30 steps per cycle. This compares in excess of 67,000 *complex* matrix-vector multiplications required for the frequency domain solution. The complex matrix-vector multiplication requires 4 multiplication and two addition/subtraction operations for each complex multiply. This accounts for the very large difference in solution time, the time domain solution is over 11 times faster, compared to the fairly small difference, only 2.5 times, in the number of matrix vector multiplications. As noted earlier the number of matrix-vector multiplications is generally a better indication of the efficiency of the method than simply the time taken. This is because it is both machine independent and does not depend upon the degree of optimisation obtained in the coding of the algorithm.

Time stepping could not be carried out with the lumped mass matrix (see §2.4.4) for this mesh since negative entries on the diagonal of the $[\mathbf{T}_\epsilon]$ matrix were present in the lumped matrix. This suggests that some elements in the mesh did not conform to Delaunay's empty sphere criteria. It was found impossible, with the mesh generation routines available, to produce a mesh that contained the required localised refinement in the potato and which allowed lumping to take place. If lumping is to be used for this type of problem then better mesh generation algorithms will have to be employed. However, even without the potential reduction in computation time that lumping will provide, the time domain method still shows a considerable improvement over the frequency domain method for this type of problem.

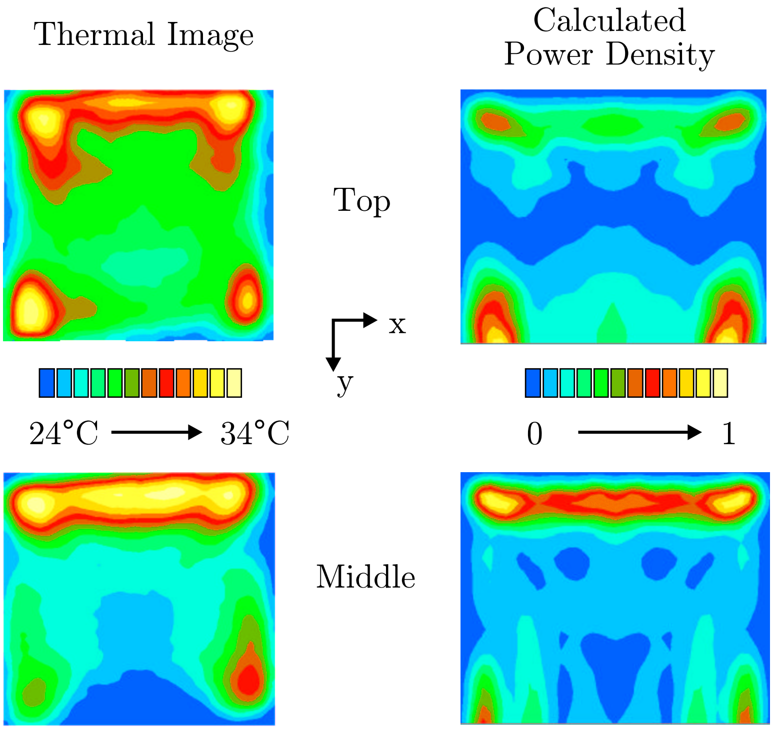

Figure 6.9: Thermal images and normalised power density at two x-y slices through the pastry block.

6.5 Pastry Block

A second food like material was studied to look at the effects of a different geometric configuration. A paste of wheat flour and water was formed into 8 mm thick layers which were then stacked to form a block 110 × 100 × 40 mm. The layers were separated by P.V.D.C. film ("cling" film) so that they could be separated easily after heating. The dielectric properties of the block were measured as $\epsilon_r = 28 - \jmath 8$ using a Hewlett Packard open-ended co-axial probe. The block was placed against the long wall of the cavity such that it was 50 mm from the base of the cavity. The cavity used was the same as that for the mashed potato experiment, shown in Figure 6.5. The mesh used for the numerical calculation consisted of 143,520 tetrahedral elements, a finer mesh being used in and around the pastry block.

The thermal images obtained from the experiment are compared to the finite ele-

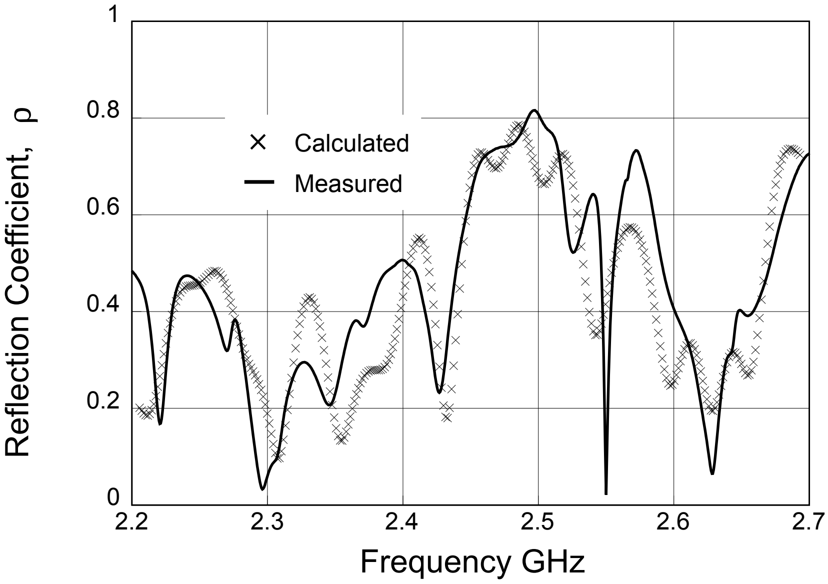

Figure 6.10: Reflection coefficient for the pastry block as a function of frequency.

ment solution in Figure 6.9. There are distinct similarities between the calculated and empirical results, however, the match is not as good as that obtained for the mashed potato. At the top of the block the heating is concentrated in the four corners, which is correctly predicted by the model. The heating along the edge at the front of the block (shown as the top side in Figures 6.9), however, is larger in the experimental result than in the numerical one. Results at 2.4 GHz and 2.5 GHz were also calculated but they showed no significant differences to the results presented in Figure 6.9. The large loading that the pastry block represents will mean that the cavity is likely to have a low Q-factor making it insensitive to small changes in the frequency.

The reflection coefficient was obtained for this problem by connecting the Hewlett Packard network analyser to the cavity, via a calibrated co-axial to waveguide transition. The value obtained in this way is compared to the numerically calculated value in Figure 6.10. The numerical result was obtained by exciting the system with a Gaussian pulse and the taking a FFT of the resulting time domain fields. The two curves in Figure 6.10 show many similar features. The model assumed a perfectly rectangular cavity, whereas in reality the experimental cavity had a number of surface irregularities in the walls of the cavity. These will cause a certain amount of discrepancy between the measured and calculated values of ρ. The wall losses have also not been taken into account in the numerical calculation. It is expected that these losses will be insignificant compared to the losses associated with the pastry block. They do, however, constitute a further difference between the experimental and model systems. This analysis shows the potential of this method for calculating the reflection coefficient and field patterns for multimode cavities loaded with food-like materials.

6.6 Plastic Block

6.6.1 Introduction

The heating of a slab of plastic material inside a multimode cavity has different characteristics to the case of the mashed potato or pastry loaded cavities that were described previously. It highlights many of the problems associated with both microwave heating and the modelling of the heating process. Firstly, the temperature distribution produced inside the block is highly non-uniform. Secondly, since the plastic is a low loss material the resonances inside the cavity are fairly sharp: that is the Q-factor of the cavity is large. This leads to a system that is extremely sensitive to small changes in the frequency, dimensions or material properties. This imposes tough demands on any numerical method.

The cavity used was the same as that for the mashed potato, the dimensions of which are shown in Figure 6.5. The plastic block had dimensions of 200 × 200 × 25 mm and was placed centrally at the base of the cavity.

6.6.2 Experimental Results

The dielectric properties of the plastic were measured using a cavity perturbation technique [de Jongh, 1989]: a piece of the plastic was machined into a 4 mm diameter rod which was then inserted into the centre of a TM_{010} cavity. The relative dielectric properties were determined as $\epsilon_r = 2.5 - \jmath 0.01$ at 2.7 GHz[1]. The block was heated in the

---

[1] This frequency is determined by the size of the cavity which was already constructed and used specifically for cavity pertubation techniques.

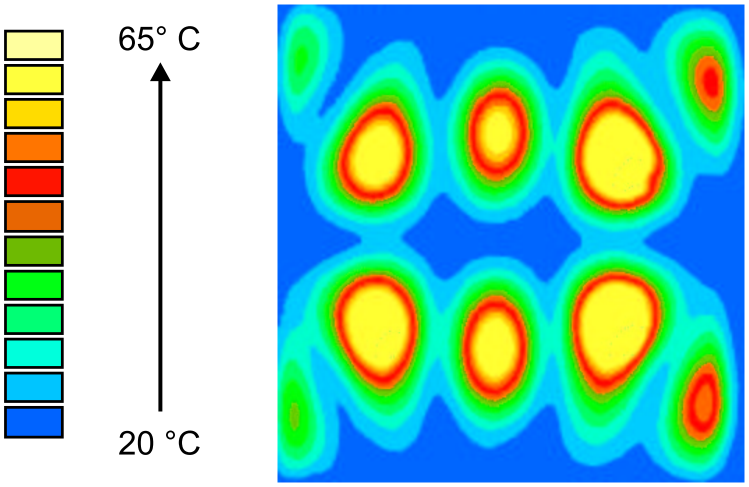

Figure 6.11: Thermal image of the underside of the plastic block after 20 seconds of heating

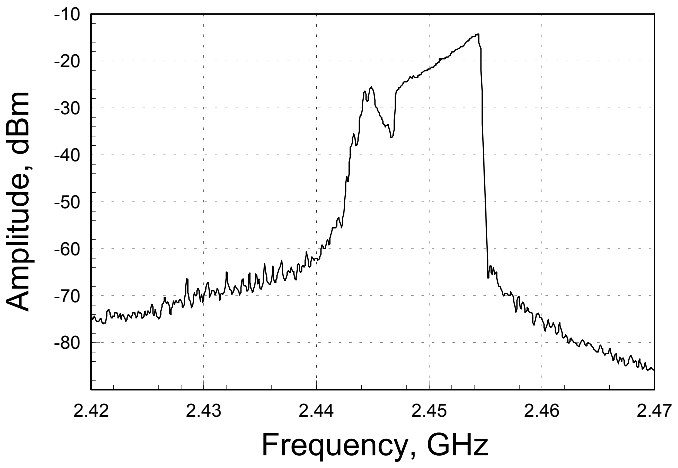

Figure 6.12: Spectrum of the magnetron source used for the experiments

cavity for 20 seconds and then a thermal image, which is shown in Figure 6.11, was taken of the underside of the block. Six hot spots are clearly visible, showing the highly non-uniform heating that can be obtained in multimode cavities.

Since it was expected that the temperature distribution will be sensitive to small changes in frequency the spectrum of the magnetron that supplied the power was measured to determine the actual operating frequency. The spectrum obtained is shown in Figure 6.12 using the coupler described in Appendix B. There is a significant peak at 2.455 GHz with a spectrum of frequencies below this. The lower frequencies have a significantly lower power associated with them. However, it would still be possible for them to affect the field distribution. If one of these frequencies coincides with a mode that possesses a high Q factor, then only a small signal will be required to produce a very large excitation of that mode. It is also to be noted that the dominant frequency is not exactly 2.45 GHz, the nominal operating frequency of the magnetron. The small difference in frequency may be sufficient in some cases to change the relative excitation of the resonant modes, thereby altering the field distribution, which is indeed seen to be the case for the plastic block.

6.6.3 SOLUTION AT A SINGLE FREQUENCY

In order to model the plastic loaded cavity a mesh containing 64,887 edges was used, giving rise to 56,064 unknowns. The mesh had elements of roughly uniform size throughout the whole domain since the plastic has a dielectric constant which is similar to that of air. Unlike the mashed potato problem the matrices arising from the frequency domain discretisation are comparatively easy to solve. This is due in part to the smaller variation in material properties that occurs with the plastic load. A single frequency domain solution for this problem took 4 hours and 10 minutes to complete, requiring 4,784 iterations of the SIC-QMR algorithm to reduce the residual to 5×10^{-7} of its initial value. This is an order of magnitude faster than the mashed potato problem which had a similar number of unknowns. This reinforces the observation made in Chapter 3 that large variations in material properties over the domain have a detrimental effect on the condition number.

The problem was then solved using the time domain method with Gaussian pulse

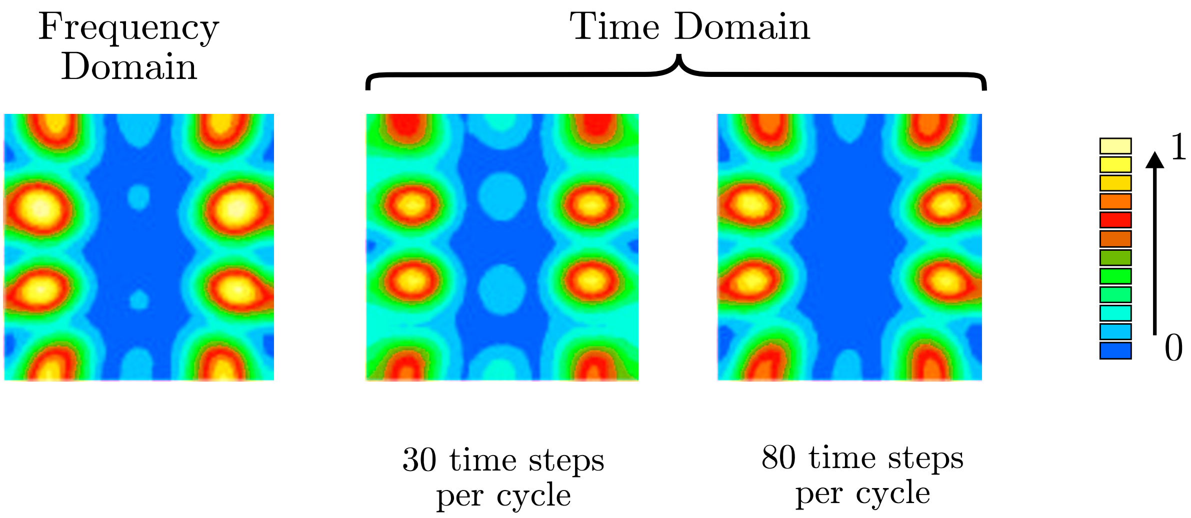

Frequency Domain

Time Domain

30 time steps per cycle

80 time steps per cycle

Figure 6.13: Comparison of four solutions for the normalised power density using the same mesh for the plastic loaded cavity at 2.45 GHz.

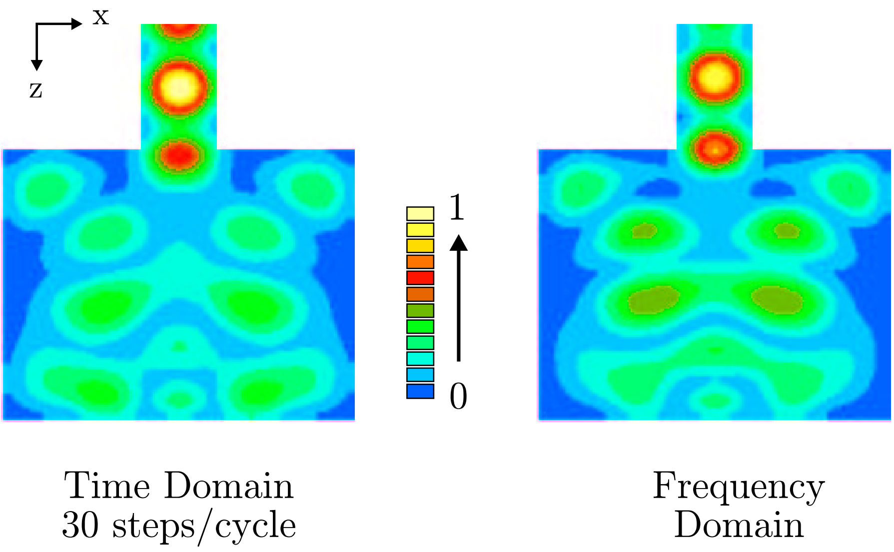

Time Domain 30 steps/cycle

Frequency Domain

Figure 6.14: Comparison of solutions for the normalised electric field magnitude on an x-z plane through the centre of the cavity for excitation at 2.45 GHz.

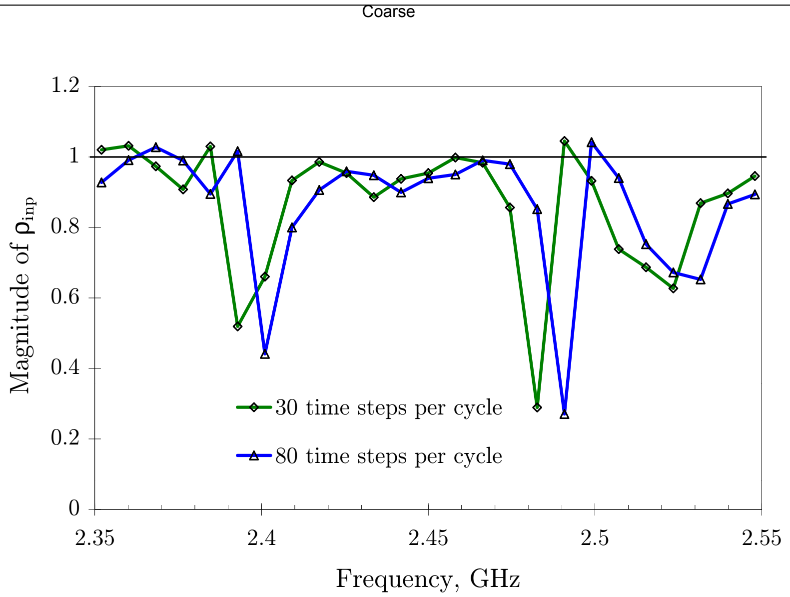

Figure 6.15: Reflection coefficient for two calculated solutions for the plastic loaded cavity.

excitation (see §4.4) modulated at 2.45 GHz with 30 time steps per cycle. The solution was time stepped for 300 cycles taking a total of 9 hours 15 minutes on the Sun Sparc-10 workstation. An average of 4 iterations per time step of the SSOR-CG method being required. A further solution where 80 time steps per cycle were used was also carried out, a calculation which required 23 hours and 40 minutes to complete. Figure 6.13 compares the power density in the plastic block obtained using the time domain and frequency domain methods. The three patterns for the power density are all very similar, the result for the time domain calculation at 80 steps per cycle being slightly closer to the frequency domain one than that for 30 time steps per cycle. The magnitude of the electric field on an x-z plane through the centre of the cavity is shown in Figure 6.14 for both the time domain and frequency domain solutions. The peaks in the centre of the cavity are slightly higher for the frequency domain calculation but otherwise the solutions are identical. These results raise several points.

- The predicted power density patterns at the nominal operating frequency of 2.45 GHz obviously do not match the experimental result. The thermal image in Figure 6.11 has six hot spots in the central region of the block whereas the calculated results show eight peaks, four along each side of the block.

- The results in Figures 6.13 and 6.14 are all very similar. This suggests that the time domain and frequency domain methods give comparable results, that is no accuracy is lost in performing the calculation in the time domain rather than in the frequency domain.
- For a single solution the time domain method appears to be significantly slower than the frequency domain technique when applied to this particular problem.

If we were content to settle for a solution at a single frequency then it would appear that the finite element method produces the wrong result for this problem. This, however, does not do justice to the method: a closer look at the numerical solution is called for. Figure 6.15 show the magnitude of the reflection coefficient against frequency for the two time domain solutions. The two curves show very similar features but are offset in frequency from each other. Increasing the number of time steps per cycle from 30 to 80 has the effect of shifting the curve to the right by approximately 10 MHz or 0.4%. The curves show several sharp dips corresponding to sharp resonances. This confirms the observation made in the introduction that the system is sensitive to small changes in frequency. This also suggests that it would be worthwhile to look at the power density distributions at a range of frequencies other than 2.45 GHz. This is carried out in the next section. It is worth commenting here that at a couple of frequencies the predicted magnitude of the reflection coefficient is greater than unity. In reality this would correspond to more energy being reflected from the cavity than is supplied, which of course is impossible for passive systems. It must be concluded therefore that the values which greater than unity are due to numerical error in the calculation.

6.6.4 MULTIPLE FREQUENCY SOLUTION

It is common in the literature for results to a particular problem to be given only at a single frequency [Jia & Jolly, 1992], however, when low loss materials are being heated the system is very sensitive to small changes in frequency. This makes it essential that solutions at a range of frequencies are calculated and possible variations identified. Figure 6.16 shows the power density distribution at frequencies from 2.44 GHz to 2.50

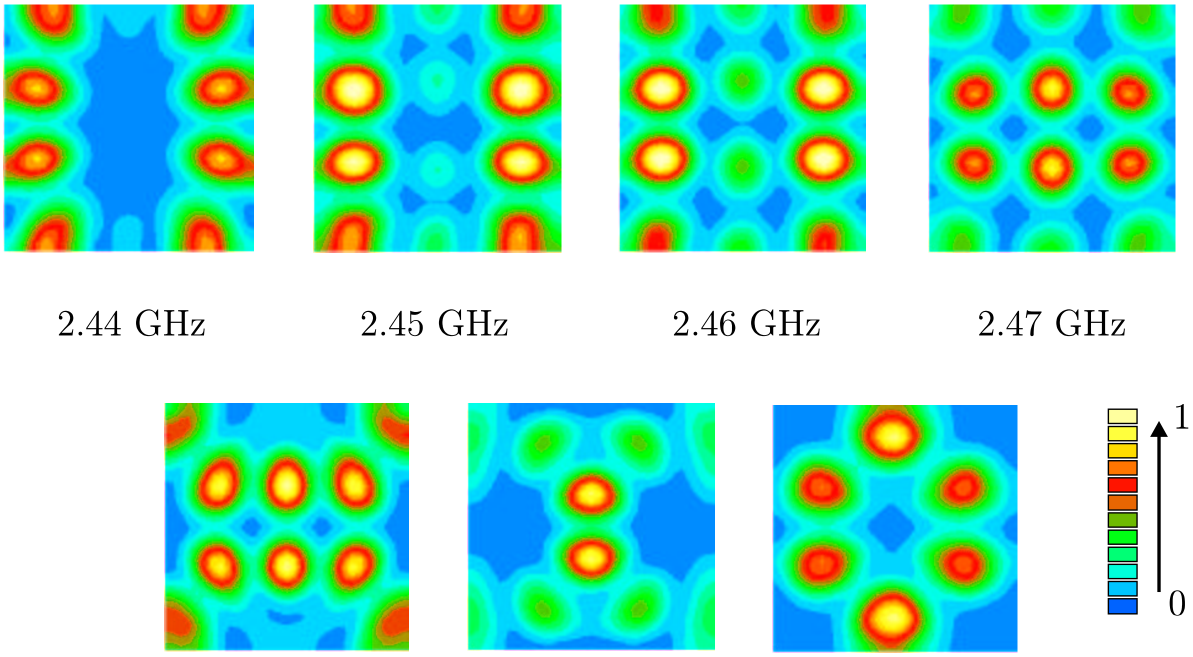

2.44 GHz 2.45 GHz 2.46 GHz 2.47 GHz

2.48 GHz 2.49 GHz 2.50 GHz

Figure 6.16: Numerical results for normalised power density inside plastic block for several frequencies using the coarse mesh and 30 steps per cycle.

GHz calculated using the mesh described above with 30 time steps per cycle. This range corresponds to only a 2.5% variation in frequency yet very distinct changes in field pattern are observed. At 2.47 GHz the distribution corresponds well with the thermal image shown in Figure 6.11.

The patterns shown in Figure 6.16 when coupled with the curves in Figure 6.15 would suggest that there are two different modes which play an important role in determining the power density distribution in the plastic block. Firstly, there is a mode that produces the four strong central peaks present at 2.45 GHz. Secondly, there is a mode at a slightly higher frequency that produces the two central peaks that appear at 2.49 GHz. The thermal image shows that the experimental solution contains a roughly even balance of these two modes, which occurs between 2.47 GHz and 2.48 GHz in the numerical solution. The error in the frequency between numerical and experimental solutions is therefore only 0.8%. The calculation presented here has clearly demonstrated the importance of considering the solution at multiple frequencies when modelling low loss materials. The different distributions obtained in Figure 6.16 shows immediately that the system is sensitive to small changes in frequency.

The result at a given frequency is therefore likely to be effected by small errors in the calculated modes which can then be taken into account when interpreting the results. A solution at a single frequency does not provide this information and is consequentially of very limited value. Solution in the time domain took twice as long as the frequency domain method, however, the frequency domain method only provides information at a single frequency compared to the large frequency range provided by the time domain calculation. The time domain method produced results at seven frequencies in this instance so can effectively be considered to be over three times faster than the frequency domain method for this problem.

Even though the time domain method is faster for multiple frequency solutions than the frequency domain method it still took 9 hours to produce a solution with a mesh containg 56,064 unknowns. Any method therefore, that can speed up this solution should be investigated. Lumping, as described in §2.4.4, has this potential and the application of which is described in the next section. Speeding up the solution also allows a finer mesh to be used without prolonging the solution time, which will hopefully reduce the discrepency between the calculated and empirical results.

6.6.5 Effect of Lumping

Lumping has the potential to significantly reduce the solution time by removing the need for a matrix solution at each time step. The mesh used for the above calculations was based on hexahedra which were approximately cubic, these were subsequently divided into tetrahedra. The elements that were generated were consequently of high quality and lumping could be carried out. Figure 6.17 shows the result for the power density when lumping is used. It is immediately noticed that the solution at 2.45 GHz matches the experimental distribution. Figure 6.18 which shows the magnitude of the reflection coefficient for the lumped and consistent mass matrices against frequency provides an explanation for this similarity: lumping has had the effect of shifting the curve to the left so that the frequency at which the calculated and experimental solutions match is now at 2.45 GHz. This corresponds to lumping having reduced the calculated values of the resonant frequencies by some 40 MHz or 1.6%. In many situations such a small variation will have little effect, however, for this problem, which is sensitive to very small frequency changes, the effect on power density distribution is considerable.

The lumped calculation took 3 hours and 19 minutes to time step for 245 cycles at 80 steps per cycle. The number of time steps per cycle required in order to ensure stability was found empirically. Lumping has had the effect of reducing the solution time by a factor of 2.8, however, a significant shift in resonant frequency is also observed. Since the solution will contain errors, which ever method is used, lumping may provide a very useful means of reducing the calculation time although the interpretation of the results must be carried out even more careful than before.

6.6.6 Solution with a Fine Mesh

In order to investigate the effect of mesh refinement on the solution the problem was solved using a considerably finer mesh. This time the mesh had 204,183 edges of which 184,971 were free to vary. The solution was run both with and without lumping and required 16 hours and 25 hours respectively for the calculation. As previously 80 time steps per cycle were used for the lumped calculation and 30 time steps per cycle with

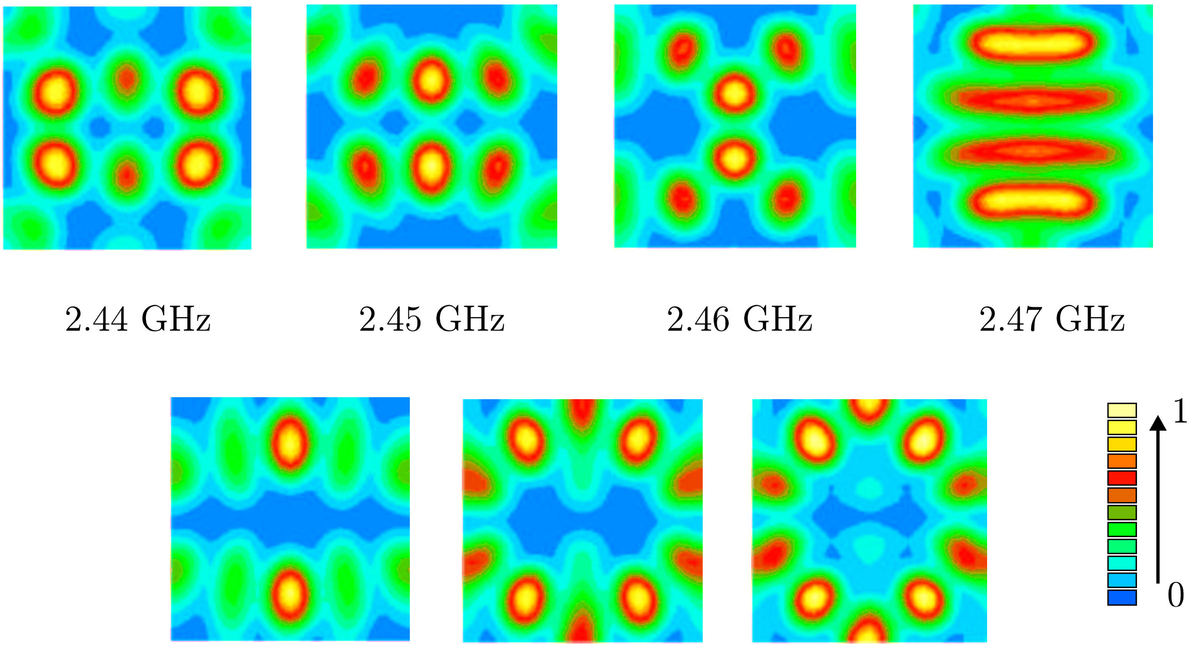

2.44 GHz 2.45 GHz 2.46 GHz 2.47 GHz

2.48 GHz 2.49 GHz 2.50 GHz

Figure 6.17: Numerical results for normalised power density inside plastic block when lumping is used with the coarse mesh.

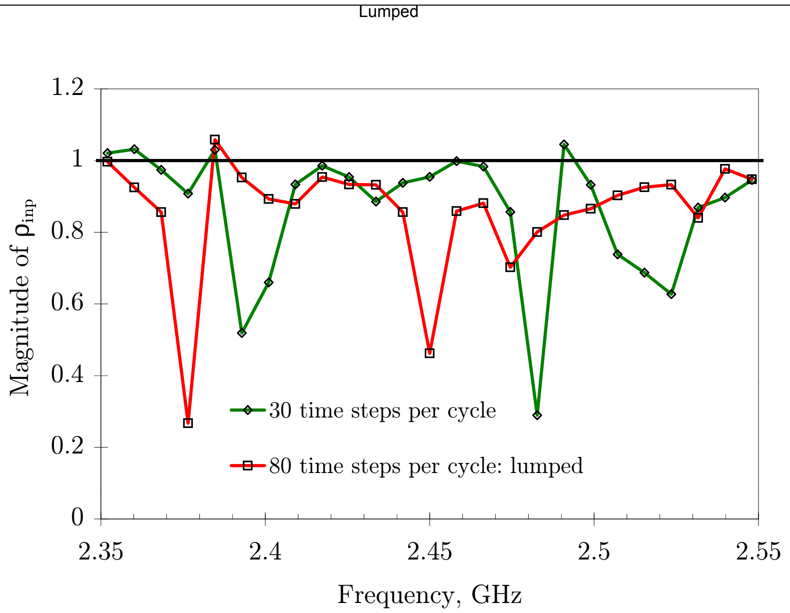

Figure 6.18: Reflection coefficient with and without lumping for the plastic loaded cavity.

the consistent mass matrix. The power density patterns in the block at a number of frequencies are shown in Figure 6.19 and in Figure 6.20 for the lumped solution. Figure 6.21 shows the reflection coefficient for the fine mesh and compares it to that obtained with the coarse mesh without lumping. It can immediately be noted that lumping has much less effect on the solution when a fine mesh is used. The solutions produced on the fine mesh and the coarse mesh when lumping is not used show very good similarities. This suggests that both meshes are sufficiently fine to give a satisfactory approximation to the field: that is the results are not dependent upon the discretisation.

Page 1

6.6.7 Effect of Variation in Dielectric Properties

Figure 6.22 shows the effect on the solution of changing the dielectric properties. The power density distribution is different to all of the previous results. This shows that accurate measurement of the dielectric properties is essential if good comparisons between experiment and simulation are to be carried out.

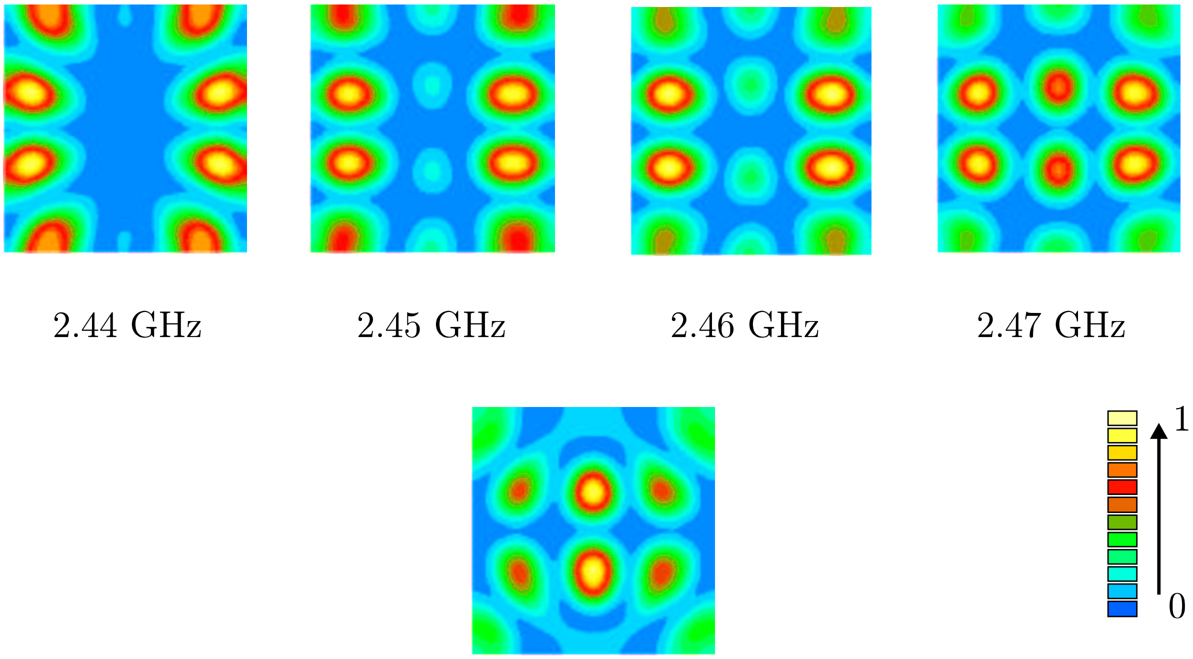

2.44 GHz 2.45 GHz 2.46 GHz 2.47 GHz

2.48 GHz

Figure 6.19: Numerical results for the normalised power density inside plastic block at several frequencies using the fine mesh and 30 time steps per cycle without lumping.

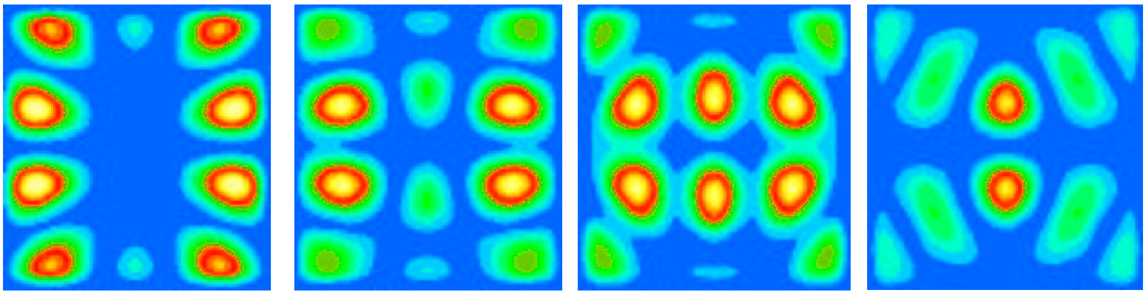

2.44 GHz 2.45 GHz 2.46 GHz 2.475 GHz

Figure 6.20: Numerical results for the normalised power density inside plastic block at several frequencies using the fine mesh with lumping.

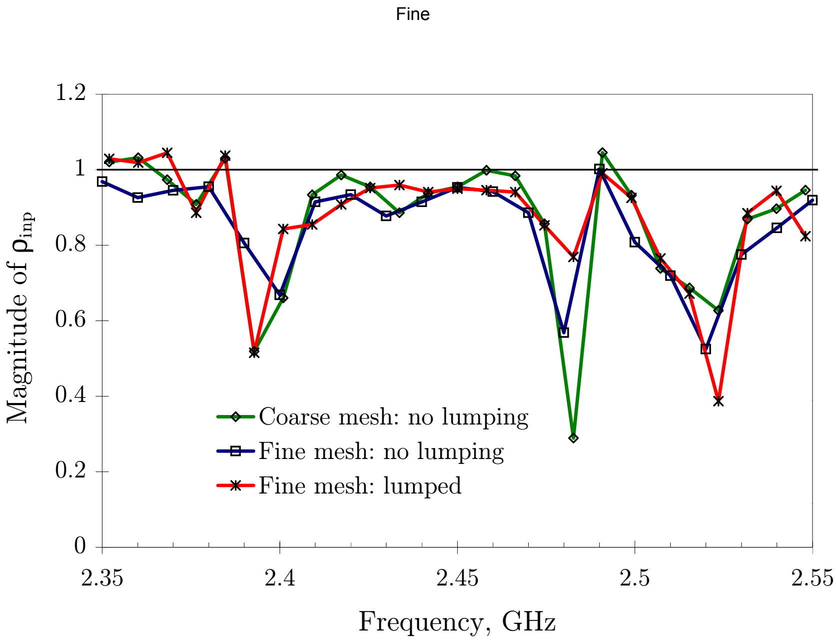

Figure 6.21: Comparison of the reflection coefficient for the coarse mesh at 30 time steps per cycle and the fine mesh with and without lumping.

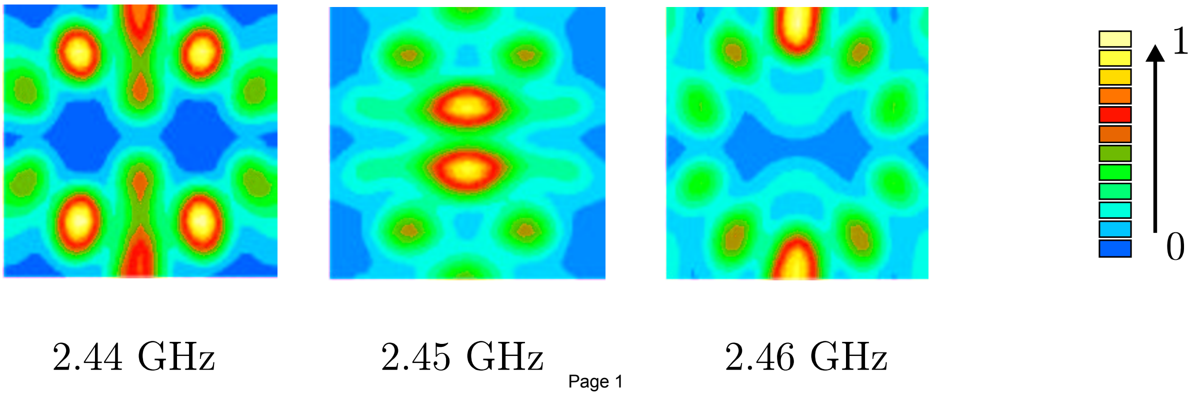
2.44 GHz 2.45 GHz 2.46 GHz

Figure 6.22: Normalised power density in plastic block when $\epsilon_r = 3.0 - \jmath 0.01$ at several frequencies.

6.6.8 Discussion of Results

This result has shown, for low loss materials, that not only is the system very sensitive to small changes in frequency but also that it is vital in any numerical calculation to take full account of this sensitivity. A single frequency domain solution at 2.45 GHz would have given a different answer to the experimental one and no further clue as to why this should be so. Further more, the frequency at which the calculated distribution matches the experimental one of 2.455 GHz is only 0.6% in error for the coarse mesh and 0.2% for the fine mesh when lumping is used. These results also show that it is possible to use the finite element method to produce accurate solutions for low loss materials heated inside multimode cavities although care must be exercised in interpreting these results.

Results with or without lumping on the coarse and fine meshes have all shown similar results but at slightly different frequencies. This would suggest that altering the mesh or using lumping does not change the field distribution of a given mode in a significant manner rather it changes the frequency at which it occurs. The changes in frequency can be very small, less than 2%, yet the resulting changes in field pattern can by very large. If the numerical method was able to calculate the resonant frequencies with no error it may still be difficult to exactly match the experimental solution. The expression given in the introduction for the modes in an empty cavity, equation (1.1), shows that a small change in one of the dimensions can have a corresponding change in the resonant frequency of the mode. The solution for the plastic slab loaded cavity has been shown to be sensitive to changes as small as 0.4%, a change which corresponds to only 1.56 mm on the longest side of the cavity. Unless the cavity has been constructed to a high level of precision, which is unnecessary for normal operation, the the walls of the cavity may vary by this much over the length of the cavity. This shows, once again, that when comparing experimental data to numerical solutions it is essential that the model is an accurate representation of the real system.

6.7 Conclusions

The results given in this chapter can be sumarised as follows,

- For multimode cavities the time domain finite element method described in this thesis is considerably faster for problems involving food-like materials than the more traditional frequency domain method.

- Multimode cavities containing low loss materials can be very sensitive to small changes in frequnecy. The ability of the time domain method, in conjunction with Gaussian pulse excitation to produce solutions at multiple frequencies from a single calculation makes it faster than the frequency domain method. This is true even for systems where a single frequency domain solution is faster than a time domain calculation.

- Cavities with a high Q-factor, which occurs when low loss materials are heated, require field solutions at several frequencies in order to determine the degree of sensitivity of the system to frequency changes. Changes in the mesh can produce small changes in the calculated resonant frequencies, which in turn can have a large effect on the field pattern.

It can also be noted that the solution time for the time domain method scales linearly with increasing refinement: the number of time steps is dependent purely on the desired frequency resolution and the number of iterations per time step is dependent upon the element shapes. This makes it particularly attractive for large problems where the condition number in the frequency domain is prohibitively large.

The comparisons with empirical data have shown that a degree of agreement between experiment and calculation can be achieved. The mashed potato gave an extremely good match whereas the pastry showed certain differences in heating pattern. There remain, however, many difficulties in ensuring that the experimental and model systems are identical. The variations in frequency found between sources and the accurate determination of dielectric properties providing possible sources of discrepancy.

Chapter

7 Solution for Temperature

7.1 Introduction

The purpose of microwave heating systems is to produce a temperature rise in the load. A discussion of microwave heating is therefore incomplete without a consideration of the temperature distribution. The ultimate aim of the simulation must therefore be to predict the temperature rise that will be produced for a given loading in an applicator. The previous chapters have focused solely on the electromagnetic portion of the calculation. For many materials, such as foods and plastics, which have low conductivities the temperature distribution will be very similar to the power density pattern. This is the justification for the comparisons made in Chapters 5 and 6. However, this does not hold for all materials and it is sometimes desirable to calculate actual temperatures.

This chapter addresses the problem of the temperature calculation, which presents many difficulties for loads heated in multimode applicators. The emphasis is placed here on the application of the method to microwave heating problems rather than on the method itself, although a brief description of the formulation is included.

It is often the case that dielectric materials have properties which vary with temperature. Changes in the permittivity effect the power density and therefore the temperature in two ways. Firstly a change in ϵ_e'' will directly change the power density since,

$$p_v = \frac{1}{2}\epsilon_0\epsilon_e''\omega|\mathbf{E}|^2. \tag{7.1}$$

Secondly, changes in both the real and imaginary parts of the permittivity will affect the electric field distribution. For some materials the variation on permittivity may not be significant and have a negligible effect on the field pattern. Other materials, especially ceramics, can show exponential increases in the loss factor with increasing temperature. In these cases the electric field distribution within the applicator will almost certainly vary with the temperature of the load. It is then essential to take into account the variations in properties if the heating process is to be modelled correctly. However, this process is not straight forward when applied to multimode cavities. The last part of this chapter looks at how the electromagnetic and thermal models may be coupled to solve this sort of problem.

7.2 Solution of the Heat Flow Equation

The temperature distribution inside a solid body is governed by the heat flow equation,

$$\rho C_p \frac{\partial T}{\partial t} = \nabla \cdot (\kappa \nabla T) + p_v, \tag{7.2}$$

where p_v is the power per unit volume produced by the microwave heating and ρ is the density of the material, C_p the specific heat capacity and κ the thermal conductivity. This equation is supplemented by the boundary condition,

$$\kappa \frac{\partial T}{\partial \mathbf{n}} + h_e(T - T_{\mathrm{amb}}) + \epsilon \sigma_s (T^4 - T_{\mathrm{amb}}^4) = 0 \qquad \text{on } \Gamma, \tag{7.3}$$

where $\mathbf{n}$ is the normal to the surface Γ and T_{amb} is the ambient temperature of the surroundings. The second term of equation (7.3) represents heat loss from the surface by convection with h_e being the convective heat transfer or film coefficient. For free convection in gases Rogers & Mayhew [1980] suggest that h_e typically lies in the range 0.0005 – 1 $\mathrm{kW/m^2 \cdot K}$, with the actual value being found experimentally. The third term of equation (7.3) represents radiation from the surface where σ_s is the Stefan-Boltzmann constant and ϵ is the emissivity.

Equation (7.2) can be solved using the finite element method [Zienkiewicz, 1977]. We start by applying Galerkin's procedure: premultiplying by a scalar function ϕ and integrating over the volume of the element

$$\int_{\Omega_e} \kappa \phi \nabla^2 T \ \mathrm{d}\Omega_e - \int_{\Omega_e} \rho C_p \phi \frac{\partial T}{\partial t} \ \mathrm{d}\Omega_e = - \int_{\Omega_e} \phi p_v \ \mathrm{d}\Omega_e. \tag{7.4}$$

The material properties are considered to be constant within each element, which enables the κ to be moved outside the gradient. Integrating the first term by parts gives

$$\int_{\Omega_e} \kappa\nabla\phi\cdot\nabla T \ \mathrm{d}\Omega_e + \int_{\Omega_e} \rho C_p \phi \frac{\partial T}{\partial t} \ \mathrm{d}\Omega_e = \int_{\Omega_e} \phi p_v \ \mathrm{d}\Omega_e + \int_{\Gamma_e} \kappa\phi\frac{\partial T}{\partial \mathbf{n}} \ \mathrm{d}\Gamma_e. \tag{7.5}$$

The last term of equation (7.5) represents the heat flow over the surface of an element. At all inter element boundaries this will cancel, the contributions from the two adjacent elements exactly cancelling. Comparison with equation (7.3) shows that we can write,

$$\begin{split}\int_{\Omega_e} \kappa\nabla\phi\cdot\nabla T \ \mathrm{d}\Omega_e + \int_{\Omega_e} \rho C_p \phi \frac{\partial T}{\partial t} \ \mathrm{d}\Omega_e = \\ \int_{\Omega_e} \phi p_v \ \mathrm{d}\Omega_e - \int_{\Gamma_e} h_e\phi(T - T_{\mathrm{amb}}) \ \mathrm{d}\Gamma_e - \sigma_s \int_{\Gamma_e} \epsilon\phi(T^4 - T^4_{\mathrm{amb}}) \ \mathrm{d}\Gamma_e.\end{split} \tag{7.6}$$

The temperature, T, and ϕ are replaced, as normal by,

$$T = \sum_{i=0}^{N} \lambda_i T_i \qquad \phi = \sum_{j=0}^{N} \lambda_j \qquad q_v = \sum_{k=0}^{N} \lambda_k q_{v_k}. \tag{7.7}$$

where λ_i are the shape functions within the element and q_{v_k} is the value of the power density at node k. Substituting these into equation (7.5) leads to a matrix equation,

$$[\mathbf{K}]\mathbf{T} + [\mathbf{M}]\frac{\partial \mathbf{T}}{\partial t} = [\mathbf{G}]\mathbf{Q} - [\mathbf{H}]\mathbf{T} + [\mathbf{H}]\mathbf{T}_{\mathrm{amb}} - [\mathbf{R}]\mathbf{T}^4 + [\mathbf{R}]\mathbf{T}^4_{\mathrm{amb}}, \tag{7.8}$$

where the individual element matrices are given by,

$$\begin{aligned}
[\mathbf{K}]^e_{i,j} &= \kappa \int_{\Omega_e} \nabla\lambda_i\cdot\nabla\lambda_j \, \mathrm{d}\Omega_e, \\
[\mathbf{M}]^e_{i,j} &= \rho C_p \int_{\Omega_e} \lambda_i\lambda_j \, \mathrm{d}\Omega_e, \\
[\mathbf{G}]^e_{i,j} &= \int_{\Omega_e} \lambda_i\lambda_j \, \mathrm{d}\Omega_e, \\
[\mathbf{H}]^e_{i,j} &= h_e \int_{\Gamma_e} \lambda_i\lambda_j \, \mathrm{d}\Gamma_e, \\
[\mathbf{R}]^e_{i,j} &= \sigma_s\epsilon \int_{\Gamma_e} \lambda_i\lambda_j \, \mathrm{d}\Gamma_e,
\end{aligned} \tag{7.9}$$

In the interior of the material the contributions to $[\mathbf{H}]$ and $[\mathbf{R}]$ from adjacent elements will cancel so they are only non-zero for element faces that are on the surface of the material.

To discretise the temporal derivatives in equations (7.8) the θ–method has been used [Wood, 1990],

$$\{[\mathbf{M}] + \theta\Delta t\,([\mathbf{K}] + [\mathbf{H}])\}\,\mathbf{T}_{k+1} = \{[\mathbf{M}] - (1-\theta)\Delta t\,([\mathbf{K}] + [\mathbf{H}])\}\,\mathbf{T}_k$$
$$+\Delta t\left\{\theta[\mathbf{G}]\mathbf{Q}_{k+1} + (1-\theta)[\mathbf{G}]\mathbf{Q}_k - [\mathbf{R}]\mathbf{T}_k^4 + [\mathbf{H}]\mathbf{T}_{\text{amb}} + [\mathbf{R}]\mathbf{T}_{\text{amb}}^4\right\}. \tag{7.10}$$

When $\theta = 0.5$, Crank-Nicolson centred differences are used [Crank & Nicolson, 1947], with $\theta = 0$ forward differences and $\theta = 1$, backward differences are used in equation (7.10). However, forward differences are always used for the radiation term. This is because the inclusion of a $\mathbf{T}_{k+1}^4$ term on the left hand side of equation (7.10) would make solution considerably harder! With $\theta = 0.5$ the method is implicit, has an accuracy of $O(\Delta t^2)$ and is unconditionally stable.

7.3 Temperature Distribution in Mashed Potato Load

The heat flow equation was solved for the mashed potato loaded cavity problem described in Chapter 6. This example serves to demonstrate some of the difficulties involved in applying the heat flow equation to microwave heating problems. Firstly, accurate values of the thermal properties were not available. The values that were used for the calculation are given by Singh & Heldman [1984]; the specific heat for potato as 3.517 kJ/kg · K and the thermal conductivity as 0.554 W/m · K. The mashed potato was formed formed by mixing 120 g of dry powdered instant potato with 600 ml of water, which gives the mashed potato a water content of around 83%. This is slightly higher than the value quoted by Singh & Heldman of 75%. This suggests the value of specific heat capacity that was used used might be slightly too low. The density of the mashed potato was taken as 948 kg/m^3. Since a value of h_e was unavailable several values were used so that the effects of adjusting the heat loss from the surface could be observed.

Figure 7.1 shows temperatures calculated from the solution of equation (7.2) for two values of the convective heat transfer coefficient. The power density distribution was taken from the field solution given in Chapter 6. The power supplied to the cavity was taken as 600 Watts, so with the calculated reflection coefficient of 0.38 the power dissipated in the potato was 513 Watts. The temperature solution was time stepped

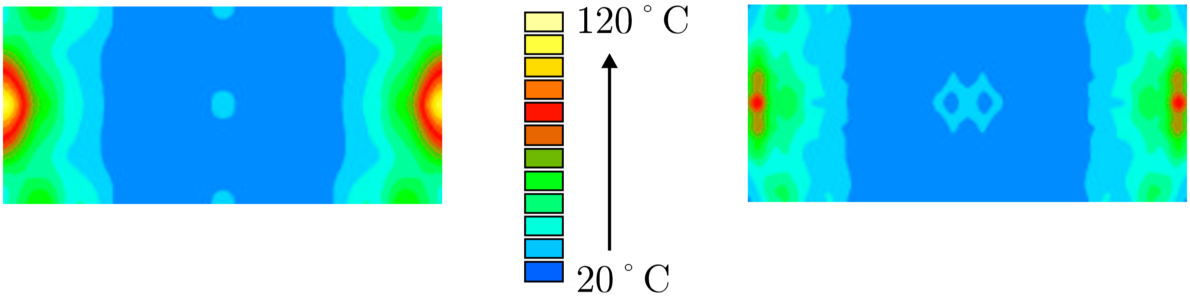

h_e=0.1 kW/m^2 K

h_e=0.5 kW/m^2 K

Figure 7.1: Calculated surface temperature distribution for two values of the convective heat transfer coefficient.

with a step size of $\Delta t = 0.01$ seconds for 20 seconds. The temperature calculation took only a couple of minutes to perform on a Sparc-10 and so it is considerably faster than the electric field solution. The calculated temperatures are considerably higher than those shown in the thermal image. With $h_e = 0.1$ kW/m$^2\cdot$K the temperatures at the end of the potato are predicted to exceed 100°C, which of course will not happen in practice since the water in the mashed potato will start to boil. This suggests that neglecting the evaporative losses from the surface produces unacceptable results. The inclusion of mass transfer into the temperature calculation increases the complexity of the calculation significantly, however, this will be required for future calculation if sensible comparisons with experiments are to be made. Increasing h_e has the effect of reducing the surface temperature considerably. This is especially noticeable along the edges at the end of the tray since heat loss at these points will be from two sides. The model was unable to take account of the tray in which the potato was contained. The thin walled plastic tray will have little effect on the electromagnetic field solution, however, it may have a significant effect upon the temperature distribution. Future models should be able to account for the containers in which loads are placed.

7.4 Coupled Electromagnetic and Thermal Models

7.4.1 Introduction

The purpose of this section is to analyse some of the problems that are encountered during the application of the coupled model to multimode cavity problems and to demonstrate, by means of an example, the type of effects that may be observed in temperature dependent systems. Several recent papers have considered the problem coupling the thermal and electromagnetic fields for microwave heating problems [Dibben & Metaxas, 1994a; Sundberg, 1994; Huang *et al.*, 1994]. However, very few results are available for the coupled problem in multimode cavities. Ayappa *et al.* [1991] use a one dimensional finite element model to investigate the heating caused by plane waves incident on a multilayered slab. The results show that the temperature dependence of the material properties can appreciably effect the temperature distribution. The application of this one dimensional model to real problems is, however, extremely limited. Shouzheng & Davis [1991] and Sekkak *et al.* [1994] have also considered the effects on the electric field of the temperature dependence of dielectric properties although for a short circuited waveguide loaded with a dielectric material. They have shown that the use of a coupled model results in power density and temperature profiles that are significantly different from those produced by assuming no variation in power density with temperature.

It was seen in Chapter 6 that for low loss materials it was necessary to produce solutions at several frequencies in order to determine the sensitivity of the system. This remains true for the coupled model which will require repeated calculations for each frequency being modelled: the coupled model cannot produce multiple frequency solutions from a single calculation. This obviously will increase the cost of the calculation enormously.

The power supplied to the cavity determines the temperature rise, which in turn will determine the development of the electric field distribution during heating. Small variations in the power supplied to the cavity may therefore cause the temperature distribution to evolve in a different manner. This leads to the observation that small errors in the reflection coefficient, which through equation (4.21) will determine the power absorbed by the load, may lead to large changes in the field and temperature distributions later on in the heating cycle. The results in Chapters 5 and 6 for the reflection coefficient show large variations in the magnitude with frequency. This suggests that it is also necessary to solve the system with a variety of power levels to determine the sensitivity to changes in absorbed power. This will also give an indication of the sensitivity to errors in the reflection coefficient.

Taking the above comments together, and assuming that it is desired to solve the system at, say, 5 frequencies and 5 power levels then this requires 25 repeated solutions. Each solution will require several field calculations. If, for example, 10 field calculations were required per solution then this leads to a total of 250 field calculations. Even the shorter calculations presented in Chapter 6 took 4 hours to complete, so that the problem described here would require 41 days to complete! These numbers are somewhat arbitrary, but they demonstrate one of the most obvious problems with implementing the coupled model; the fact that the large computational burden of repeat solutions leads to unacceptably large solution times.

Before the temperature feedback scheme, which is outlined below, can be used for real multimode cavity problems there will need to be a considerably more research carried out to understand the electromagnetic phenomena involved in modelling multimode cavities. The scheme presented here is therefore of only theoretical interest at present.

7.4.2 Temperature Feedback

In order to reflect the changes in dielectric properties with temperature the algorithm shown in Figure 7.2 was implemented. The time scales of the thermal and electromagnetic systems are very different. For the electromagnetic system changes take place in nano seconds compared to the several seconds required for the thermal system. This allows the two calculations to be performed separately. During the heat flow calculation the temperature of each element is monitored. When the change in temperature is sufficient to produce a significant change in dielectric properties the temperature calculation is suspended and the electric field distribution is recalculated. After each recalulation of the electric field the reflection coefficient is calculated so that the absorbed power can be determined and the values of the power density scaled accordingly. This procedure continues until the load has reached a pre-set temperature or a specified time period

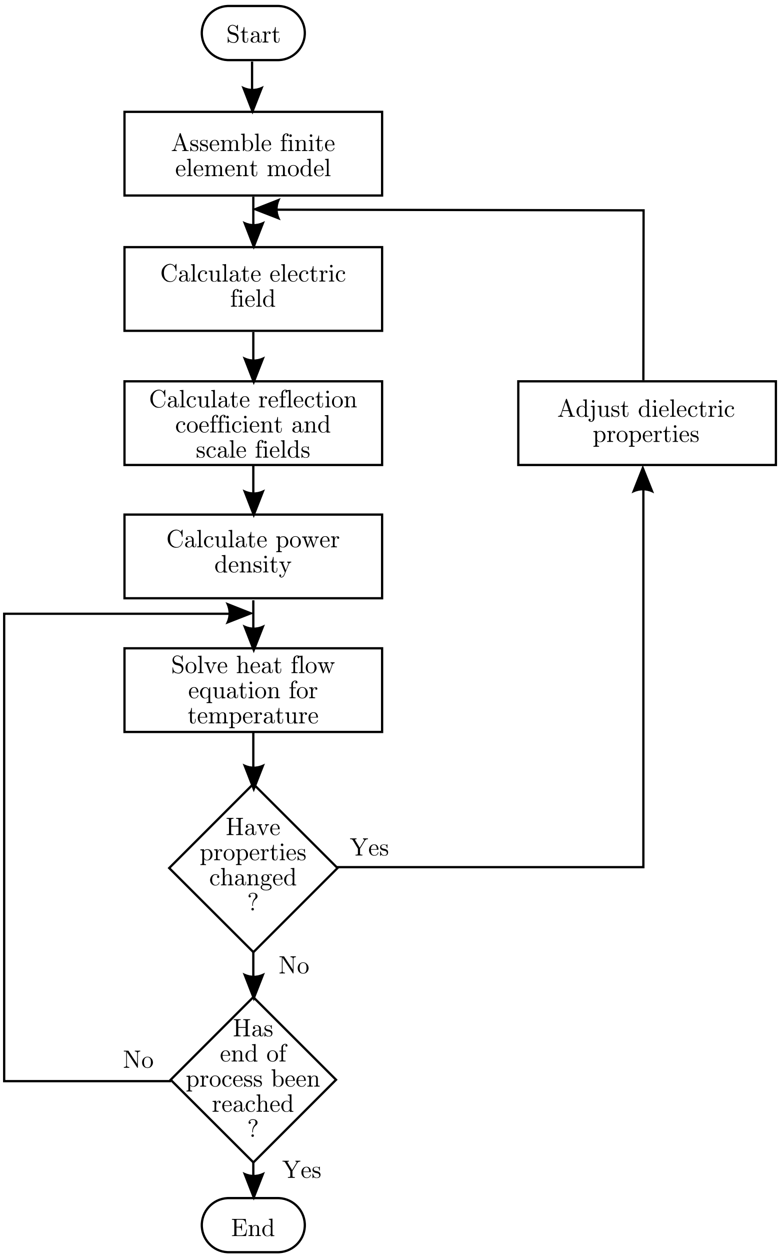

Figure 7.2: Flow chart showing temperature feedback algorithm.

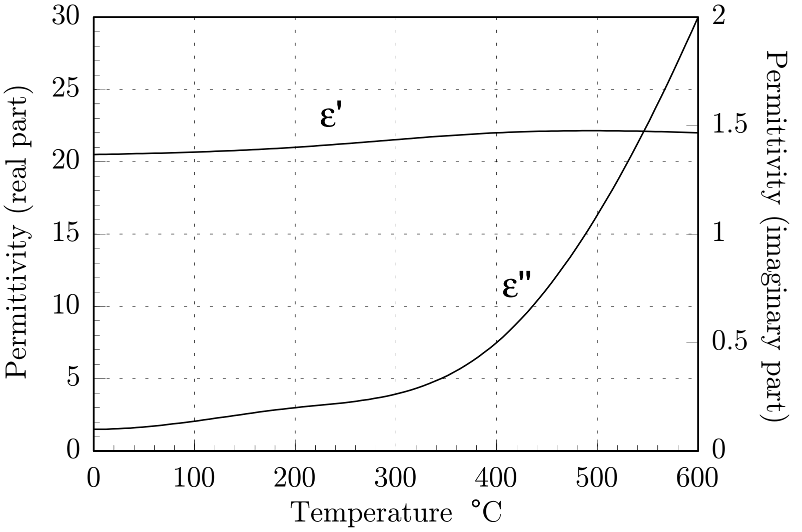

Figure 7.3: Relative permittivity and conductivity of Zirconia against temperature. (from Arai *et al.* [1993])

has elapsed.

Conceptually this procedure is very simple, however, there are many issues that are not yet understood. For example, what constitutes a significant rise in dielectric properties? If the electric field is recalculated after too small a change then the solution time will be prolonged. Conversely, if too large a change is allowed before re-calculation then the development of the temperature distribution will be altered. The change in properties that will cause a significant change in field distribution will be very problem-dependent. If the system is operating close to a sharp resonance a small change could produce very large changes in the reflection coefficient and therefore in the absorbed power.

7.4.3 Ceramic Block Example

In order to demonstrate the application of the temperature feedback to a multimode cavity, a block of ceramic was modelled. The ceramic that was chosen was zirconia, which has a permittivity that varies with temperature, as shown in Figure 7.3. A

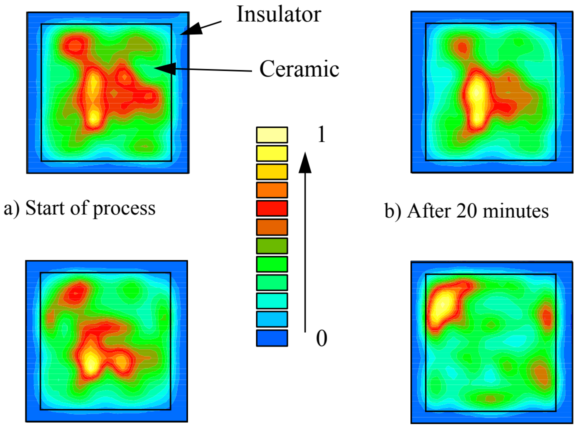

a) Start of process
b) After 20 minutes
c) After 30 minutes
d) After 50 minutes

Figure 7.4: Normalise lock on an x-y plane
through the centre of

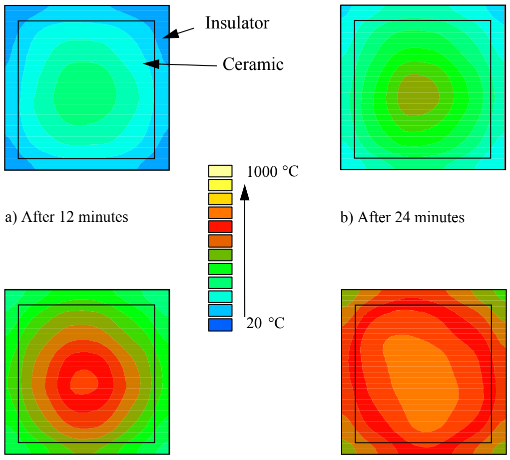

a) After 12 minutes
b) After 24 minutes
c) After 40 minutes
d) After 55 minutes

Figure 7.5: Temperature density distribution in the ceramic block on an x-y plane through the centre of the ceramic.

cube of zirconia, 100 mm in each dimension, was modelled in a cavity with the same dimensions as that used for the mashed potato (see §6.4). This time, however, the waveguide feed was positioned on the side of the cavity, in order to produce a non-symmetric excitation. This was to give a more non-uniform heating pattern that was likey to show more significant variations with changes in dielectric properties. In the model the ceramic was surrounded by a layer of insulating material 20 mm thick, with relative permittivity taken to be $\epsilon_r = 1.54 - \jmath 0.01$. The magnetron was assumed to have an output power of 1 kW. The finite element mesh that was used consisted of 114,620 tetrahedral elements, giving rise to 130,000 unknowns. The power density distribution in a horizontal slice through the centre of the ceramic and insulator assembly is shown in Figure 7.4 for various stages of the heating process. The temperatures attained in the ceramic are shown in Figure 7.5. As the temperature at the centre of the ceramic rises we initially see a concentration of the power density in a single area, shown in Figure 7.4(b). This is due to the rise in the effective conductivity. However, as the temperature continues to rise, the conductivity increases significantly which produces a change in the electric field pattern within the cavity. This alters the power density distribution, as shown in Figure 7.4(c).

This solution is presented as an example of they type of effects that may be observed in coupled problems. Since there is no experimental evidence to verify the validity of the solution there is no way to check the asumptions that have been made.

7.5 Conclusions

The solution of the heat flow equation for microwave heated loads requires considerably more work before accurate comparisons between experiment and theory can be obtained. It has been shown that neglecting evaporative losses leads to an overestimation of the temperatures. It is also necessary to determine accurate values for the thermal properties over the temperature range of interest.

The solution of coupled problems for multimode cavities needs either faster computing hardware or an advance in the algorithms used for the calculation if reasonable solution times are to be obtained. If the electric field can be updated rather than recalculated after each change in dielectric properties then a reduction in solution time may be obtained, however, research into how this can be implemented has yet to be carried out.

Chapter

8

Conclusions and Recommendations for Further Work

The most significant part of this thesis is the development of the time domain finite element method for the solution of multimode cavity problems. With Gaussian pulse excitation the method allows solution at multiple frequencies, which was seen to be vital for lightly loaded multimode applicators. The time domain method is also an order of magnitude faster than the frequency domain method for multimode cavities loaded with food-like materials. This was due to severe ill-conditioning in the frequency domain. Comparisons with experimental results have shown that the methods give good agreement in many cases. The problem of the plastic block loaded cavity demonstrated that, for low loss materials, the system is extremely sensitive to small changes in frequency which necessitates solution at several frequencies.

The frequency domain method is well suited to the analysis of single mode applicators where the problem of ill-conditioning does not arise. This enables solutions at a single frequency to be obtained in a couple of minutes of computer time. The time domain method, which needs many cycles of the field to obtain accurate results, was considerably slower for this type of problem. Comparisons with results obtained using other numerical methods show that the methods presented here compare favourably, however, certain differences between calculation and experiment remain, the causes of which still need to be addressed.

Results in Chapter 2 showed that, when post-processed correctly, Whitney edge elements give consistently lower errors than both nodal elements and linear edge elements. When coupled with the absence of spurious modes and their ability to model sharp metal corners and dielectric discontinuities this makes Whitney edge elements the best choice for the discretisation. The ability of edge elements to give accurate answers was confirmed by the good agreement with experimental results obtained in Chapter 6.

The coupled thermal and electromagnetic problem with temperature dependent material properties was seen to be particulary difficult in multimode applicators. This is due to the sensitivity of the system to small changes which are then amplified by the non-linear nature of the coupled problem.

The problems associated with the simulation that have been outlined in this dissertation would suggest that that the role of analysis lies not in predicting exact distributions for specific situations but rather in analysing the effects of changes to the system. For example, a designer may wish to investigate a new type of food packaging. The analysis techniques can be used to produce temperature distributions in the food for different positions of the package in a given cavity. Since the distribution will depend on both the cavity used and the position of the load the calculation cannot find the actual distribution that will be obtained in a consumers own oven. However, the designer can use the analysis to get a feel for the behaviour of the packaging. For example, some areas may consistently overheat or remain cold so the packaging can be re-designed to account for this.

8.1 Recommendations for Further Work

Many areas remain which require further understanding and development.

- Further comparisons with experimental data are required in order to fully understand the physical effects that can produce significant changes in the field distribution. This is particularly true for the case where the material properties vary with temperature.

- Investigation into the causes of ill-conditioning with multimode applicators. This may lead to new solution methods that allow solutions to the frequency domain problem in a reasonable time, maybe through the use of multigrid or domain decomposition algorithms.

- One of the limiting factors of the problems analysed in this dissertation was mesh generation. Better mesh generation tools need to be applied to this problem. The application of adaptive techniques has the potential to reduce computation times while improving accuracy.
- The post-processing of Whitney element results was seen to improve both the accuracy and the rate of convergence on mesh refinement. However, only fairly simple techniques were applied to the post-processing, more sophisticated techniques are worth investigation as well as establishing a theoretical basis for the post-processing methods.
- Results for single mode cavities showed that the wall losses may play a significant role in certain cavities. The inclusion of these losses must therefore be considered for future calculations.
- More work is required in the correct modelling of the apertures used to couple single mode systems. Apertures with rounded corners have not been modelled, however, they are used in real systems.
- For food like materials the inclusion of evaporative losses was seen to be necessary. The extension of the temperature solution algorithms to include mass transfer must therefore be a priority if food like materials are to be studied in depth.
- This thesis has only considered multimode cavities with static loads, whereas in practice the load is often on a conveyor or turntable. Mode stirrers are also used to improve heating uniformity in many ovens. The inclusion of these into the model presents several difficulties not least in the more complex mesh generation routines that will be required. Their inclusion into the model, however, is necessary if real systems are to be modelled.
- A further area that was not considered in this dissertation but which is relevant to many industrial applicators is the use of multi-port feeds. The effect of the

number of feeds and their position is a topic that is yet to be investigated.

- The applicators studied in this dissertation were fed via an iso-circulator that has the effect of decoupling the source from the load. In many real situations, for example domestic ovens, iso-circulators are not used. In these situations it will be necessary to determine the effect on the operating frequency and output power of the load impedance. Furthermore, the use of an ABC to terminate the waveguide mesh may no longer be valid.

Bibliography

Akhtarzad, S. & Johns, P. (1975). Solution of Maxwell's Equations in Three Space Dimensions and Time by the TLM Method of Numerical Analysis. *Proc. IEE 122*(12), 1344–1348.

Ambrosiano, J., Brandon, S., Löhner, R., & DeVore, C. (1994). Electromagnetics via the Taylor-Galerkin Finite Element Method on Unstructured Grids. *Journal of Computational Physics 110*, 310–319.

Arai, M., Binner, J., Carr, G., & Cross, T. (1993). High Temperature Dielectric Property Measurements of Engineering Ceramics. In *Proceedings of the symposium on Microwaves: Theory and Application in Materials Processing II, Cincinnati,OH.* American Ceramic Society.

Audhuy-peaudecerf, M., Lefeuvre, S., Majdabadino, M., & Hathouti, S. (1993). Mathematical Modelling of EM Fields in a Loaded Microwave Oven. In *28th IMPI Microwave Power Symposium, Montreal, Canada, July 11 – 14*, pp. 201–205.

Axelsson, O. (1980). Conjugate Gradient Type Methods for Unsymmetric and Inconsistent Systems of Linear Equations. *Linear Algebra and its Applications 29*, 1–16.

Ayappa, K., Davis, H., Crapiste, G., Davis, E., & Gordon, J. (1991). Microwave Heating: an Evaluation of Power Formulations. *Chemical Engineering Science 46*(4), 1005–1016.

Ayappa, K., Davis, H., Davis, E., & Gordon, J. (1991). Analysis of Microwave Heating of Materials with Temperature Dependent Properties. *AIChE Journal 37*(3), 313–322.

Baldomir, D. (1986). Differential Forms and Electromagnetism in Three-Dimensional Euclidean Space R^3. *IEE Proceedings Pt. A 133*(3), 139–143.

Bandelier, B. & Rioux-Damidau, F. (1990). Modelling of Magnetic Fields Using Nodal or Edge Variables. *IEEE Transactions on Magnetics 26*(5), 1644–1646.

Bardi, I., Biro, O., Dyczij-Edlinger, R., Preis, K., & Richter, K. (1994a). On the Treatment of Sharp Corners in the FEM Analysis of High Frequency Problems. *IEEE Transactions on Magnetics 30*(5), 3108–3111.

Bardi, I., Biro, O., Dyczij-Edlinger, R., Preis, K., & Richter, K. (1994b). Solution of TEAM Benchmark Problem 18 "waveguide loaded cavity". See Bossavit & Chaussecourte [1994].

Barret, R., Berry, M., Chan, T., Demmel, J., Donato, J., Dongarra, J., Eijkhout, V., Pozo, R., Romine, C., & van der Vorst, H. (1993). *Templates for the Solution of Linear Systems: Building Blocks for Iterative Methods.* Society for Industrial and applied Mathematics, Philadelphia. PA.

Barton, M. & Cendes, Z. (1987). New Vector Finite Elements for Three-Dimensional Magnetic Field Computation. *Journal of Applied Physics 61*(8), 3919–3921.

Bi, Z., Shen, Y., Wu, K., & Litva, J. (1992). Fast Finite Difference Time Domain Analysis of Resonators using Digital Filtering and Spectral Estimation Techniques. *IEEE Transactions on Microwave Theory and Techniques 40*, 1611–1619.

Bossavit, A. (1988a). A Rationale for Edge-Elements in 3-D Field Computations. *IEEE Transactions on Magnetics 24*(1), 74–79.

Bossavit, A. (1988b). Whitney Forms: A Class of Finite Elements for Three-Dimensional Computations in Electromagnetics. *IEE Proceedings Pt. A 135*(8), 493–499.

Bossavit, A. (1990). Solving Maxwell Equations in a Closed Cavity, and the Question of Spurious Modes. *IEEE Transactions on Magnetics 26*(2), 702–705.

Bossavit, A. (1994). A New Rationale for Edge-Elements. *International Compumag Society Newsletter 1*(3), 3–6.

Bossavit, A. (1995). Uniqueness of Solution of Maxwell Equations in the Loaded Microwave Oven, and How it May Fail. Abstract of paper to be presented at International Conference on Microwave and High Frequency Heating, 17-21 Sept. 1995, Cambridge, UK.

Bossavit, A. & Chaussecourte, P. (Eds.) (1994). *The TEAM Workshop in Aix-les-Bains, July 7-8.*

Brezzi, F. & Marini, D. (1994). A Survey On Mixed Finite Element Approximations. *IEEE Transactions on Magnetics 30*(5), 3547–3551.

Buleev, N. (1960). A Numerical Method for the Solution of Two-Dimensional And Three-Dimensional Equations of Difffusion. *Mat. Sb. 51*, 227.

Cai, X.-C. & Widlund, O. (1992). Domain Decomposition Algorithms for Indefinite Elliptic Problems. *SIAM Journal of Scientific and Statistical Computing 13*(1), 243–258.

Chan, C., Sangani, H., Yee, K., & Elson, J. (1994). A Finite-Difference Time-Domain Method using Whitney Elements. *Microwave and Optical Technology Letters 7*(14), 673–676.

Chassecourte, P., Lamaudiere, J., & Maestrali, B. (1993). Electromagnetic Field Modelling of a Loaded Microwave Cavity. In *28th IMPI Microwave Power Symposium, Montreal, Canada, July 11 – 14.*

Chaussecourte, P., Hazard, C., Lamaudiere, J., & Maestrali, B. (1991). 3D Numerical Microwaves; Heating Applications. Communication.

Chen, J., Wu, C., Lo, T., Wu, K.-L., & Litva, J. (1994). Using Linear and Nonlinear Predictors to Improve the Computational Efficiency of the FD-TD Algorithm. *IEEE Transactions on Microwave Theory and Techniques 42*(10), 1992–1997.

Chen, Z., Ney, M., & Hoefer, W. (1991). A New Finite-Difference Time-Domain Formulation and its Equivalence with the TLM Symmetrical Condensed Node. *IEEE Transactions on Microwave Theory and Techniques 39*(12), 2160–2169.

Chew, W. (1990). *Waves and Fields in Inhomogeneous Media.* Van Nostrand Reinhold, New York.

Ciarlet, P. (1978). *The Finite Element Method for Elliptic Problems.* North-Holland, Amsterdam.

Cline, A., Moler, C., Stewart, G., & Wilkinson, J. (1979). An Estimate for the Condition Number of a Matrix. *SIAM Journal on Numerical Analysis 16*, 368–375.

Collin, R. (1991). *Field Theory of Guided Waves : 2nd Edition.* IEEE Press, New York, USA.

Collin, R. (1992). *Foundations for Microwave Engineering.* McGraw-Hill, New Yorks.

Crank, J. & Nicolson, P. (1947). A Practical Method for Numerical Evaluation of Solutions of Partial Differential Equations of the Heat Conduction Type. *Proceedings of the Cambridge Philosophical Society 43*, 50–67.

Davis, J. (1993). Finite Element Analysis of Waveguides and Cavities – a Review. *IEEE Transactions on Magnetics 29*(2), 1578–1583.

Dawes, W. (1992). The Practical Application of Solution-Adaption to the Numerical Simulation of Complex Turbomachinery Problems. *Prog. Aerospace Sci. 29*, 221–269.

de Jongh, P. (1989). Moisture Measurements with Microwaves. In *HF and Microwave conference, ARNHEM.*

de Pourcq, M. (1984). New Power-Density Calculation Method by Three-Dimensional Finite Elements. *IEE Proceedings Pt. H 131*(6), 411–419.

Desai, R., Lowery, A., Christopoulos, C., Naylor, P., Blanshard, J., & Gregson, K. (1992). Computer Modelling of Microwave Cooking Using the Transmission-Line Model. *IEE Proceedings Pt. A 139*(1), 30–38.

Deschamps, G. (1981). Electromagnetics and Differential Forms. *Proceedings of the IEEE 69*(6), 676–696.

Dibben, D. & Metaxas, A. (1994a). Finite Element Analysis of Multi-mode Cavities with Coupled Electrical and Thermal Fields. Presented at the 29th IMPI Microwave Power Symposium, Chicago, USA, 25–27 July.

Dibben, D. & Metaxas, A. (1994b). Finite-Element Time-Domain Analysis of Multimode Applicators Using Edge Elements. *International Journal of Microwave Power and Electromagnetic Energy 29*(4), 242–251.

Duff, I., Erisman, A., & Reid, J. (1986). *Direct Methods for Sparse Matrices.* Clarendon Press, Oxford, UK.

Dyczij-Edlinger, R. (1994). Solution of TEAM Benchmark Problem 19 (Loaded Cavity Resonator). See Bossavit & Chaussecourte [1994].

Eisenstat, S. (1981). Efficient Implementation of a Class of Preconditioned Conjugate Gradient Methods. *SIAM Journal of Scientific and Statistical Computing 2*(1), 1–4.

Engquist, B. & Majda, A. (1977). Absorbing Boundary Conditions for the Numerical Simulation of Waves. *Mathematics of Computation 31*, 629–651.

Eswarappa, C. & Hoefer, W. (1994). Autoregressive (AR) and Autoregressive Moving Average (ARMA) Spectral Estimation Techniques for Faster TLM Analysis of Microwave Structures. *IEEE Transactions on Microwave Theory and Techniques 42*(12), 2407–2411.

Evans, D. (1967). The Use of Pre-conditioning in Iterative Methods for Solving Linear Equations with Symmetric Positive Definite Matrices. *J. Inst. Maths Applics. 4*, 295–314.

Faber, V. & Manteuffel, T. (1984). Necessary and Sufficient Conditions for the Existence of a Conjugate Gradient Method. *SIAM Journal on Numerical Analysis 21*, 352–362.

Femsys Ltd. (1993). *Femgen/Femview User Manual.* Leicester, England: Femsys Ltd.

Fletcher, R. (1976). Conjugate Gradient Methods for Indefinite Systems. In G. Watson (Ed.), *Numerical Analysis, Dundee. Lecture Notes in Mathematics 506*, pp. 73–89. Springer-Verlag, Berlin.

Flockhart, C., Trenkic, V., & Christopoulos, C. (1994). The Simulation of Coupled Electromagnetic and Thermal Problems in Microwave Heating. In *Second International Conference on Computational Electromagnetics, Nottingham, UK, 12–14 April*, Volume 384. IEE.

Freund, R. (1992). Conjugate Gradient-Type Methods for Linear Systems with Complex Symmetric Coefficient Matrices. *SIAM Journal of Scientific and Statistical Computing 13*(1), 425–448.

Freund, R. & Nachtigal, N. (1991). QMR: A Quasi-minimal Residual Method for Non-Hermetian and Linear Systems. *Numerische Mathematik 60*, 315–339.

Fu, W. & Metaxas, A. (1994). Numerical Prediction of Three-Dimensional Power Density Distribution in a Multi-Mode Cavity. *International Journal of Microwave Power and Electromagnetic Energy 29*(2), 67–75.

George, A. & Liu, J. (1981). *Computer Solution of Large Sparse Positive Definite Systems.* Prentice Hall, London.

George, P. (1991). *Automatic Mesh Generation.* John Wiley and Sons, Chichester, UK.

Golias, N., Papagiannakis, A., & Tsiboukis, T. (1994). Efficient Mode Analysis with Edge Elements and 3-D Adaptive Refinement. *IEEE Transactions on Microwave Theory and Techniques 42*(1), 99–107.

Gustafsson, I. (1978). A Class of First Order Factorization Methods. *BIT 18*, 142.

Hager, W. (1984). Condition Estimates. *SIAM Journal of Scientific and Statistical Computing 5*(2), 311–316.

Hammer, P., Marlowe, O., & Stroud, A. (1956). Numerical Integration over Simplexes and Cones. *Mathematical Tables and other Aids to Computation 10*(55), 130–136.

Hammond, P. & Baldomir, D. (1988). Dual Energy Methods in Electromagnetism using Tubes and Slices. *IEE Proceedings Pt. A 135*(3), 167–172.

Hara, M., Wada, T., Fukasawa, T., & Kikuchi, F. (1983). A Three Dimensional Analysis of RF Electromagnetic Fields by the Finite Element Method. *IEEE Transactions on Magnetics 19*(6), 2417–2420.

Haugazeau, Y. & Lacoste, P. (1993). Condensation de la Matrice Masse pour les Éléments Finis Mixtes de H(rot). *Comptes Rendus de l'Academie des Sciences Serie I. 316*(5), 509–512.

Hestenes, M. & Stiefel, E. (1952). Methods of Conjugate Gradients for Solving Linear Systems. *J. Res. Nat. Bur. Standards 49*(6), 409–436.

Hoefer, W. (1985). The Transmission-Line Matrix Method – Theory and Applications. *IEEE Transactions on Microwave Theory and Techniques 33*(10), 882–893.

Holland, R. (1993). Pitfalls of Staircase Meshing. *IEEE Transactions on Electromagnetic Compatibility 35*(4), 434–439.

Huang, Z., Iskander, M., Tucker, J., & Kimrey, H. (1994). FDTD Modeling of Realistic Microwave Sintering Experiments. In M. Iskander, R. Lauf, & W. Sutton (Eds.), *Microwave Processing of Materials IV*, Volume 347, pp. 331–345. Materials Research Society.

Irons, B. (1970). A Frontal Solution Program for Finite Element Analysis. *Int. Journ. Numerical Methods in Engineering 2*, 5–32.

Ise, K., Inoue, K., & Koshiba, M. (1990). Three-Dimensional Finite Element Solution of Dielectric Scattering Obstacles in a Rectangular Waveguide. *IEEE Transactions on Microwave Theory and Techniques 38*(9), 1352–1358.

Iskander, M. (1993). Modelling the Microwave Process – Challenges and New Directions. In *Microwaves: Theory and Applications in Materials Processing II*, Ceramic Transactions 36, pp. 167–199. American Ceramic Society.

Iskander, M., Smith, R., Andrade, A., Kimrey, H., & Walsh, L. (1994). FDTD Simulation of Microwave Sintering of Ceramics in Multimode Cavities. *IEEE Transactions on Microwave Theory and Techniques 42*(5), 793–800.

Jacobs, D. (1981). The Exploitation of Sparsity by Iterative Methods. In I. Duff (Ed.), *Sparse Matrices and their Uses*, pp. 191–222. Academic Press, London.

Jia, X. (1993). Experimental and Numerical Study of Microwave Power Distributions in a Microwave Heating Applicator. *International Journal of Microwave Power and Electromagnetic Energy 28*(1), 25–31.

Jia, X. & Jolly, P. (1992). Simulation of Microwave Field and Power Distribution in a Cavity by a Three-Dimensional Finite Element Method. *International Journal of Microwave Power and Electromagnetic Energy 27*(1), 11–22.

Joe, B. (1993). *GEOMPACK Users' Guide.* Edmonton, Alberta, Canada.: Department of Computing Science, University of Alberta.

Katz, D., Thiele, E., & Taflove, A. (1994). Validation and Extension to Three Dimensions of the Berenger PML Absorbing Boundary Condition for FD-TD Meshes. *IEEE Microwave and Guided Wave Letters 4*(8), 268–270.

Kershaw, D. (1978). The Incomplete Cholesky-Conjugate Gradient Method for the Iterative Solution of Linear Equations. *Journal of Computational Physics 26*, 43–65.

Ko, W. & Mittra, R. (1991). A Combination of FD-TD and Prony's Methods for Analyzing Microwave Integrated Circuits. *IEEE Transactions on Microwave Theory and Techniques 39*, 2176–2181.

Koshiba, M., Hayata, K., & Suzuki, M. (1987). Finite-Element Method Analysis of Microwave and Optical Waveguides – Trends in Countermeasures to Spurious Solutions. *Electronics and Communications in Japan, Part 2. 70*(9), 96–108.

Kümpel, W. & Wolff, I. (1994). Digital Signal Processing of Time Domain Field Simulation Results Using the System Identification Method. *IEEE Transactions on Microwave Theory and Techniques 42*(4), 667–671.

Lanczos, C. (1950). An Iteration Method for the Solution of the Eigenvalue Problem of Linear Differential and Integral Operators. *J. res. Nat. Bur. Standards 45*(4), 255–282.

Lee, J. (1994). WETD - A Finite Element Time-Domain Approach for Solving Maxwell's Equations. *IEEE Microwave and Guided Wave Letters 4*(1), 11–13.

Lee, J. & Mittra, R. (1992). A Note on the Application of Edge-Elements for Modeling Three-Dimensional Inhomogeneously-Filled Cavities. *IEEE Transactions on Microwave Theory and Techniques 40*(9), 1767–1773.

Leis, R. (1977). Exterior Boundary-Value Problems in Mathematical Physics. In H. Zorski (Ed.), *Trends in Applications of Pure mathematics to Mecahnics. Vol II*, pp. 187–203. Pitman, London, U.K.

Liao, Z., Wong, H., B.P., Y., & Yuan, Y. (1984). A Transmitting Boundary for Transient Wave Analyses. *Scientia Sinca, Series A. 27*(10), 1063–1076.

Liu, F., Turner, I., & Bialkowski, M. (1994). A Finite-Difference Time-Domain Simulation of Power-Density Distribution in a Dielectric-Loaded Microwave Cavity. *International Journal of Microwave Power and Electromagnetic Energy 29*(3), 138–148.

Lorenson, C. & Gallerneault, C. (1991). Numerical Methods for the Modelling of Microwave Fields. In *Proceedings of the Symposium on Microwaves: Theory and Applictation in Materials Processing held during the 93rd Annual Meeting of the American Ceramic Society in Cincinnati,OH, April 29-May 3*, pp. 193–200. American Ceramic Society.

Ludeman, L. (1987). *Fundamentals of Digital Signal Processing.* John Wiley and Sons, New York.

Lynch, D. & Paulsen, K. (1991). Origin of Vector Parasites in Numerical Maxwell Solutions. *IEEE Transactions on Microwave Theory and Techniques 39*(3), 383–394.

Ma, L., Pothecary, N., & Railton, C. (1994). Application of the FDTD Technique on Microwave Heating. In *Second International Conference on Computation in Electromagnetics, Nottingham, U.K., 12–14 April.*

Madsen, N. & Ziolkowski, R. (1988). Numerical-Solution of Maxwell Equations in the Time Domain Using Irregular Non-orthogonal Grids. *Wave Motion 10*(6), 583–596.

Manteuffel, T. (1980). An Incomplete Factorisation Technique for Positive Definite Linear Systems. *Mathematics of Computation 34*, 473–497.

Meijerink, J. & van der Vorst, H. (1977). An Iterative Solution Method for Linear Systems of which the coefficient Matrix is an M-Matrix. *Mathematics of Computation 31*, 148.

Meijerink, J. & van der Vorst, H. (1981). Guidelines for the Usage of Incomplete Decompositions in Solving Sets of Linear Equations as They Occur in Practical Problems. *Journal of Computational Physics 44*, 134–155.

Meredith, R. (1994). A 3 Axis Model of the Mode Structure of Multimode Cavities. *Journal of microwave power and electromagnetic energy 29*(1), 31–44.

Metaxas, A. (1974). Design of a TM_{010} Resonant Cavity to Process Liquid Foodstuffs at 896 MHz. Technical Report ECRC/M767, The Electricity Council Research Centre, Capenhurst, England.

Metaxas, A. & Meredith, R. (1978). Microwave Drying of Nylon Tufted carpets II. Electrical Characterization of a Modified $\mathrm{TE}_{10\mathrm{n}}$ Resonant Cavity. *International Journal of Microwave Power and Electromagnetic Energy 13*(4), 315–320.

Metaxas, A. & Meredith, R. (1983). *Industrial Microwave Heating.* Peter Perigrinus, London, U.K.

Mitchell, S. & Vavasis, S. (1992). Quality Mesh Generation in Three Dimensions. In *Proc. 8th Symposium on Computational Geometry*, pp. 212–221. ACM Press.

Monk, P. (1992). A Finite Element Method for Approximating the Time-Harmonic Maxwell Equations. *Numerische Mathematik 63*, 243–261.

Monk, P. (1993). An Analysis of Nédélec's Method for the Spatial Discretization of Maxwell's Equations. *Journ. Computational and Applied Mathematics 47*, 101–121.

Mur, G. (1981). Absorbing Boundary Conditions for the Finite-Difference Approximation of the Time-Domain Electromagnetic-Field Equations. *IEEE Transactions on Electromagnetic Compatibility 23*(4), 377–382.

Mur, G. (1988). Optimum Choice of Finite-Elements for Computing Three-Dimensional Electromagnetic Fields in Inhomogeneous Media. *IEEE Transactions on Magnetics 24*(1), 330–333.

Mur, G. (1994). Edge Elements, their Advantages and their Disadvantages. *IEEE Transactions on Magnetics 30*(5), 3552–3557.

Mur, G. & Dehoop, A. (1985). A Finite-Element Method for Computing Three-Dimensional Electromagnetic Fields in Inhomogeneous Media. *IEEE Transactions on Magnetics 21*(6), 2188–2191.

Nédélec, J. (1980). Mixed Finite Elements in $\Re^3$. *Numerische Mathematik 35*, 315–341.

Nédélec, J. (1986). A New Family of Mixed Finite-Elements in $\Re^3$. *Numerische Mathematik 50*(1), 57–81.

Nicolaides, R. & Choudhury, S. (1986). Iterative Methods for Elliptic Finite Element Equations on General Meshes. In R. Voigt (Ed.), *Finite Elements: Theory and Applications*, pp. 94–123. Springer-Verlag, New York.

Paige, C. & Saunders, M. (1975). Solution of Sparse Indefinite Systems of Linear Equations. *SIAM Journal on Numerical Analysis 12*(4), 617–629.

Paoloni, F. (1989). Calculation of Power Deposition in a Highly Overmoded Rectangular Cavity with Dielectric Loss. *International Journal of Microwave Power and Electromagnetic Energy 24*(1), 21–32.

Parlett, B. (1980). *The Symmetric Eigenvalue Problem.* Prentice-Hall, Englewood Cliffs, NJ., USA.

Paulsen, K. & Lynch, D. (1991). Elimination of Vector Parasites in Finite-Element Maxwell Solutions. *IEEE Transactions on Microwave Theory and Techniques 39*(3), 395–404.

Paulsen, K., Lynch, D., & Liu, W. (1992). Conjugate Direction Methods for Helmholtz Problems with Complex-Valued Wavenumbers. *Int. Journ. Numerical Methods in Engineering 35*(3), 601–622.

Paulsen, K., Lynch, D., & Strohbehn, J. (1987). Numerical Treatment of Boundary Conditions at Points Connecting More than Two Electrically Distinct Regions. *Communications in Applied Numerical Methods 3*(1), 53–62.

Pinchuk, A., Crowley, C., & Silvester, P. (1988). Spurious Solutions to Vector Diffusion and Wave Field Problems. *IEEE Transactions on Magnetics 24*(1), 158–161.

Rahman, B., Fernandez, F., & Davis, J. (1991). Review of Finite Element methods for Microwave and Optical Waveguides. *Proceedings of the IEEE 79*(10), 1442–1448.

Ramage, A. & Wathen, A. (1994). On Preconditioning for Finite Element Equations on Irregular Grids. *SIAM Journal on Matrix Analysis and Applications 15*(3), 909–921.

Raviart, P. & Thomas, J. (1977). Primal Hybrid Finite Element Methods for 2nd Order Elliptical Equations. *Mathematics of Computation 31*(138), 391–413.

Reid, J. (1970). On the Method of Conjugate Gradients for the Solution of Large Sparse Systems of Linear Equations. In J. Reid (Ed.), *Large Sparse Sets of Linear Equations (1971)*, pp. 231–254. Academic Press, London.

Risman, P. (1993). Microwave Oven Loads for Power Measurements. *Microwave World 14*(1), 14–19.

Rogers, G. & Mayhew, Y. (1980). *Engineering Thermodynamics Work and Heat Transfer (third edition)*. Longman, London.

Saad, Y. (1989). Krylov Subspace Methods on Super Computers. *SIAM Journal of Scientific and Statistical Computing 10*(6), 1200–1232.

Schroeder, W. & Wolff, I. (1994). The Origin of Spurious Modes in Numerical Solutions of Electromagnetic Field Eigenvalue Problems. *IEEE Transactions on Microwave Theory and Techniques 42*(4), 644–653.

Sekkak, A., Pichon, L., & Razek, A. (1994). 3-D FEM Magneto-Thermal Analysis in Microwave Ovens. *IEEE Transactions on Magnetics 30*(5), 3347–3350.

Shouzheng, Z. & Davis, J. (1991). Non Linear Modeling of Microwave Heating Problems. In *IEE International Conference on Computation in Electromagnetics, London, U.K. 25–27 November.*

Silvester, P. & Ferrari, R. (1990). *Finite Elements for Electrical Engineers.* Cambridge University Press, Cambridge, U.K.

Silvester, P. & Omeragić, D. (1993). A Comparitive Experimental Study of Differentiation Methods on Finite Elements. *International Journal of Applied Electromagnetics in Materials 4*, 123–136.

Singh, R. & Heldman, D. (1984). *Introduction to Food Engineering.* Academic Press, Inc., Orlando.

Sundberg, M. (1994). Simulation of Sterilization and Pasteurization in Multi-Mode Applicators. In *29th IMPI Microwave Power Symposium, Chicago, USA, 25–27 July.*

Taflove, A. (1988). Review of the Formulation and Applications of the Finite-Difference Time -Domain Method for Numerical Modelling of Electromagnetic Wave Interactions with Arbitrary Structures. *Wave Motion 10*, 547–582.

van der Vorst, H. (1989). High Performance Preconditioning. *SIAM Journal of Scientific and Statistical Computing 10*(6), 1174–1185.

van der Vorst, H. (1992). Bi-CGStab: A Fast and Smoothly Converging Varient of Bi-CG for the Solution of Nonsymmetric Linear Systems. *SIAM Journal of Scientific and Statistical Computing 13*(2), 631–644.

van Welij, J. (1985). Calculation of Eddy Currents in Terms of H on Hexahedra. *IEEE Transactions on Magnetics 21*(6), 2239–2241.

Varga, R. (1960). Factorisation and Normalized Iterative Methods. In R. Langer (Ed.), *Boundary Value Problems in Differential Equations*, pp. 121. University of Wisconsin Press, Madison.

Vavasis, S. (1993). Stable Finite Elements for Problems with Wild Coefficients. Technical Report CTC93TR147, Cornell Theory Center.

Wathen, A. (1987). Realistic Eigenvalue Bounds for the Galerkin Mass Matrix. *IMA Journal of Numerical Analysis 7*, 449–457.

Webb, J. (1981). *Developments in a Finite Element Method for Three-Dimensional Electromagnetic Problems*. Ph. D. thesis, Cambridge University, U.K.

Webb, J. (1988). Finite Element Analysis of Dispersion in Waveguides with Sharp Metal Edges. *IEEE Transactions on Microwave Theory and Techniques 36*(12), 1819–1823.

Webb, J. (1993). Edge Elements and What They can do for You. *IEEE Transactions on Magnetics 29*(2), 1460–1465.

Webb, J. & Forghani, B. (1993). Heirarchal Scalar and Vector Tetrahedra. *IEEE Transactions on Magnetics 29*(2), 1495–1498.

Webb, J., Maile, G., & Ferrari, R. (1983). Finite-Element Solution of Three-Dimensional Electromagnetic Problems. *IEE Proceedings Pt. H 130*(2), 153–159.

Weiss, R. (1994). Minimization Properties and Short Recurrences for Krylov Subspace Methods. *Electronic Transactions on Numerical Analysis 2*, 57–75.

Whitney, H. (1957). *Geometric Integration Theory*. Princeton University Press, New Jersey, U.S.A.

Wong, S. & Cendes, Z. (1988). Combined Finite Element-Modal Solution of Three-Dimensional Eddy Current Problems. *IEEE Transactions on Magnetics 24*(6), 2685–2687.

Wood, W. (1990). *Practical Time Stepping Schemes*. Clarendon Press, Oxford, U.K.

Yamashita, E. (Ed.) (1990). *Analysis Methods for Electromagnetic Wave Problems*. Artech House, Boston.

Yee, K. (1966). Numerical Solution of Initial Boundary Value Problem Involving Maxwell's Equations in Isotropic Media. *IEEE Transactions on Antennas and Propagation 14*, 302–307.

Zhu, Z., Davis, J., & Fernandez, F. (1994). 3-D Edge Element Analysis of Dielectric Loaded Resonant Cavities. *Int. Journal of Numerical Modelling : Electronic Networks, Devices and Fields 7*(1), 35–41.

Zienkiewicz, O. (1977). *The Finite Element Method*. McGraw-Hill, London.

Appendix

A Element Types

The basis functions for tetrahedral edge elements are easily defined [Bossavit, 1988b]. The element matrices for Whitney elements have been given explicilty by Lee & Mittra [1992]. However, the other element shapes require more work. Hexahedral edge elements have been defined by van Welij [1985] and hexahedral, prismatic and wedges by Brezzi & Marini [1994]. This appendix provides the full list of the basis functions for hexahedral and prismatic edge elements.

A.1 Hexahedral Edge Elements

Each hexahedron K is seen as the image of the unit cube $\hat{K}$ under a tri-linear mapping $F(\mathbf{s}) :\rightarrow \mathbf{r}$, as shown in Figure A.1. [van Welij, 1985] On the unit cube we can define shape functions λ_i associated with each node i, these are shown in Table A.1. The mapping $F(\mathbf{s})$ is then defined by [Ciarlet, 1978],

$$F\colon \mathbf{s} \in \hat{K} \rightarrow F(\mathbf{s}) = \sum_{i=1}^{N} \lambda_i(\mathbf{s})\mathbf{a}_i(x, y, z), \tag{A.1}$$

where $\lambda_i(\mathbf{s})$ is the value of the local coordinate evaluated at $\mathbf{s}$ and the $\mathbf{a}_i(x, y, z)$ are the vertices of the hexahedron.

The elements have degrees of freedom associated with their edges, being the tangential component of the field along the edge. For the edge where $s_2 = 1$ and $s_3 = 1$, which

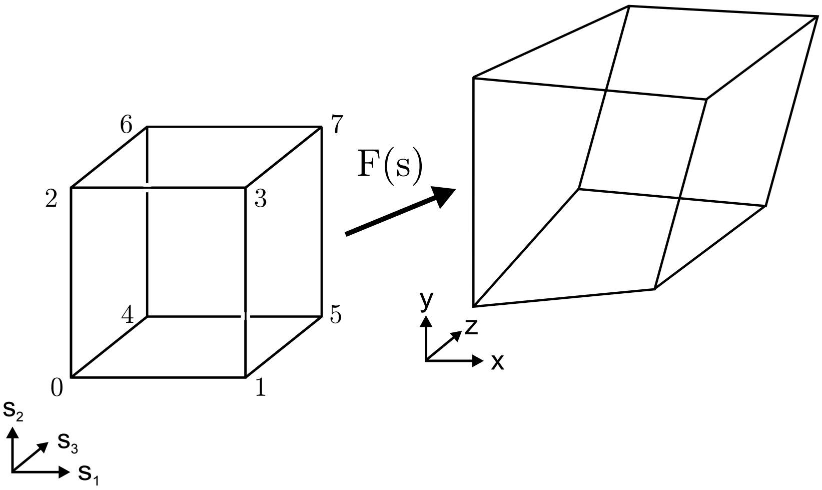

Figure A.1: Unit cube mapped onto the hexahedron by $F(\mathbf{s})$.

$$\begin{aligned}
\lambda_0 &= -s_1 - s_2 - s_3 + s_1 s_2 + s_1 s_3 & \lambda_4 &= s_3 - s_1 s_3 - s_2 s_3 + s_1 s_2 s_3 \\
&\qquad + s_2 s_3 - s_1 s_2 s_3 + 1 & & \\
\lambda_1 &= s_1 - s_1 s_2 - s_1 s_3 + s_1 s_2 s_3 & \lambda_5 &= s_1 s_3 - s_1 s_2 s_3 \\
\lambda_2 &= s_2 - s_1 s_2 - s_2 s_3 + s_1 s_2 s_3 & \lambda_6 &= s_2 s_3 - s_1 s_2 s_3 \\
\lambda_3 &= s_1 s_2 - s_1 s_2 s_3 & \lambda_7 &= s_1 s_2 s_3
\end{aligned}$$

Table A.1: Homogeneous coordinates for hexahedral element

is in the direction of s_1, the shape function is defined as,

$$\mathbf{w}_2 = s_2 s_3 \nabla s_1. \tag{A.2}$$

This function is normal to the faces $s_1 = 0$ and $s_1 = 1$, and so does not contribute to the tangential component of the field on these faces. On all edges in the direction s_1 except for the edge for which $\mathbf{w}_2$ is defined, the product $s_2 s_3$ is zero so the function vanishes. On its own edge the tangential component is constant. The numbering scheme for the edges is shown in Figure A.2. The full set of edge shape functions are given in Table A.2.

In order to assemble the finite element matrices it is necessary to integrate the

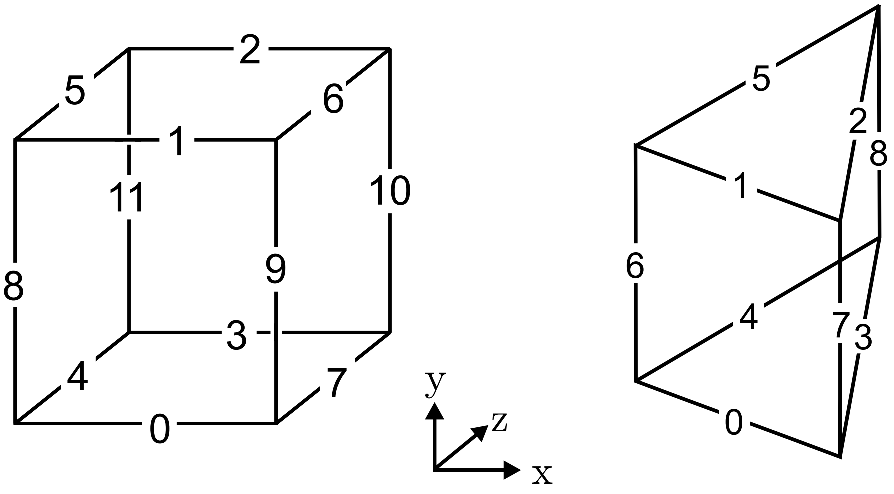

Figure A.2: Edge numbering for hexahedron and prism.

functions over the volume of the element. This requires the evaluation of the shape functions. van Welij [1985] defines

$$\mathbf{V}_i = \frac{\mathrm{d}\mathbf{r}}{\mathrm{d}\mathbf{s}_i}, \tag{A.3}$$

which is easily obtainable from the the shape functions given in Table A.1 and equation (A.1). The Jacobian matrix, $\mathrm{d}\mathbf{r}/\mathrm{d}\mathbf{s}$, has $\nabla \mathbf{s}_i$ as its rows and is the inverse of $\mathrm{d}\mathbf{s}/\mathrm{d}\mathbf{r}$, which has $\mathbf{V}_i$ as its columns;

$$\frac{\mathrm{d}\mathbf{s}}{\mathrm{d}\mathbf{x}} = J \quad = \begin{vmatrix} \frac{\partial s_1}{\partial x} & \frac{\partial s_1}{\partial y} & \frac{\partial s_1}{\partial z} \\ \frac{\partial s_2}{\partial x} & \frac{\partial s_2}{\partial y} & \frac{\partial s_2}{\partial z} \\ \frac{\partial s_3}{\partial x} & \frac{\partial s_3}{\partial y} & \frac{\partial s_3}{\partial z} \end{vmatrix} \tag{A.4}$$

$$\frac{\mathrm{d}\mathbf{x}}{\mathrm{d}\mathbf{s}} = J^{-1} \quad = \begin{vmatrix} \frac{\partial x_1}{\partial s_1} & \frac{\partial x_1}{\partial s_2} & \frac{\partial x_1}{\partial s_3} \\ \frac{\partial x_2}{\partial s_1} & \frac{\partial x_2}{\partial s_2} & \frac{\partial x_2}{\partial s_3} \\ \frac{\partial x_3}{\partial s_1} & \frac{\partial x_3}{\partial s_2} & \frac{\partial x_3}{\partial s_3} \end{vmatrix} \tag{A.5}$$

$$\begin{array}{lcllcl}
\mathbf{w}_0 & = & (1-s_2)(1-s_3)\nabla s_1 & \mathbf{w}_1 & = & s_2(1-s_3)\nabla s_1 \\
\mathbf{w}_2 & = & s_2 s_3 \nabla s_1 & \mathbf{w}_3 & = & s_3(1-s_2)\nabla s_1 \\
\mathbf{w}_4 & = & (1-s_1)(1-s_2)\nabla s_3 & \mathbf{w}_5 & = & s_2(1-s_1)\nabla s_3 \\
\mathbf{w}_6 & = & s_1 s_2 \nabla s_3 & \mathbf{w}_7 & = & s_1(1-s_2)\nabla s_3 \\
\mathbf{w}_8 & = & (1-s_1)(1-s_3)\nabla s_2 & \mathbf{w}_9 & = & s_1(1-s_3)\nabla s_2 \\
\mathbf{w}_{10} & = & s_1 s_3 \nabla s_2 & \mathbf{w}_{11} & = & s_3(1-s_1)\nabla s_2
\end{array}$$

Table A.2: Shape functions for hexahedral edge elements.

So that,

$$\mathbf{V}_i \cdot \nabla s_j = \delta_{i,j} \tag{A.6}$$

where $\delta_{i,j}$ is the Kroneker delta function. The inverse of a matrix can be written,

$$A^{-1} = \frac{adj\ A}{|A|}, \tag{A.7}$$

where *adj A* is obtained by transposing A and replacing each element by its co-factor. The co-factors are no more than the cross products of the appropriate $\mathbf{V}_i$'s so we can get an expression for ∇s_i;

$$\nabla s_1 = \frac{\mathbf{V}_2 \times \mathbf{V}_3}{(\mathbf{V}_2 \times \mathbf{V}_3) \cdot \mathbf{V}_1}. \tag{A.8}$$

The denominator is the determinant of the matrix, so is the same for all three gradients. These equations now allow the shape functions for an arbitary hexahedron to be written entirely in the local coordinates s, and functions $\mathbf{V}_i$ which are easily calculated from the vertices of the hexahedron.

The *curl* of the shape function $\mathbf{w}$ is required for the stiffness matrix. Since the *curl* of a gradient is zero we can write,

$$\begin{aligned}
\nabla \times \mathbf{w}_2 &= \nabla \times (s_2 s_3 \nabla s_1) \\
&= \nabla (s_2 s_3) \times \nabla s_1
\end{aligned} \tag{A.9}$$

This can be developed further,

$$\begin{aligned}
\nabla \times \mathbf{w}_2 &= \nabla(s_2 s_3) \times \nabla s_1 \\
&= (s_2 \nabla s_3 + s_3 \nabla s_2) \times \nabla s_1 \\
&= \left(s_2 \frac{\mathbf{V}_1 \times \mathbf{V}_2}{(\mathbf{V}_2 \times \mathbf{V}_3) \cdot \mathbf{V}_1} + s_3 \frac{\mathbf{V}_3 \times \mathbf{V}_1}{(\mathbf{V}_2 \times \mathbf{V}_3) \cdot \mathbf{V}_1} \right) \times \frac{\mathbf{V}_2 \times \mathbf{V}_3}{(\mathbf{V}_2 \times \mathbf{V}_3) \cdot \mathbf{V}_1} \\
&= \frac{s_2 (\mathbf{V}_1 \times \mathbf{V}_2) \times (\mathbf{V}_2 \times \mathbf{V}_3) + s_3 (\mathbf{V}_3 \times \mathbf{V}_1) \times (\mathbf{V}_2 \times \mathbf{V}_3)}{((\mathbf{V}_2 \times \mathbf{V}_3) \cdot \mathbf{V}_1)^2} \\
&= \frac{s_2 \mathbf{V}_2 - s_3 \mathbf{V}_3}{(\mathbf{V}_2 \times \mathbf{V}_3) \cdot \mathbf{V}_1}. \qquad \text{(A.10)}
\end{aligned}$$

The expressions for all the $\nabla \times \mathbf{w}_i$ are given in Table A.3.

A.2 Prismatic Elements

van Welij [1985] suggests that prismatic elements can be made from a hexahedral element by making two pairs of vertices coincide. Certainly the mapping $F(\mathbf{s})\colon \rightarrow \mathbf{r}$ remains valid, as does the integration. Furthermore, as he points out this mapping becomes singular at these vertices. It is, however, necessary to redefine the edge shape functions, one cannot simply use the hexahedral shape functions on those edges whose lengths have not become zero. This is because the gradients ∇s_i are now undefined at the duplicate vertices.

To define the new shape functions we start with a triangular element and define three new local co-ordinates, $\zeta_1, \zeta_2, \zeta_3$ corresponding to the normal barycentric co-ordinates of a triangle. The edge shape functions for the three edges of the triangle are then defined, as normal, by

$$\begin{aligned}
\mathbf{w}_0 &= \zeta_1 \nabla \zeta_2 - \zeta_2 \nabla \zeta_1, \\
\mathbf{w}_1 &= \zeta_1 \nabla \zeta_3 - \zeta_3 \nabla \zeta_1, \\
\mathbf{w}_2 &= \zeta_2 \nabla \zeta_3 - \zeta_3 \nabla \zeta_2. \qquad \text{(A.11)}
\end{aligned}$$

We now note that the triangular shape functions can be written in terms of the co-

$$
\begin{aligned}
\nabla \times \mathbf{w}_0 &= \frac{(s_2-1)\mathbf{V}_2-(s_3-1)\mathbf{V}_3}{(\mathbf{V}_2\times\mathbf{V}_3)\cdot\mathbf{V}_1} \\
\nabla \times \mathbf{w}_1 &= \frac{-s_2\mathbf{V}_2+(s_3-1)\mathbf{V}_3}{(\mathbf{V}_2\times\mathbf{V}_3)\cdot\mathbf{V}_1} \\
\nabla \times \mathbf{w}_2 &= \frac{s_2\mathbf{V}_2-s_3\mathbf{V}_3}{(\mathbf{V}_2\times\mathbf{V}_3)\cdot\mathbf{V}_1} \\
\nabla \times \mathbf{w}_3 &= \frac{(1-s_2)\mathbf{V}_2+s_3\mathbf{V}_3}{(\mathbf{V}_2\times\mathbf{V}_3)\cdot\mathbf{V}_1} \\
\nabla \times \mathbf{w}_4 &= \frac{(s_1-1)\mathbf{V}_1-(s_2-1)\mathbf{V}_2}{(\mathbf{V}_2\times\mathbf{V}_3)\cdot\mathbf{V}_1} \\
\nabla \times \mathbf{w}_5 &= \frac{(1-s_1)\mathbf{V}_1+s_2\mathbf{V}_2}{(\mathbf{V}_2\times\mathbf{V}_3)\cdot\mathbf{V}_1} \\
\nabla \times \mathbf{w}_6 &= \frac{s_1\mathbf{V}_1-s_2\mathbf{V}_2}{(\mathbf{V}_2\times\mathbf{V}_3)\cdot\mathbf{V}_1} \\
\nabla \times \mathbf{w}_7 &= \frac{-s_1\mathbf{V}_1+(1-s_2)\mathbf{V}_2}{(\mathbf{V}_2\times\mathbf{V}_3)\cdot\mathbf{V}_1} \\
\nabla \times \mathbf{w}_8 &= \frac{(s_1-1)\mathbf{V}_1-(s_3-1)\mathbf{V}_3}{(\mathbf{V}_2\times\mathbf{V}_3)\cdot\mathbf{V}_1} \\
\nabla \times \mathbf{w}_9 &= \frac{-s_1\mathbf{V}_1+(s_3-1)\mathbf{V}_3}{(\mathbf{V}_2\times\mathbf{V}_3)\cdot\mathbf{V}_1} \\
\nabla \times \mathbf{w}_{10} &= \frac{s_1\mathbf{V}_1-s_3\mathbf{V}_3}{(\mathbf{V}_2\times\mathbf{V}_3)\cdot\mathbf{V}_1} \\
\nabla \times \mathbf{w}_{11} &= \frac{(1-s_1)\mathbf{V}_1+s_3\mathbf{V}_3}{(\mathbf{V}_2\times\mathbf{V}_3)\cdot\mathbf{V}_1}
\end{aligned}
$$

Table A.3: Curl of shape functions for hexahedral edge element.

$$
\begin{aligned}
\mathbf{w}_0 &= (1-s_2)\left\{(1-s_3)\nabla s_1 + s_1\nabla s_3\right\} \\
\mathbf{w}_1 &= s_2\left\{(1-s_3)\nabla s_1 + s_1\nabla s_3\right\} \\
\mathbf{w}_2 &= s_2\left\{s_1\nabla s_3 - s_3\nabla s_1\right\} \\
\mathbf{w}_3 &= (1-s_2)\left\{s_1\nabla s_3 - s_3\nabla s_1\right\} \\
\mathbf{w}_4 &= (1-s_2)\left\{(1-s_1)\nabla s_3 + s_3\nabla s_1\right\} \\
\mathbf{w}_5 &= s_2\left\{(1-s_1)\nabla s_3 + s_3\nabla s_1\right\} \\
\mathbf{w}_6 &= (1-s_1-s_3)\nabla s_2 \\
\mathbf{w}_7 &= s_1\nabla s_2 \\
\mathbf{w}_8 &= s_3\nabla s_2
\end{aligned}
$$

Table A.4: Shape functions for prism edge element

ordinates s_i,

$$
\begin{aligned}
\zeta_1 &= 1-s_1-s_2 \\
\zeta_2 &= s_1 \\
\zeta_3 &= s_3. \qquad \text{(A.12)}
\end{aligned}
$$

Substitution of equations (A.12) into equation (A.11) gives,

$$
\begin{aligned}
\mathbf{w}_0 &= (1-s_3)\nabla s_1 + s_1\nabla s_3 \\
\mathbf{w}_1 &= (1-s_1)\nabla s_3 + s_3\nabla s_1 \\
\mathbf{w}_2 &= s_1\nabla s_3 - s_3\nabla s_1. \qquad \text{(A.13)}
\end{aligned}
$$

These can now be used to produce the complete set of shape functions for a prism in terms of the coordinates s, Table A.4. The curl of these shape functions is developed in the same way as the hexahedral elements and are given in Table A.5.

$$
\begin{aligned}
\nabla \times \mathbf{w}_0 &= \frac{-s_1\mathbf{V}_1 - (s_3-1)\mathbf{V}_3}{(\mathbf{V}_2 \times \mathbf{V}_3)\cdot \mathbf{V}_1} \\
\nabla \times \mathbf{w}_1 &= \frac{s_1\mathbf{V}_1 - 2s_2\mathbf{V}_2 + (s_3-1)\mathbf{V}_3}{(\mathbf{V}_2 \times \mathbf{V}_3)\cdot \mathbf{V}_1} \\
\nabla \times \mathbf{w}_2 &= \frac{s_1\mathbf{V}_1 - 2s_2\mathbf{V}_2 + s_3\mathbf{V}_3}{(\mathbf{V}_2 \times \mathbf{V}_3)\cdot \mathbf{V}_1} \\
\nabla \times \mathbf{w}_3 &= \frac{-s_1\mathbf{V}_1 - s_3\mathbf{V}_3}{(\mathbf{V}_2 \times \mathbf{V}_3)\cdot \mathbf{V}_1} \\
\nabla \times \mathbf{w}_4 &= \frac{(s_1-1)\mathbf{V}_1 + 2(1-s_2)\mathbf{V}_2 + s_3\mathbf{V}_3}{(\mathbf{V}_2 \times \mathbf{V}_3)\cdot \mathbf{V}_1} \\
\nabla \times \mathbf{w}_5 &= \frac{(1-s_1)\mathbf{V}_1 + 2s_2\mathbf{V}_2 - s_3\mathbf{V}_3}{(\mathbf{V}_2 \times \mathbf{V}_3)\cdot \mathbf{V}_1} \\
\nabla \times \mathbf{w}_6 &= \frac{-\mathbf{V}_1 - \mathbf{V}_3}{(\mathbf{V}_2 \times \mathbf{V}_3)\cdot \mathbf{V}_1} \\
\nabla \times \mathbf{w}_7 &= \frac{\mathbf{V}_3}{(\mathbf{V}_2 \times \mathbf{V}_3)\cdot \mathbf{V}_1} \\
\nabla \times \mathbf{w}_8 &= \frac{\mathbf{V}_1}{(\mathbf{V}_2 \times \mathbf{V}_3)\cdot \mathbf{V}_1}
\end{aligned}
$$

Table A.5: Curl of shape functions for prism edge element

Appendix

B Waveguide Coupler

In order to measure the spectrum of the magnetron it was necessary to find some way to couple the spectrum analyser to the microwave system. Since the maximum permissible power input to the spectrum analyser is below 1 Watt and the output of the magnetron in the region of 700 Watts a large degree of attenuation is required. For this purpose a waveguide coupler, shown in Figure B.1 was constructed. It was desired to measure the spectrum of the power supplied to the cavity rather than the power reflected from the cavity which will have a spectrum that is also dependent upon the loading. The field a a point in the waveguide feed is a combination of the forward and backward waves so the coupler was designed so that it could differentiate between them.

The coupler consists of two E-field probes that are located one quarter of a wavelength apart in the wall of the waveguide, as shown in Figure B.1. The probes were designed to provide a high level of attenuation, which also means that they have virtually no perturbing effect upon the fields in the waveguide. The signals from the two probes are coupled to a packaged quadrature hybrid. This is designed so that the signal fed in at one port is split so that it appears at the opposite port attenuated by 3 dB and at the diagonally opposite port attenuated by 3 dB and phase shifted by 90 degrees. A wave travelling in the forward direction, as shown in Figure B.1, will provide a signal at the two probes which is 90 degrees apart so that at one output port of the quadrature hybrid the two signals will add whereas at the other they will be in anti-phase and so

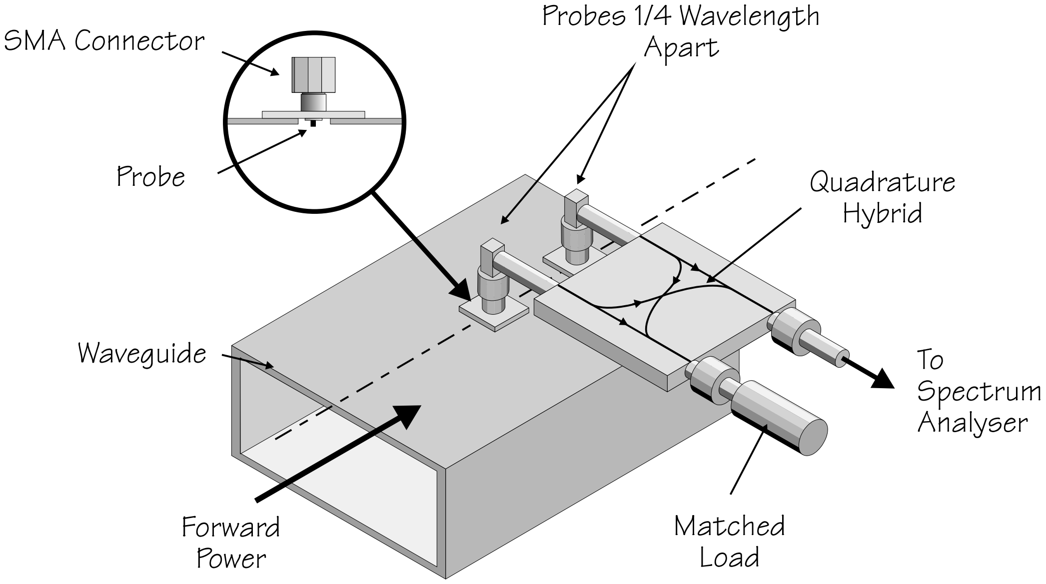

Figure B.1: Waveguide coupler used to connect the feed waveguide to the spectrum analyser.

subtract. Since a wave travelling in the reverse direction will produce signals at the probes which as the opposite phase relationship the forward wave will couple to one of the output ports and the backward wave to the other. For this to work in practice the two probes need to be identical and exactly one quarter of a wavelength apart. The coupler achieved a directionality of 38 dB, that is the signal at the port that should be zero was 38 dB lower than the signal at the other output port. One port was connected to the spectrum analyser via a further attenuator and the other port to a matched load.